Université de Neuchâtel
Institut de Microtechnique

Amorphous silicon for optimized multi-junction solar cells: Material study and cell design

Thèse

**présentée à la faculté des sciences,
pour l'obtention du titre de docteur ès sciences**

par

Rainer Platz

UFO Dissertation Band 362

Die Deutsche Bibliothek – CIP-Einheitsaufnahme

Platz, Rainer
Amorphous silicon for optimized multi-junction solar cells: Material study and cell design / Rainer Platz. – 1. Aufl. – Allensbach : UFO, Atelier für Gestaltung und Verl., 1999
(UFO-Dissertation ; Bd. 362)
Zugl.: Neuchâtel, Univ., Diss., 1999
ISBN 3-930803-61-5

Dissertation der Universität Neuchâtel
Datum der mündlichen Prüfung: 17. März 1999
Referenten: Prof. Dr. A. Shah
Prof. Dr. J. Faist
Dr. H. Schade
Prof. Dr. S. Wagner

UFO Atelier für Gestaltung & Verlag GbR
Allensbach
Internet http://www.ufo.znet.de
Maus Druck & Medien GmbH, Konstanz
Erste Auflage 1999

ISBN 3-930803-61-5

IMPRIMATUR POUR LA THÈSE

Amorphous silicon for optimized multi-junction solar cells: material study and cell design

de M. Rainer Platz

UNIVERSITÉ DE NEUCHÂTEL

FACULTÉ DES SCIENCES

La Faculté des sciences de l'Université de Neuchâtel sur le rapport des membres du jury,

MM. A. Shah (directeur de thèse), J. Faist,
H. Schade (Putzbrunn D) et
S. Wagner (Princeton, USA)

autorise l'impression de la présente thèse.

Neuchâtel, le 6 mai 1999

Le doyen:

F. Stoeckli

Content

I. INTRODUCTION 1

I.1. GENERAL INTRODUCTORY REMARKS 1

I.1.1. Solar energy conversion using solar cells *1*

I.1.2. The case for amorphous silicon *3*

I.1.3. Background and outline of this work *7*

I.2. SAMPLE PREPARATION 9

I.2.1. The deposition systems *9*

I.2.2. Layers *10*

I.2.3. Solar cells *10*

I.3. MATERIAL CHARACTERIZATION 11

I.3.1. Optical characterization *11*

I.3.2. Electrical characterization *14*

I.3.3. Structural characterization *16*

I.4. CHARACTERIZATION OF SOLAR CELLS 19

I.4.1. I-V measurements *19*

I.4.2. Spectral response measurements *20*

I.4.3. Solar cell degradation *21*

II. INTRINSIC MATERIAL 22

II.1. A-SiC:H 22

II.1.1. Introduction *22*

II.1.2. Material study *23*

II.1.3. Discussion and conclusions *32*

II.2. A-Si:H 34

II.2.1. Introduction *34*

II.2.2. Hydrogen dilution and influence of the substrate temperature *35*

II.2.3. Comparison of VHF, RF and DC plasma excitation *43*

II.2.4. Discussion and conclusions *56*

III. SINGLE-JUNCTION SOLAR CELLS 58

III.1. INTRODUCTION 58

III.2. A-SiC:H SINGLE-JUNCTION SOLAR CELLS 60

III.3. A-Si:H SINGLE-JUNCTION SOLAR CELLS 63

III.3.1. i-layer deposition with H_2 dilution *63*

III.3.2. p-i-n cells at enhanced substrate temperature *67*

III.4. DESIGN AND TECHNOLOGICAL CONSIDERATIONS 69

III.4.1. Graded hydrogen dilution - "a-Si:H buffer" ... *69*
III.4.2. a-SiC:H "buffer" layers ... *71*
III.4.3. Sources of i-layer contamination ... *78*
III.5. V_{oc}-DETERMINING FACTORS ... 84
III.6. CONCLUSIONS: THREE DEPOSITION TECHNIQUES "À LA CARTE" ... 87

IV. TANDEM SOLAR CELLS ... **89**

IV.1. INTRODUCTION ... 89
IV.2. A-SI:H/A-SI:H STACKED CELL ... 91
IV.2.1. Semi-empirical modeling of stacked cells ... *91*
IV.2.2. Modeling of a-Si:H/a-Si:H stacked cells ... *94*
IV.2.3. Technological realization ... *96*
IV.2.4. Conclusions ... *100*
IV.3. MICROMORPH TANDEM CELL ... 101
IV.3.1. Special challenge for the top cell in a micromorph tandem ... *101*
IV.3.2. Choice of a top cell deposition technique ... *102*
IV.3.3. Modeling of micromorph tandem cells ... *106*
IV.3.4. Results and discussion ... *109*
IV.3.5. Conclusions ... *122*

V. GENERAL CONCLUSIONS ... **124**

VI. ANNEX ... **128**

VI.1. MATLAB PROGRAM CALCULATING I-V CURVE OF A STACKED CELL ... 128
VI.2. I-V CURVES FOR MODELING OF MICROMORPH TANDEM CELLS ... 129
VI.3. CONSTANTS, SYMBOLS AND ABBREVIATIONS ... 130
VI.3.1. Constants ... *130*
VI.3.2. Symbols ... *130*
VI.3.3. Abbreviations ... *131*
VI.4. FURTHER PUBLICATIONS ... 133

VII. REFERENCES ... **136**

I. Introduction

I.1. General introductory remarks

The growing world population and, at the same time, the continuous development of most countries results in a growing demand for energy. It is by now generally recognized that in the future a considerable amount of energy has to be covered by renewable sources. The limits of classical energy sources, such as coal, oil, gas, uranium, but increasingly also environmental questions account for the growing understanding in most countries of the urgency of this question. It is, however, not clear today which form of renewable energies will be able to economically provide considerable amounts of power. Wind, bio-mass and nuclear fusion energy among many others are currently being discussed and research is being undertaken. Most probably, a mix of several technologies will have to replace step by step fossil energy sources.

Solar energy has the advantage of its abundance and availability all over the globe. The world energy demand is currently on the order of 357 EJ per year [1] (1 EJ = 10^{18} J), which is only 0.013 % of the 2.8 million exajoules [2] of solar energy received every year on the earth's surface in the form of sunlight.

Photovoltaic (PV) solar energy conversion has the advantage of providing energy directly as electricity, which is for many applications the most valuable and versatile form of energy. Photovoltaic energy conversion is therefore one of the most promising and realistic technologies for at least partial coverage of the energy demand in the future. Already today, PV energy is of growing interest for special applications, though not yet economically competitive with conventional energy sources.

I.1.1. Solar energy conversion using solar cells

In a solar cell, free electric carriers are created by the absorption of light within a solid-state semiconductor. Light-generated electron-hole pairs are separated by the electric field present in the solar cell. This internal electric field can be established by either a p-n homo- or hetero-junction or a Schottky barrier type (metal-semiconductor) junction.

The conversion efficiency of a solar cell is determined by

a) its capability to absorb sunlight, which determines the current of the solar cell. The absorption coefficient of the absorbing material in a solar cell determines the maximum achievable current density. In semiconductor materials, the bandgap defines the minimum

photon energy that is required to generate an electron-hole pair. Photons with lower energy than what corresponds to this bandgap energy are not absorbed in the solar cell.

b) The energy level, at which charge carriers can be extracted from the solar cell, which determines the voltage of the cell.

c) The amount of carriers recombining, within the solar cell, on their way to the contacts, being therefore lost to the current generation. Such losses are reflected in the so-called fill factor of the solar cell (see section I.4.1).

Solar cells are - in general - optimized for maximum conversion efficiency with respect to the solar spectrum. Figure 1 shows the power density distribution available in the global normal radiation spectrum on the earth's surface. This so-called AM 1.5 solar spectrum gives the energy distribution of the sunlight after 1.5 passes (AM stands for air mass) through the earth's atmosphere, corresponding to a solar zenith angle of ~48°. The solar spectrum outside the atmosphere (AM 0) corresponds, roughly, to the radiation of a black body at ~6000 K, i.e. the temperature of the sun's surface. The global AM 1.5 spectrum integrates to a power density of 965 W/m^2, i.e. ~1000 W/m^2, which is generally taken for solar cell efficiency measurements.

As stated above, semiconductors absorb the solar spectrum up to wavelengths

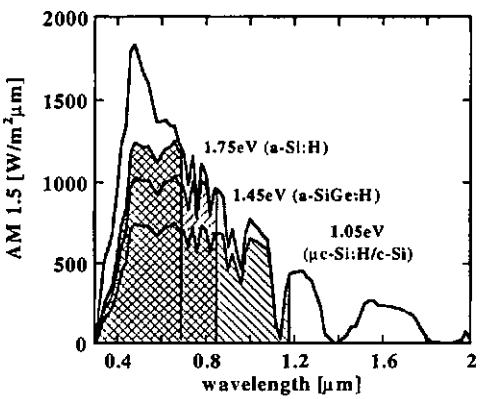

Figure 1: AM 1.5 solar spectrum and power density AM 1.5·$E_g/h\nu$ (shaded areas) for semiconductor materials with different bandgaps. The power density of the solar spectrum is reduced by $E_g/h\nu$, the excess energy is lost due to thermalization of the carriers to the band edges.

corresponding to their bandgap energy. The maximum energy at which carriers can be extracted (which is related to the maximum voltage of the solar cell) depends on the bandgap of the absorbing semiconductor material. Therefore, the smaller the bandgap of the semiconductor material, the higher the achievable current density within the solar cell. The excess energy of the photons (= photon energy minus bandgap energy), however, is lost due to thermalization of the carriers to the band edges.

The shaded areas in Figure 1 illustrate the power potential for semiconductor materials of different optical gap. Multiplying the power distribution of the solar spectrum by $E_g/(h\nu)$ takes into account thermalization losses, and integration over all wavelengths yields a power density [W/m^2]. This power density would be achieved if all photons were absorbed and the carriers could be extracted without losses at a voltage E_g/e. In reality, however, the voltage of a solar cell has, for physical reasons, to be considerably lower than E_g/e. We show as an example in Figure 1 the cases for hydrogenated amorphous silicon (a-Si:H, $E_g \sim 1.75$ eV), hydrogenated amorphous silicon germanium (a-SiGe:H) alloy of $E_g \sim 1.45$ eV and hydrogenated microcrystalline silicon (μc-Si:H) with a bandgap energy that is approximately comparable to crystalline silicon ($E_g \sim 1.05$ eV).

An optimum bandgap for single-junction solar cells is theoretically expected: the current density increases with decreasing gap of the absorbing layer in the solar cell while the open circuit voltage, i.e. the energy level at which carriers are collected, decreases at the same time. Semi-empirical models predict this maximum to lie around 1.5 eV [3], which is considerably higher than the value for crystalline silicon (~1.1 eV) and slightly lower than the standard value for a-Si:H (~1.75 eV). GaAs (~1.45 eV) matches the optimum value quite well, however its high cost makes this material not suited for large-scale PV production and restricts its application to some niches.

The utilization of the energy that is available in the solar spectrum can therefore be optimized by splitting the solar spectrum and absorbing light of different wavelengths in solar cells with different bandgap because the energy lost due to thermalization can be minimized. In other words, the surface under the solar power distribution can be "filled" with less lost area. Light transmitted through a large-gap cell can be absorbed in a cell with a lower gap and then possibly a third cell can convert the remaining red light. In a-Si:H based solar cells this division of the absorbing layer into two or more thinner layers additionally helps the stability of the solar cell against light soaking, as will be discussed in section IV.1.

I.1.2. The case for amorphous silicon

In planning for the future scaling-up of photovoltaic power generation it is important to carefully choose the semiconductor material of which the solar cells are to be made. Important criteria for the choice are, on the one hand, the maximum achievable efficiency,

but, on the other hand, also economical and ecological aspects. These become even more important if one considers in future to cover large areas with solar modules. The availability of the raw material as well as the nature of the production technology used are important criteria determining the feasible minimum cost of solar cells. Considering only materials which are abundantly available in the earth's crust, which are non-toxic and which have already reached technological maturity, one is left with silicon as the only realistic medium-term candidate for semiconductor photovoltaic solar cells [3]. Silicon is perhaps the best-known semiconductor material and the technology for handliog silicon is certainly very well developed.

Crystalline silicon (c-Si) photovoltaic technology undoubtedly is mature, yielding high efficiencies and excellent stability, proven through long-term field use. At present, however, high production costs of c-Si solar cells, essentially linked to the use of wafer processing, constitute a major barrier to the widespread use of PV energy conversioo. Thus, there is a very strong motivation for developing a viable thin-film silicon solar cell technology.

Unfortunately, c-Si is a semiconductor with an indirect optical gap. This has as consequence that its absorption in the interesting spectral range of maximum solar power is relatively poor. Thus, solar cells made from c-Si have to be relatively thick (30 µm of monocrystalline silicon to absorb ~80 % of the sunlight without additiooal light-trapping). In order to make crystalline silicon a competitive altemative for large-area photovoltaic energy generation, technologies have to be developed to deposit (multi-) crystalline silicon of good quality on low-cost substrate materials. Additionally, suited light-trapping structures have to

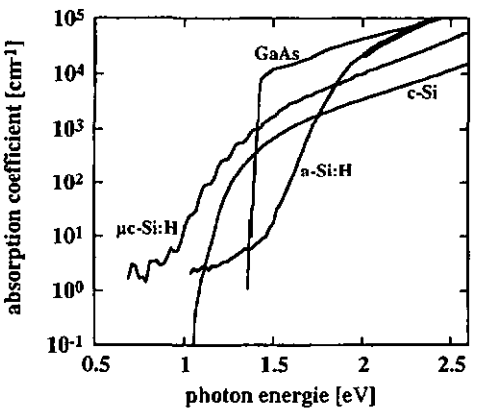

Figure 2: Absorption spectra of c-Si, GaAs, a-Si:H and µc-Si:H as a function of photon energy.

be advanced.

A very favorable candidate for thin-film solar cells is hydrogenated amorphous silicon (a-Si:H) which has fundamentally higher absorption (due to the structural disorder of the material, the quantum mechanical selection rules for optical transitions do not act in the same way). Practically, it has an absorption in the "useful" spectral range (cf. Figure 2) that is higher by an order of magnitude than c-Si. Therefore a-Si:H can be used as a "true" thin-film solar cell material, with thicknesses down to < 1 μm, provided one has suitable light-trapping structure.

Amorphous silicon can be deposited at relatively low temperatures of around 200°C from the gas phase in a plasma enhanced chemical vapor deposition (PECVD) process. This allows the deposition directly on suited substrates of considerable size. The most commonly used substrate is glass, however more and more interest and work is focused on alternative substrates such as stainless steel and polymers, allowing for cheap, light-weight and flexible substrate materials. A further advantage of the a-Si:H technology is the monolithic series connection during the production process and the possibility of alloying with other group IV elements. The optical bandgap (section I.3.1.2) can be varied over a wide range (<1.4 eV up to >2 eV) by germane or carbon alloying.

Amorphous silicon solar cells always use a p-i-n diode structure in contrast to the classical p-n diode structure used in virtually all crystalline solar cells so far. Although there are technological reasons for using a p-i-n structure in the case of a-Si:H (difficulty of doping, decrease of layer quality with doping), the p-i-n structure also offers some basic advantages with respect to collection. Collection is not a major problem for wafer-based c-Si solar cells. The minority carrier diffusion length L_{diff} is usually sufficiently large so that minority carriers are transported by diffusion to the junction, where the actual separation between holes and electrons takes place, due to the internal field in the depletion region. This depletion region is usually much thinner than the total cell thickness and the electric field extends only over this very thin region. a-Si:H, in contrast, has relatively poor transport properties, i.e. low carrier mobilities μ and short carrier lifetimes τ. The diffusion length, which is a function of the diffusion constant D and the lifetime, and which can be written as

Equation 1

$$L_{diff} = \sqrt{D\tau} = \sqrt{\frac{k_B T}{e}\mu\tau}$$

is therefore small (on the order of 100 nm). Hence, collection certainly is a major problem in a-Si:H based solar cells; diffusion alone is not sufficient as transport mechanism. In order to avoid that the major part of the generated free carriers recombines within the a-Si:H solar cell, it is imperative to have drift-assisted transport, based on an internal electric

field F extending over most of the cell, i.e. over the whole i-layer. The drift length L_{drift} in an intrinsic layer is given by

Equation 2

$$L_{drift} = \mu\tau F \approx \mu\tau \frac{V_{bi}}{d_i} ;$$

V_{bi} is the built-in voltage and d_i the thickness of the i-layer. If we define κ by setting $d_i = \kappa \cdot L_{drift}$ we obtain with $V_{bi} \sim 1$ V (V_{bi} depends on the gap)

Equation 3

$$\frac{L_{drift}}{L_{diff}} = \sqrt{\frac{V_{bi}}{k_B T / e} \cdot \frac{1}{\kappa}} \approx \sqrt{\frac{40}{\kappa}} .$$

For $\kappa \leq 0.5$ (i.e. i-layer thickness less than half of the drift length, which is certainly not unreasonable in order to obtain satisfactory collection) one obtains that the drift length is roughly a factor of 10 larger than the diffusion length. Therefore, all a-Si:H solar cells consist of a p-i-n structure (Figure 3). The doped layers are very thin and serve only to establish the electric field in the i-layer. Carriers generated in the doped layers recombine instantly due to the high density of impurities and defects in amorphous doped layers and do therefore not contribute to the current generation. a-Si:H solar cells can be made in two different configurations. The most commonly used approach is to deposit the solar cell structure in the

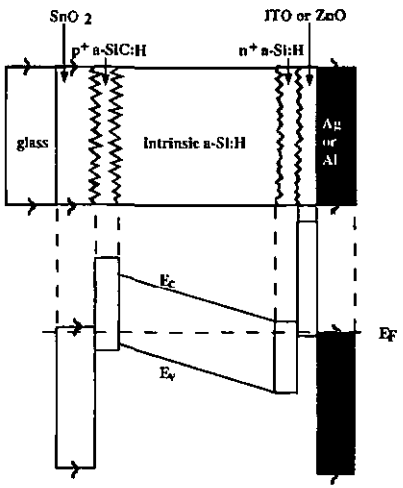

Figure 3: Schematic cross-section (top) and band diagram (bottom) of an amorphous single-junction p-i-n solar cell.

p-i-n sequence on top of glass covered with transparent conductive oxide (TCO). In order to enhance the optical path in the solar cell, this TCO layer is textured. The back contact is usually made of sputtered indium tin oxide (ITO) or zinc oxide (ZnO) and a highly reflective metal (silver or aluminum) layer. An alternative concept, which is continuously gaining in interest, is to deposit the solar cell in the n-i-p sequence on top of a non-transparent substrate such as stainless steel or polymers. The top p-layer is then contacted with ITO in order to establish the front contact. All solar cells in this work are of the p-i-n (or "superstrate") structure.

I.I.3. Background and outline of this work

Prior to the present work, a well-established technology for a-Si:H solar cells had already been developed at IMT. The amorphous doped layers had been intensively studied and the intrinsic i-layer (deposited from undiluted SiH_4) allowed for quite satisfying initial solar cell efficiencies with values exceeding 10 %. It had been shown that the VHF plasma excitation technique, i.e. plasma excitation by a very high frequency (VHF) source, leads to initial cell efficiencies that are comparable to those obtained with the more conventional standard 13.56 MHz industrial frequency.

At this point in time, the stabilized efficiency had become the most important issue in the optimization of a-Si:H solar cells. In fact, shortly after the invention of the a-Si:H solar cell in 1976 [4], Staebler and Wronski discovered that the photo-conductivity of the material decreased under illumination [5], an effect which was found to be reversible upon annealing at high temperature. This so-called Staebler-Wronski effect was found to be due to a reversible increase in the defect density of the material (metastability), which also affects the conversion efficiency of an a-Si:H solar cell. Since then, stability against light-induced degradation is one of the most important issues in the optimization of a-Si:H solar cells. Different approaches to reduce degradation - or at least its consequences on the solar cell performance - are being undertaken and are also key points in this work: A) More stable intrinsic material results in enhanced solar cell stability. B) The question for stabilized efficiencies also includes design considerations such as application of buffer layers, tandem cell structures or variation of the optical bandgap for maximum utilization of the solar spectrum.

This work focuses on the variation of the optical gap of a-SiC:H alloys and unalloyed a-Si:H with a special emphasis on the material stability. Throughout the work, the close connection of material and device study is emphasized. A peculiarity of this work is therefore the optimization of material needed for a given solar cell application, rather than an academic material study where the incorporation into a solar cell is only a final, separate tool. This explains the structure of the work:

a-SiC:H alloys were investigated with the goal to make high-voltage solar cells by using this material as the i-layer. Once a suitable material had been obtained, further optimization of the material was done within the solar cell.

During the course of this study hydrogen dilution of the silane plasma to deposit unalloyed a-Si:H has shown to yield V_{oc} values which were – in the degraded state – comparable to those obtained with a-SiC:H solar cells, yet with considerably higher fill factor and current values. In consequence, and in parallel with the developments in other laboratories, the focus was shifted towards these materials and solar cells incorporating H_2 diluted i-layers.

The upcoming interest in a-Si:H/μc-Si:H (micromorph) tandem cells again partially changed the focus of this work. First, here also, the enhanced stability of H_2 diluted a-Si:H cells, later on combined with different kinds of buffer layers, seemed to be the key to an enhanced stabilized efficiency of the micromorph cell. Later on, we came to the conclusion, that the optimum top cell for a micromorph tandem cell would need to be a cell which provides a high current density within a relatively thin intrinsic layer, which made the development of low-bandgap a-Si:H necessary. Furthermore, as a reduced optical gap can most appropriately be obtained through an increased deposition temperature, a p-i-n solar cell technology was developed for the deposition p-i-n solar cells at comparatively high temperatures.

I.2. Sample preparation

I.2.1. The deposition systems

Most samples described in this work (i-layers and complete p-i-n or stacked solar cells) were deposited in a single-chamber reactor with load lock using the very high frequency glow discharge technique (VHF-GD) at 70 MHz. The a-SiC:H material study was performed in a similar reactor, however without load lock. The RF input power is coupled capacitively to the plasma. Power values given in this work are measured by a power meter between the generator and the matching network. The substrate size is 8×8 cm^2, the substrate is fixed on the grounded electrode and the distance to the powered electrode is 1.6 cm. The deposition system is described in more detail in [6].

The depositioo pressure was, unless otherwise stated, 0.35 mbar for the standard SiH_4 plasma and 0.5 mbar when H_2 dilution was applied. For the deposition of the amorphous p-layer we used silane (SiH_4), methane (CH_4) and diborane (B_2H_6). Intrinsic layers were made from SiH_4 with or without hydrogen (H_2) dilution. a-SiC:H i-layers were deposited from SiH_4 and CH_4 with varying H_2 dilution ratios. Amorphous and microcrystalline n-layers were deposited by adding phosphine (PH_3) to a H_2 diluted SiH_4 plasma.

The substrate temperatures given throughout this work are calibrated values and correspond to the true substrate temperature during deposition. Even though the substrate is in close mechanical contact with the heated electrode, its temperature is always considerably lower than the electrode temperature. Calibration was performed by measuring the temperature on the substrate surface under conditions (i.e. gas flow, pressure) identical to those during deposition, however without plasma. In our VHF-system, the lower (powered) electrode temperature was set to 130°C and the value of the upper electrode with the substrate mounted on it could be varied.

Another deposition system, used for some of the samples described in this work, is a three-chamber 'S-900' system with load-lock available at Princeton University. This PECVD system, built for Solarex by Innovative Systems Engineering, was originally designed for the use of direct current (DC) plasma excitation. In this case, the powered electrode (cathode) is biased negatively with respect to the grounded substrate (anode) The system can, however, also be used for deposition using 13.56 MHz plasma excitation. A more detailed description of the deposition system can be found in [7].

We incorporated some data on RF-deposited films in this work. Those samples have been deposited by the group at the Forschungszentrum Jülich, using 13.56 MHz plasma excitation. Deposition conditions for films deposited using DC and RF plasma excitation are listed in section II.2.3.

I.2.2. Layers

Samples for optical, electronic and structural characterization were grown on glass substrates (Schott AF45 and Dow Corning DC 7059) for optical and transport measurements and crystalline silicon wafers for infrared absorption measurements. The glass substrates were cleaned prior to utilization using a commercial detergent and several steps of rinsing in de-ionized water. After loading of the substrates into the load lock and pump down, the substrate holder was transferred into the deposition chamber. We allowed for at least 30 minutes for heat-up in the deposition chamber. When strong H_2 dilution was used for the deposition, we pumped after loading over night before performing the deposition. Directly prior to the deposition, the mixture of gases used for the film growth was flown during 10 minutes before igniting the plasma in order to stabilize the gas flow and the substrate temperature. The gas fluxes were calibrated from time to time in order to keep track of a possible drift of the mass flow controllers. We deposited samples in a single-chamber reactor for the a-SiC:H study. In this case, the substrates were loaded into the reactor followed by pump-down and heat-up of the electrodes. Once a base pressure of 10^{-6} mbar was obtained, a pre-flow as described above was applied, followed by deposition.

I.2.3. Solar cells

Most solar cells were deposited on Asahi U-type TCO (SnO_2). The cell structure is p-i-n, i.e. the p-layer is deposited directly onto the TCO, followed by i- and n-layer. Magnetron sputtered ZnO or ITO followed by thermally evaporated silver was deposited onto the n-layer as back contact. The ZnO or ITO layer, together with the highly reflective metal surface, acts as an interferometric layer, which enhances the red response of the solar cell due to wavelength-selective reflection. Anti-reflecting coatings on the front-side of the cells have not been employed. Solar cells were annealed for 90 minutes in nitrogen atmosphere at 180°C.

Some of the top cells for micromorph tandem cells (chapter IV) have been deposited on CVD-deposited textured ZnO, which combines high conductivity with excellent light-trapping properties.

I.3. Material characterization

The film thickness was measured using an α-Step profiler. A suited step was obtained either by using scotch-tape to remove the film partially and leaving a well-defined edge, by scratching with a cutter blade or by etching in KOH. The growth rate was determined by dividing film thickness by growth time.

I.3.1. Optical characterization

I.3.1.1. Absorption spectrum from transmission and reflection

Transmission and reflection spectra were measured using a Perkin Elmer Lambda 900 spectrometer. The samples were mounted with the film surface towards the incoming beam. To obtain the absorption coefficient α as a function of the wavelength, two methods can be applied.

The method proposed by Hishikawa et al. [8], which has been used in this work, uses the transmission (T) and reflection (R) spectra as well as the film thickness d in order to determine α according to the following formula. Interference fringes are eliminated because both, transmission and reflection spectra, contain maxima and minima at the same wavelengths:

Equation 4

$$\alpha(\lambda) = \frac{-1}{d} \ln\left(\frac{T(\lambda)}{1 - R(\lambda)}\right)$$

Another method, introduced by R. Swanepoel [9], uses only the transmission spectrum. The index of refraction as well as the film thickness is determined using the minima and maxima in the transmission spectrum. The index of refraction can then be used to calculate the reflection which yields, together with the transmission spectrum the absorption coefficient.

I.3.1.2. Determination of the optical bandgap

There is no unique technique for determining the optical bandgap of a-Si:H and its alloys from the α(λ) curve. The optical bandgap is used for amorphous semiconductors because no real gap is present in this case (Figure 5), there are states in the whole energy range. Most commonly, a method proposed by Tauc et al. [10] is applied. The procedure assumes parabolic band edges for direct semiconductors. The optical bandgap E_{Tauc} is obtained by extrapolation of the linear region in a $\sqrt{\alpha E}(E)$ plot, E_{Tauc} being the energy value at the intersection of the fit with the energy axis. The method yields good results for materials close to "standard" a-Si:H. However, when applied for a-Si:H alloys or materials deposited under

uncommon conditions, it is not always simple and unambiguous to determine a linear region in the plot. As a small variation in the slope of this linear region results in considerable changes of the E_{Tauc} values, this method results in some uncertainty concerning the proper determination of the bandgap.

We therefore use througbout this work as optical gap the quantity E_{04}, defined by $\alpha(E_{04}) = 10^4\ cm^{-1}$. This value has no direct physical meaning, however the determination of the value on the absorption curve is straightforward and therefore less susceptible to errors due to the determination of a linear region in the Tauc plot. Interference fringes in the absorption curve are a certain source of error, depending on the optical gap and the thickness of the film.

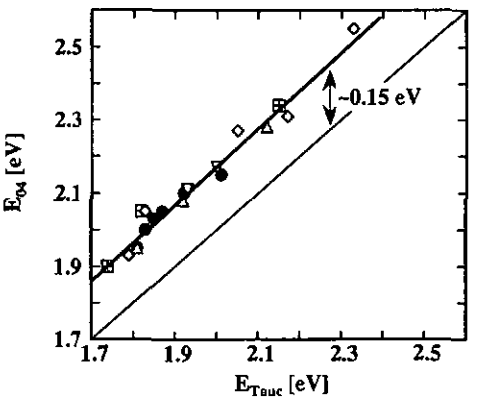

Figure 4: Comparison of values obtained for the optical gap E_{04} in comparison to values obtained for Tauc's optical gap E_{Tauc}. The second line corresponds to $E_{04} = E_{Tauc}$.

Figure 4 compares E_{Tauc} and E_{04} values for a-SiC:H samples deposited under various conditions. The figure indicates that both values scale linearly with each other, E_{04} being about 150 meV higher than the E_{Tauc} values. Therefore, in order to compare the values given in this work to other results, the following relationship should give a good approximation:

Equation 5

$$E_{04} = E_{Tauc} + 0.15eV$$

I.3.1.3. PDS/CPM

Transmission and reflection measurements allow to determine the absorption coefficient for large values of α ($\alpha d \geq 1$, i.e. for $\alpha > 10^4\ cm^{-1}$ with $d = 1\ \mu m$). For smaller values of α, i.e. the absorption coefficient in the sub-bandgap region, other techniques have been developed. Photothermal deflection spectroscopy (PDS) [11] measures the deflection of a laser beam due to the change of the index of refraction of a liquid around the a-Si:H sample. Monochromatic light is shined on the sample, the absorbed light heats the sample and the heat is transferred to the surrounding liquid. Absolute values are obtained by calibrating the spectra in the high-energy range to the absorption spectrum obtained from transmission/reflection measurements.

Another way to obtain the absorption spectrum in the sub-bandgap region is the constant photo-current method (CPM) [12]. Optical transitions excited by photons with energies smaller than the optical bandgap result in transitions from localized to extended states. Free carriers in the extended states can then be measured as a photo-current.

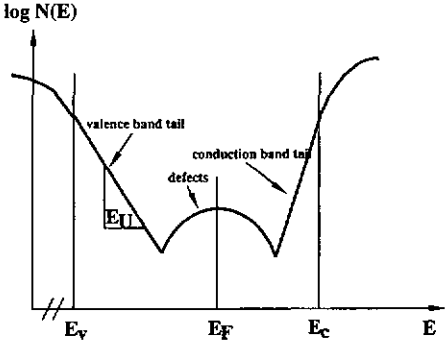

Figure 5: Schematic density of states distribution in a-Si:H.

Both methods, PDS and CPM, therefore yield information on the distribution of states within the optical bandgap (Figure 5).

A typical sub-bandgap absorption spectrum of a-Si:H (see, e.g., Figure 18, section II.2.2.1) shows two regions of the absorption coefficient. For small energies (< 1.2 eV) the absorption coefficient is determined by optical transitions between the defect states and the extended states (Figure 5). The absorption coefficient in this region is therefore a measure of the density of defects in the material. For higher photon energies, the absorption coefficient

increases exponentially, reflecting transitions between the band tails and the extended states. This part of the absorption spectrum is determined by the valence band tail, due to the fact that the valence band tail is much shallower than the conduction band tail. The inverse slope of the absorption spectrum in the exponential region is called Urbach energy (E_U). The Urbach energy (representing the valence band tail slope) is a measure for the disorder in the material.

I.3.2. Electrical characterization

I.3.2.1. Photo- and dark-conductivity

The steady-state cooductivity σ of an isotropic material is, according to Ohm's law, connected to the current density i due to an electric field F by

Equation 6

$$i = \sigma F, \qquad \sigma = e(n\mu_n + p\mu_p);$$

n and p are the densities of free electrons and holes and μ_n, μ_p are their mobilities. The dark-conductivity σ_d follows an exponential increase with temperature

Equation 7

$$\sigma_d = \sigma_0 \exp\left\{\frac{-E_{act}}{k_B T}\right\}.$$

E_{act} is the dark-conductivity activation energy which is the energy difference between the Fermi level and the band edge of the current-transporting band. In the case of undoped a-Si:H current transport by electrons in the conduction band is the determining transport mechanism, E_{act} in this case is the energy difference between the conduction band edge and the Fermi level.

Conductivity measurements were executed using coplanar aluminum contacts of 10 mm length with a gap of 0.5 mm. The samples were heated up to 180°C and afterwards slowly cooled down. $\sigma_d(T)$ was then used to extract values for the room temperature (25°C) dark-conductivity and the dark-conductivity activation energy.

The photo-conductivity σ_{ph} is defined as

Equation 8

$$\sigma_{ph} = eG(\mu_n\tau_n + \mu_p\tau_p) \approx eG\mu_n\tau_n,$$

μ_n, μ_p are the effective mobilities of electrons and holes and τ_n, τ_p their lifetimes. G is the generation rate. The photo-conductivity was measured under an intensity of 100 mW/cm² which corresponds to a generation rate of ~10^{21} $cm^{-2}s^{-1}$. Let us note that the photo-

conductivity is not necessarily a good measure for the quality of a-Si:H. The $\mu\tau$ product (i.e. the lifetime τ) of the majority carriers depends on the Fermi level. Especially in as-deposited a-Si:H samples, the Fermi level is above midgap. E.g. oxygen contamination can shift the Fermi level further towards the conduction band edge resulting in increased photo-conductivity values which are, however, not due to improved material quality. The problem is discussed in more detail in the following section.

1.3.2.2. Light soaking and $\mu_0\tau_0$ product

In order to study the stability of a-Si:H against light-induced degradation (Staebler-Wronski-effect), a reliable degradation procedure as well as a parameter is needed which reflects "true" electronic transport properties. As already indicated above, measurement of the photo-conductivity alone yields values which are directly influenced by the Fermi level and therefore do not necessarily reflect the material quality. Measurement of the ambipolar diffusion length, i.e. the $\mu\tau$ product of the minority carriers yields additional information but is also influenced by the Fermi level position. Figure 6 illustrates the Fermi-level dependence of the electron and hole $\mu\tau$ product. As will be seen in chapter II of this work, a Fermi-level independent quality parameter becomes even more important when dealing with un-intentionally doped films. E.g. oxygen contamination of the film results in a pronounced n-type doping leading to high photo-conductivity.

N. Beck et al. [14] developed therefore at IMT the material quality parameter $\mu_0\tau_0$. This

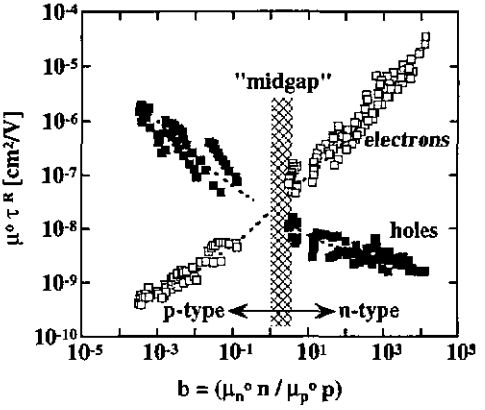

Figure 6: Electron and hole $\mu\tau$ product as a function of b, i.e. as a function of the Fermi level. Variation of the Fermi level position is obtained by degradation of micro-doped samples. The figure is taken from ref. 13.

mobility lifetime product combines the $\mu\tau$ product of the majority carriers (from photo-conductivity measurements) and information on the minority $\mu\tau$ product (from the steady-state photo-carrier grating, SSPG, technique) to a Fermi-level independent $\mu\tau$ product:

Equation 9

$$\mu_0\tau_0 = \frac{\sigma_{ph}}{eG}\cdot\frac{1}{z},$$

the correction factor z is defined as

Equation 10

$$z = \frac{p}{n}\cdot\frac{S_p^0}{S_n^+} + 1 + \frac{n}{p}\cdot\frac{S_n^0}{S_p^-},$$

n and p being the density of free electrons and holes, respectively, and S the capture cross sections of the dangling bonds. n and p are determined by measuring σ_{ph} and L_{amb} on the same sample whereas certain assumptions have to be made for the capture cross sections. The $\mu_0\tau_0$ product corresponds to the $\mu\tau$ product that would be measured by photo-conductivity measurements if all defects were neutral. The $\mu_0\tau_0$ product is especially required for samples where the Fermi level does not lie exactly at midgap, as is usually the case for as-deposited a-Si:H. $\mu_0\tau_0$ furthermore has been demonstrated to correlate with the performance of a-Si:H p-i-n solar cells [14,15]. The experimental error connected to the determination of the $\mu_0\tau_0$ product is estimated to be ±50 % in the initial and ±20 % in the light-soaked state [16].

Intrinsic films were degraded to their saturated light-soaked state by a combination of pulsed dye laser degradation and HeNe laser illumination as described in more detail in reference 17. The procedure has been designed so as to reach a stabilized degraded state, a state that corresponds to the state reached after 1000 h degradation with AM 1.5 light of 100 mW/cm^2 intensity.

RF-deposited films (section II.2.3) were light-soaked for 600 h using white light of 100 mW/cm^2 intensity and characterized by photo-conductivity and defect density (from constant photo-current method, CPM) measurements [18].

I.3.3. Structural characterization

Infrared (IR) absorption measurements can be used to gain information on the material structure and chemical bonding configuration. Measurements were performed using a Perking Elmer FT-IR 1720X spectrometer. IR absorption spectra of a-Si:H samples can be used to determine the hydrogen content in the films by integration of the 640 cm^{-1} absorption peak in the IR absorption spectrum, using [19]

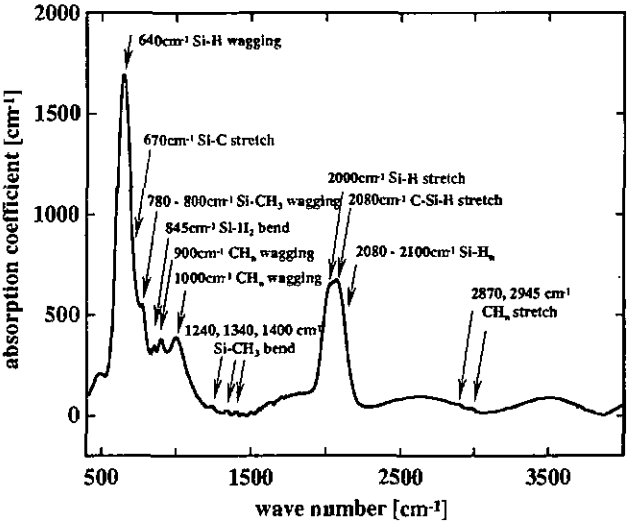

Figure 7: IR absorption spectrum of an a-SiC:H sample (40 %CH_4, H_2 dilution ratio 10) and assignments of the most important absorption peaks.

Equation 11

$$C_H[at.\%] = \frac{2.1 \cdot 10^{19} cm^{-2}}{5 \cdot 10^{22} cm^{-3}} \int \frac{\alpha(\omega)}{\omega} d\omega .$$

If the thickness of the sample is below ~1 µm, the absorption of the sample is overestimated due to multiple reflections in the layer. Maley et al. [20] have proposed to correct the hydrogen content using the following formula (d < 1 µm):

Equation 12

$$c_H^{corrected} = \frac{c_H^{uncorrected}}{1.72 - 0.7 \cdot d[\mu m]} .$$

Figure 7 shows a typical IR absorption spectrum of an a-SiC:H sample together with assignments of the major absorption bands, according to [21,22]. Information on the bonding configuration of hydrogen or, for alloyed films carbon or germanium, in the amorphous network can be deduced from the spectrum (Figure 7). Of special importance is the region around 2000-2100 cm^{-1}. The Si-H stretch mode for singly bound hydrogen lies at 2000 cm^{-1}, whereas Si-H_n vibrations or Si-H on inner surfaces are measured at 2080 cm^{-1}. The latter is the fingerprint of hydrogen that is bound in voids and therefore an indicator for a porous network. Therefore the so-called microstructure factor R is a useful parameter to describe the

mechanical density of an a-Si:H sample. It is defined as the ratio of the integrated 2080 cm^{-1} peak to the sum of the 2000 cm^{-1} and 2080 cm^{-1} peaks:

Equation 13

$$R = \frac{I_{2080}}{I_{2080} + I_{2000}}$$

Good correlation between the microstructure factor R and the performance of solar cells both, in the initial and the light-soaked state, has been reported by Guha et al. [23].

I.4. Characterization of solar cells

I.4.I. I-V measurements

The basic characterization method for a solar cell is the measurement of the current-voltage curve under illumination. This was done at 25°C and using a double source Solar Simulator (Wacom WXS-140S) which provides light of 100 mW/cm^2 intensity with a spectrum close to the global AM 1.5 solar spectrum (standard test conditions). A schematic

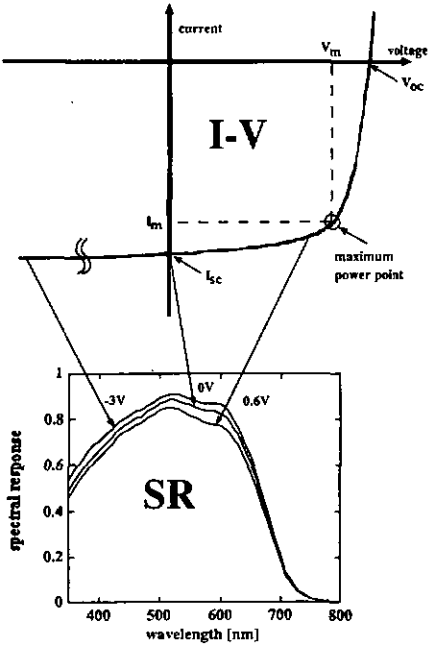

Figure 8: Schematic I-V curve of an a-Si:H solar cell under illumination.

I-V curve for an a-Si:H solar cell under illumination is given in Figure 8.

V_{oc} and I_{sc} are open circuit voltage and short circuit current density, respectively. V_m and I_m are voltage and current at the maximum power point. The maximum power point is the point on the I-V curve where the output power, i.e. the product of voltage and current is maximal. The fill factor FF is defined as the ratio of $V_m \cdot I_m$ and $V_{oc} \cdot I_{sc}$:

Equation 14

$$FF = \frac{I_m V_m}{I_{sc} V_{oc}}$$

The solar cell efficiency η is the maximum electric output power density ($=V_m \cdot I_m$) divided by the power density of the illumination which is usually taken to be 100 mW/cm^2, corresponding to the AM 1.5 intensity:

Equation 15

$$\eta = \frac{I_{sc} V_{oc} FF}{I_{light}}$$

I.4.2. Spectral response measurements

The spectral response (SR) measures the probability for an incident photon to create a free carrier that reaches the contacts and contributes to the cell current. The spectral response value corresponds to the probability that a photon is absorbed within the solar cell, times the probability that a light-generated carrier reaches the external contacts without recombining within the i-layer. At large negative bias voltages virtually all light-generated carriers reach the contacts due to the large internal electric field. Therefore the effects of carrier generation and collection can be separated. By normalizing the spectral response curve under I_{sc} conditions or at small forward voltages to the spectral response at, e.g. –3 V, one can obtain qualitative information on the distribution of the electric field in the solar cell (see, e.g.,

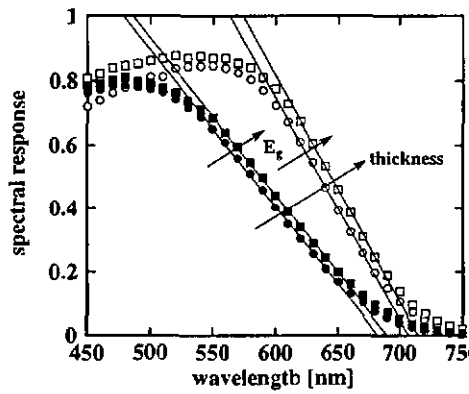

Figure 9: Measured spectral response curves for solar cells of 150 nm and 450 nm i-layer thickness and optical gaps of ~1.88 eV and ~1.92 eV.

section III.4.3).

Spectral response measurements between 350 nm and 800 nm were performed using a probe beam spot smaller than the cell surface. As the number of photons within the probe beam is measured with a reference detector, the integration of the measured curve can be used to determine the cell current independently of the effective cell surface. The SR value obtained in our measurements is the product of internal quantum efficiency and optical losses due to reflection, transmission of glass, TCO and p-layer, and absorption at the back contact. Multiplication of the measured SR curve with the solar spectrum (number of photons per wavelength) and integration over all wavelengths yields the same current density that would be measured by an I-V measurement with an ideal solar spectrum. Most values for the I_{sc} current density given throughout this work are determined by integration of the SR curve rather than by I-V measurements where the exact active cell area is rather difficult to determine.

The influence of the optical gap of the i-layer on the solar cell current can be studied in spectral response measurements. The optical gap on the one hand and the i-layer thickness on the other hand mainly influence the decrease of the SR curve in the red wavelengths region (Figure 9). A variation in the optical gap for constant i-layer thickness leads to an almost parallel shift of the SR curve in the red. The decrease of the SR shifts, for all i-layer thicknesses, to shorter wavelengths with increasing optical gap of the intrinsic layer. An increase in the i-layer thickness, in contrast, leads to a changed slope of this decrease. The linear fits for a given optical gap can be thought to intersect in a common point; increase in i-layer thickness leads to "clockwise turn" of the SR decrease around this point.

I.4.3. Solar cell degradation

Solar cells were light-soaked at 50°C and under open circuit conditions for 1000 h. Photo-luminescence tubes with a near-daylight spectrum were used as light sources. The intensity for the solar cell degradation was adjusted to 100 mW/cm^2, corresponding to AM 1.5 intensity. In some early experiments with a-SiC:H solar cells we used Na high pressure lamps with 100 mW/cm^2 intensity.

II. Intrinsic material

II.1. a-SiC:H

II.1.1. Introduction

Hydrogenated amorphous silicon has been developed rapidly since the discovery of doping by Spear and LeComber in 1975 [24] and of the a-Si:H solar cell by Carlson and Wronski in 1976 [4]. Early on, Spear and coworkers [25] also reported experiments on the alloying of a-Si:H with carbon and germanium. Carbon alloying was found to increase, germanium alloying to decrease the optical gap of the resulting alloy. The amorphous network allows for a continuous variation of the carbon content in the material; thereby one can obtain, in principle, every value between that of a-Si:H and that of amorphous carbon. Unfortunately, a-SiC:H prepared from conventional glow-discharge deposition exhibites opto-electronic properties which deteriorate rapidly with increasing degree of carbon alloying [26,27]. Matsuda and coworkers discovered that H_2 dilution of the plasma resulted in a-SiC:H material with considerably improved photo-sensitivity [28]. Since then glow-discharge deposited a-SiC:H has been studied in many laboratories [e.g., 29-39].

In solar cells, a-SiC:H alloys are used for different purposes. In all cases, one makes use of the fact that alloying with carbon increases the optical bandgap of the resulting amorphous material. A-SiC:H alloys were first applied in the p-layer of "superstrate" type p-i-*n* solar cells [40-44]. Carriers generated in the heavily doped p-layer can not contribute to the photo-current in the cell. Widening of the p-layer bandgap by carbon alloying reduces the light absorption and thereby the current loss due to absorption in the p-layer. Therefore, the current in the cell is remarkably enhanced when the p-type doped a-Si:H layer is replaced by an a-SiC:H window layer.

Soon after, the insertion of a thin (so-called buffer-) layer with increased optical gap at the p/i-interface was found to increase the open circuit voltage of the solar cell [45,46]. The increased optical gap of this buffer layer compared to the intrinsic, active layer of the solar cell was obtained by carbon alloying. The current understanding of the mechanism leading to the V_{oc} enhancement is that the band-offset at the conduction band edge between the wide-gap a-SiC:H-layer and the intrinsic layer prevents electrons from diffusing back to the p-layer and recombining instead of drifting to the n-layer. Such back-diffusion takes place mainly close to V_{oc}-conditions where the electric field within the i-layer is very small. Enhanced recombination in or close to the p-layer, in its turn, affects the V_{oc} of the solar cell.

a-SiC:H alloys can also be used as active layers in p-i-n solar cells [31,47-52]. The widening of the optical bandgap in the absorbing layer reduces the amount of absorbed photons and therefore the current, but increases the voltage of the device due to a higher built-in voltage. Such high-bandgap solar cells are mainly interesting as top cells of tandem or triple stacked solar cells.

In this work, the last-mentioned applications, i.e. the application of a-SiC:H alloys for buffer layers (III.4.2) and as active layers in p-i-n solar cells are discussed (III.2). After an assessment of the material properties of VHF-deposited a-SiC:H alloys, the behavior of such layers is studied in the device with a special emphasis on the stability against light soaking.

Let us finally note that the application of a-SiC:H alloys in the context of a-Si:H solar cell technology is only a small aspect of this highly versatile material which is used in many other fields in modern technology. Applications which are in some relation to the work described here are, among others, light-emitting diodes [e.g. 53] or PV-driven electrochromic windows [54,55].

II.1.2. Material study

Intrinsic layers of amorphous hydrogenated silicon carbon alloys were deposited from silane (SiH_4) and methane (CH_4) as feedstock gases. The choice of methane was motivated by the fact that the best material reported in the literature is made from CH_4 with H_2 dilution [33,35]. Furthermore, CH_4 was readily available in the laboratory. Most other laboratories also use methane as carbon precursor gas. Yet other carbon sources such as ethylene (C_2H_4) [56], acetylene (C_2H_2) [39,57], di- and trisilylmethane [35,58,59], which are both not commercially available, or aromatic carbon sources [32] have also been studied. However, none of the alternative carbon precursor gases has proven to result in material quality superior to a-SiC:H made from CH_4 and SiH_4 with H_2 dilution. In the present study, the methane fraction in the gas phase ($= [CH_4]/([SiH_4]+[CH_4])$) was varied between 0 and 90 %. Hydrogen dilution of the deposition gases was varied between no dilution and a dilution ratio ($= [H_2]/([SiH_4]+[CH_4])$) of 20. Gas fluxes were between five and 20 sccm for SiH_4 and CH_4 and up to 100 sccm for H_2. The intrinsic films grown for the material study were made in a single-chamber reactor without load-lock. The input power (as measured by a power-meter between the generator and the matching network) was 30 mW/cm^2 in most cases. Some films were deposited with 60 mW/cm^2 in order to study the influence of a variation of the deposition power. Substrate temperature and deposition pressure were held constant at 235°C and 0.4 mbar, respectively. Table 1 gives an overview on the different sample series, which were deposited and characterized within this material study.

The purpose of this study of intrinsic a-SiC:H material was to investigate some basic material parameters and to compare our data obtained with VHF deposition to results

Dilution $H_2/(CH_4+SiH_4)$	Power density [mW/cm^2]	Symbol
0	30	■
5	30	□
10	30	●
10	**60**	△
20	30	▽

Table 1: The sample series investigated in this work. The symbols are used throughout this work to refer to the series.

reported in the literature. Once we had a promising process window, further optimization of the intrinsic material was done in the solar cell (section III.2) rather than as an extensive material study.

II.1.2.1. Optical properties

In order to study the influence of various methane fractions in the gas phase on the optical gap of the resulting a-SiC:H layers, we varied the methane fraction in the gas phase between zero (unalloyed a-Si:H films) and 90 %. Additionally, different hydrogen dilutions of the gas (dilution ratios 0, 5, 10, and 20) were applied in order to study its influence on the material quality.

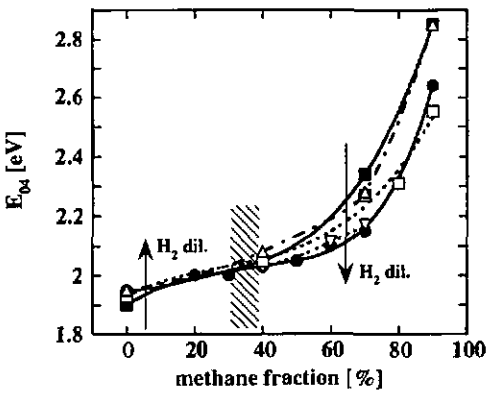

Figure 10: Optical gap E_{04} as a function of the methane fraction in the gas phase for the sample series of Table 1. Symbols are explained in Table 1.

The optical bandgap E_{04} increases for all sample series with increasing concentration of methane in the gas phase (Figure 10). The increase in the optical bandgap is relatively moderate for CH_4 fractions of up to ~40 %. For higher methane fractions in the gas phase, the increase in the optical gap is much more pronounced. The influence of H_2 dilution is different in the two regions. Below ~40 % CH_4 fraction, the optical gap increases with H_2 dilution for constant CH_4 fraction. Even for unalloyed films (0 % CH_4), the optical bandgap E_{04} increases from 1.9 eV (standard a-Si:H) to ~1.95 eV upon H_2 dilution. This very interesting point will be discussed in more detail in section II.2.2.1 of this work. When the CH_4 concentration in the gas phase exceeds ~30 %, the influence of the H_2 dilution on the optical gap is opposite: for a given CH_4 concentration the optical bandgap decreases with increasing H_2 dilution ratio. Increasing the power density to 60 mW/cm^2 at a H_2 dilution ratio of ten does not influence the optical bandgap for films deposited from pure SiH_4 and for films deposited with a small CH_4 fraction. For higher CH_4 fractions (≥30 %), however, the values for the optical bandgap of this series join that of the films deposited without dilution at lower power. We therefore conclude that deposition power and H_2 dilution have opposite effects on the optical properties of a-SiC:H films, i.e. an increase in power density has the same effect as a reduction of the H_2 dilution ratio. This observation fits with the current understanding of the mechanism of H_2 dilution. Hydrogen is believed to enhance the mobility of impinging species on the growing surface on the one hand and to etch the surface during growth on the other hand. Both effects result in a more ordererd and denser structure [28]. Deposition at higher power and hence higher growth rate leave less time for the growing surface to arrange in a highly ordered way and result therefore in a "more amorphous" film. In Figure 10 we observe two regions: up to

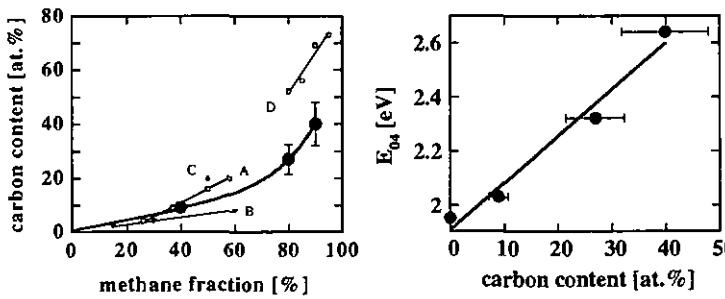

Figure 11: Carbon content in a-SiC:H films deposited with a H_2 dilution ratio of ten as a function of the methane fraction in the gas phase (left). Values from the literature are given for comparison. A: Schmidt et al. [62], B: Matsuda et al. [28], C: Zedlitz et al. [61], D: Vincenzoni et al. [63]. Optical gap E_{04} as a function of the carbon content for the same films (right). Error bars indicate an estimated experimental error of ±20 %.

a CH_4 fraction of 30-40 %, the increase in the optical gap is moderate, indicating a low degree of alloying. Hydrogen dilution results, as in the case of a-Si:H (section II.2.2), in a moderate increase of the optical gap. For CH_4 fractions exceeding 30-40 %, the optical gap increases strongly, which indicates enhanced carbon-incorporation.

This is confirmed by measurements of the carbon content of a few films by X-Ray Photoelectron Spectroscopy (XPS) measurements (Figure 11) [60] and comparison to data from the literature. First, one observes that the carbon content in the film is much smaller than the methane fraction in the gas phase. Even the film deposited with 90 % CH_4 in the gas phase contains less than 50 % carbon. In fact, it has been stated that in a low-power RF regime CH_4 is not directly dissociated in the plasma but via excited SiH_x^* radicals [37,61] limiting thereby the carbon content to 50 %. Our data are quite consistent with data from the literature, taking into account different experimental conditions and various measurement techniques. Schmidt et al. [62], Matsuda et al. [28], and Zedlitz [61] all report carbon contents below 20 at.% for methane fractions in the gas phase up to 60 %. Vincenzoni et al. [63] report carbon content as high as 73 at.%. In their case, deposition is performed in a high-power regime, the excitation power of 300 mW/cm^2 is, e.g. ten times the power generally used in this study. The shape of the curve in Figure 11 (left) is quite similar to the E_{04} (CH_4) curves plotted in Figure 10 with a very moderate increase for small CH_4 fractions and a steepening of the curve for larger amount of CH_4 in the gas. Plotting E_{04} as a function of the

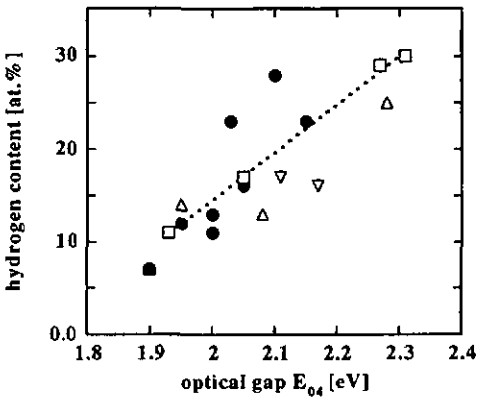

Figure 12: Hydrogen content [at.%] in the a-SiC:H films for various H_2 dilution ratios as a function of the optical gap E_{04}. The values were obtained from integration of the 640 cm^{-1} (Si-H) IR absorption peak and do therefore not take into account hydrogen bonded to carbon.

carbon content in the material, one obtains a rather linear dependency as shown in Figure 11 (right). Let us note that the maximum in the optical bandgap is usually obtained for a carbon content of ~60 % [64,65]. For even higher carbon content in the material, the optical gap decreases.

We have determined the hydrogen content in the films by integrating the 640 cm^{-1} IR absorption peak. The hydrogen content increases with increasing optical bandgap energy (Figure 12). There is no consistent tendency for the hydrogen content for different H_2 dilution ratios, but a general trend of increasing hydrogen content in the samples grown with an increased CH_4/SiH_4 ratio and therefore an increased optical gap. Integration of the Si-H IR absorption peak does not take into account hydrogen bonded to carbon. One would have to sum up the portion of H bonded to Si and to C in order to obtain the exact hydrogen content in the material. The amount of H bonded to C is, however, found to be small for samples with optical bandgaps up to 2.0 eV [22], corresponding to E_{04}~2.15 eV.

II.1.2.2. Material quality and hydrogen dilution

For the application of these a-SiC:H alloys in opto-electronic devices, such as solar cells, the material certainly needs to fulfill other requirements than only a desired value for the optical gap. The opto-electronic quality of the material and especially the stability against light soaking are very important criteria. A good tool for a first assessment of the material quality is IR absorption spectroscopy. A necessary, but certainly not a sufficient requirement for good a-SiC:H material is a low value of the so-called microstructure factor R (section I.3.3). Experience tells that a material with a strong 2080 cm^{-1} absorption peak can directly be discarded because its as-deposited and light-soaked material quality does not qualify for the application in solar cells. In contrast, additional information and especially light soaking experiments are required for material with a low value of the microstructure factor in order to judge on the suitability of that given material.

Figure 13 shows the IR absorption spectra in the 2000 cm^{-1} region for samples deposited with 40 % CH_4 in the gas phase and H_2 dilution ratios of 0, 10 and 20. Clearly, the peak at 2080 cm^{-1} is predominant in the case of the a-SiC:H material deposited without H_2 dilution. This peak decreases while the peak at 2000 cm^{-1} increases when the H_2 dilution ratio is increased, indicating a denser structure of the material. Carbon alloying, however, causes a shift of the Si-H stretch mode vibration from 2000 cm^{-1} to 2080 cm^{-1} due to the electronegativity of the carbon substituent. [22,66]. This results in an increase of the 2080 cm^{-1} absorption, which in this case is not entirely due to SiH_n clusters. In consequence, the value of the microstructure factor of a-SiC:H alloys is slightly overestimated. Yet, the importance of the effect is believed to be relatively small at low C concentrations [67,68] and we can conclude from Figure 13 that H_2 dilution clearly results in lower values of the

microstructure factor for a-SiC:H alloys. Let us note, however, that H_2 dilution results in a slight decrease of the optical gap from 2.05 eV for the sample deposited without dilution to 2.03 eV for the films deposited with dilution ratios of 10 and 20. The beneficial effect of H_2 dilution is therefore reduced to some extent as slightly more carbon would have to be incorporated for the diluted films in order to obtain the same optical bandgap.

Another criterion for an evaluation of the material quality is the slope of the valence band

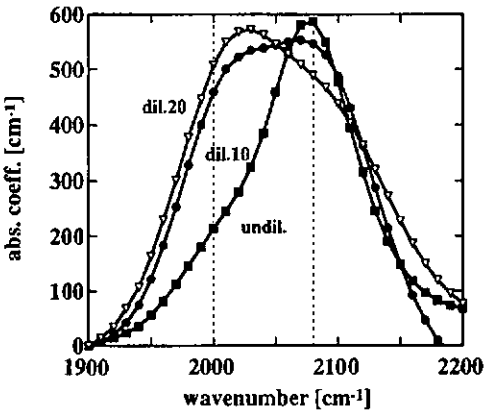

Figure 13: IR absorption spectra in the 2000 cm^{-1} and 2100 cm^{-1} region for three samples deposited from 40 % CH_4 and hydrogen dilution ratios zero (E_{04} = 2.05 eV), 10 (E_{04} = 2.03 eV) and 20 (E_{04} = 2.03 eV).

tail ("Urbach energy"). The Urbach energy is a measure for the disorder in the material and is determined by measurements of the absorption coefficient for energies smaller than the optical bandgap, such as PDS or CPM. Here again, a small value for the tail slope is a necessary but not a sufficient condition for material of good quality. With increasing values of the optical bandgap, an increase in the Urbach energy, as determined here from PDS spectra, is observed. H_2 dilution results in considerably reduced values of the Urbach energy: for samples prepared with a H_2 dilution ratio of ten, the Urbach energy remains, in contrast to undiluted samples, well below 70 meV for bandgap energies of up to 2.1 eV (Figure 14).

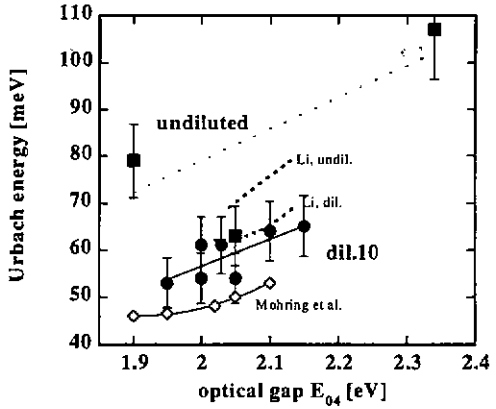

Figure 14: Urbach energy as determined from the PDS absorption spectrum as a function of the optical gap E_{04} for samples deposited wihtout H_2 dilution and with a hydrogen dilution ratio fo ten. For comparison we show values reported by Mohring et al. [33] and Li [47]. Error bars indicate an estimated experimental error of ±10 %.

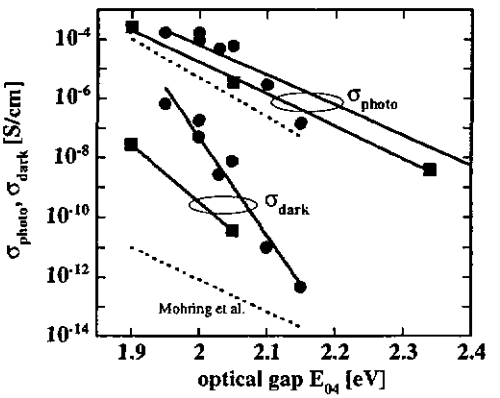

Figure 15: Photo- and dark-conductivities as a function of the bandgap energy E_{04} for two series, deposited without hydrogen dilution and with a hydrogen dilution ratio of 10. For comparison we show values reported by Mohring et al. [33] for (AM 1) photo-conductivity and dark-conductivity (dashed lines).

We included in Figure 14 values reported by Mohring et al. (University of Stuttgart) [33] which to our knowledge are the best values reported in the literature to date as well as data for a-SiC:H material made by Li (Solarex) [47] which has been incorporated into p-i-n solar cells with quite encouraging results. The optical gap was converted into E_{04} values by adding 150 meV to the reported values of the "optical" gap, as justified in Figure 4 (section I.3.1.2). Urbach energies for our VHF-deposited H_2 diluted a-SiC:H material are slightly higher than the astonishingly low values for the DC-deposited material of the Stuttgart group, but are comparable to values obtained by Solarex with H_2 dilution. Urbach energies for samples prepared without H_2 dilution are much higher.

Figure 15 shows photo-conductivity and dark-conductivity values for two sets of samples, one deposited without H_2 dilution and one deposited with a dilution ratio of 10, as a function of the optical bandgap E_{04} in the as-deposited state. The photo-conductivity is measured under the white light of a tungsten lamp with an intensity of 100 mW/cm^2 and is not corrected for generation rates. The decrease in photo-conductivity with increasing optical gap is therefore partly due to a reduced generation rate. Hydrogen dilution yields slightly higher values of the photo-conductivity. The dark-conductivity decreases strongly with increasing optical bandgap due to the exponential dependence of the dark current on the bandgap energy. The films deposited with H_2 dilution exhibit dark-conductivities which are about two orders of magnitude higher than for films of the same bandgap but deposited without dilution. Most probably, n-type doping due to oxygen incorporation into the films

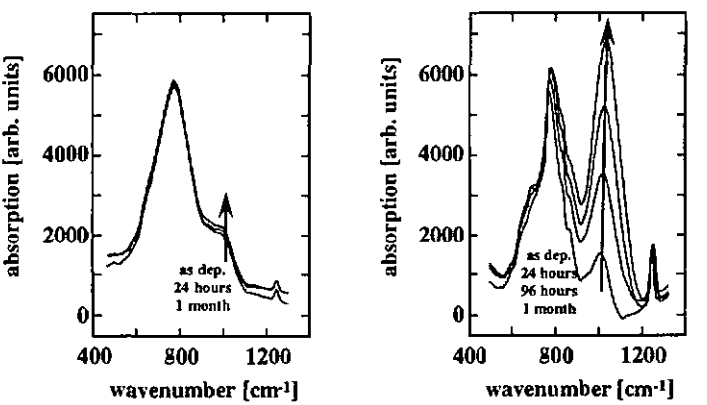

Figure 16: Infrared transmission spectra measured at different times after deposition for films deposited with a H_2 dilution ratio of ten (left) and without dilution (right). Shown is the region around the Si-O absorption peak at ~1000 cm^{-1}.

deposited with H_2 dilution is the reason. Note that the a-SiC:H films have been deposited in a single-chamber reactor without load-lock, a fact, that certainly favors oxygen contamination. The increase in σ_{ph} with H_2 dilution may therefore be partially due to a shift of the Fermi level because of oxygen doping as indicated by the increase of the dark-conductivity. Figure 15 includes data for the Stuttgart a-SiC:H material. E_{04} values are again obtained by simply scaling E_{opt} values by 150 meV. The AM 1 photo-conductivity values reported are, within experimental error, comparable to our data, the dark-conductivity, however, is 2-3 orders of magnitude lower, even for the undiluted samples, resulting in a higher photo- to dark-conductivity ratio.

Samples deposited without H_2 dilution with a high carbon content reveal a post-deposition oxidation of the layers. A sample deposited with 90 % CH_4 and no H_2 dilution shows a strong increase of the SiO IR absorption peak at 1000 cm^{-1} with time after deposition (Figure 16, right). This indicates an open void structure of the material, which, in consequence, allows oxygen to penetrate. Similar observations are reported in [22]. Samples prepared with the same CH_4 fraction but employing hydrogen dilution do not show this feature (Figure 16, left). For samples prepared with lower CH_4 fractions in the gas phase, no oxidation was observed, even when no H_2 dilution was applied. This is further evidence indicating that hydrogen dilution of the plasma results in denser material structures for material deposited with a large amount of CH_4.

The deposition rate is remarkably increased for the VHF deposition technique compared to conventional RF plasma excitation. There is little information on growth rates for DC deposition in the literature; Zedlitz et al. [61] report growth rates of 2.3 Å/s for DC at

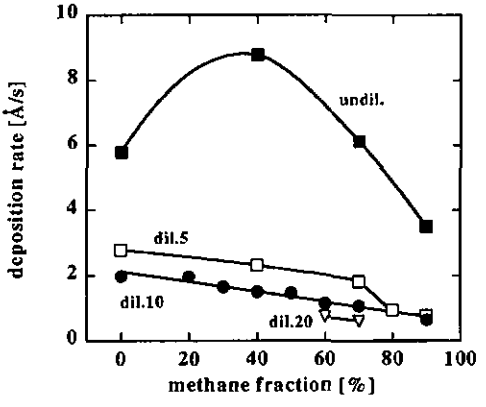

Figure 17: Deposition rate as a function of the CH_4 fraction in the gas phase for the sample series of Table 1.

50 mW/cm^2 and 17 Å/s at 180 MHz excitation frequency with input power of 45 mW/cm^2 and using H_2 dilution. We observe an increase in the deposition rate with increasing methane fraction (up to 40 %) for samples deposited without H_2 dilution, which is in contrast to RF deposition. A power density of 30 mW/cm^2 yields a deposition rate of 8.6 Å/s for 40 % CH_4 when no H_2 dilution is employed. The decrease for higher CH_4 fractions can be explained by the fact that the density of excited SiH_n^* ions, which are responsible for the decomposition of CH_4 in the plasma, decreases with increasing CH_4 fraction. Hydrogen dilution reduces the deposition rate strongly. For a H_2 dilution rate of 10 and 40 % CH_4, the deposition rate is 1.6 Å/s for otherwise same conditions. In the case of H_2 dilution during the growth, the deposition rate decreases monotonically with increasing methane content in the gas. For those samples, the growth rate decreases for a given CH_4 content with increasing H_2 dilution ratio.

II.1.3. Discussion and conclusions

Our material study did not reveal any significant difference of a-SiC:H material deposited at 70 MHz compared to "typical" RF- or DC-deposited a-SiC:H reported in the literature. The only exception is a higher growth rate for comparable values of the plasma excitation power for VHF compared to RF. Previous studies of VHF excitation for a-SiC:H deposition [61,69] suggested, however, that the VHF-deposition technique slightly increases carbon incorporation in the layers.

Hydrogen dilution of the process gas increases the optical gap for films deposited with a low methane fraction (<30 %) and reduces the gap for material deposited with higher CH_4 fraction (exceeding 30 %). H_2 dilution at the same time considerably improves the material quality. The beneficial effect on the material quality is most striking in terms of the Urbach energy. Values between 80 meV and 100 meV without dilution are reduced to values between 50 meV and 65 meV with H_2 dilution, depending on the CH_4 fraction. H_2 dilution also yields lower values of the microstructure factor when materials with the same methane fraction in the gas are compared. However, as H_2 dilution reduces the optical gap for CH_4 fractions exceeding ~30 %, the improvement in the microstructure factor is slightly reduced when comparing materials with the same optical bandgap.

In conclusion, we could confirm that CH_4 as carbon source together with H_2 dilution results in a-SiC:H material of reasonably good quality as long as the material contains a relatively small amount of carbon, i.e. as long as the optical gap is only moderately increased. The quality of such a-SiC:H material is, however, already for a small degree of alloying considerably reduced compared to state-of-the-art a-Si:H. For samples with a gap larger than 2.0-2.1 eV the material properties deteriorate very rapidly, even when strong H_2 dilution is employed.

Most probably, the investment of additional research on such a-SiC:H alloys could result in material with further improved electronic quality. Our goal was, however, to proceed, after a first assessment of the a-SiC:H deposition by means of the VHF technology, rapidly towards the fabrication of a-SiC:H solar cells. Further optimization has therefore been done within the solar cell, as will be described in section III.2 of this work. In conclusion to this material study, we choose a material deposited with 40 % CH_4 and a H_2 dilution ratio of 10 (resulting in an optical gap E_{04} of about 2.03 eV) as the starting point for our solar cell research.

II.2. a-Si:H

II.2.1. Introduction

The search for an a-Si:H material with improved stability against light soaking has ever been going on since the first report of the Staebler-Wronski-effect in 1977 [5]. Even though considerable amounts of money and time have been invested to understand the exact mechanism, many questions remain unanswered today and the number of models trying to explain the metastability exceeds the number of a-Si:H solar cell producers by far. On the other hand, the a-Si:H solar cell technology has learned to "live with the effect". Technological approaches such as the stacked or tandem a-Si:H based solar cell (chapter IV) or the possibility to make the solar cells thinner due to highly efficient light-trapping have largely contributed to today's increased stabilized efficiencies.

Until very recently, many groups limited their research to the development of intrinsic a-Si:H material without ever making a solar cell. The choice of a suited material parameter for the optimization, however, is quite problematic, because a solar cell is an ambipolar device, i.e. both types of charge carriers have to be taken into account. Measurement of the $\mu_0\tau_0$ parameter together with a controlled degradation procedure [70] is believed to yield reliable information on the light soaking behavior of a new material in a solar cell. We therefore based the characterization of the stability of our a-Si:H materials on the measurement of this $\mu_0\tau_0$ parameter in a saturated light-soaked state obtained by pulsed-laser degradation.

Many different approaches to obtain a-Si:H material of enhanced stability have been reported in the literature. However, the only technology which has proven to result in a-Si:H with enhanced stability against light soaking and which is mature for application on the production level is the hydrogen dilution technique. Guha and coworkers first reported in 1981 [71] that H_2 dilution of the SiH_4 plasma resulted in a-Si:H with improved stability. Since then the technique has become widespread and is today employed by most major a-Si:H solar cell manufacturers [e.g., 72,73] and many research laboratories. H_2 dilution fulfills a double role in the achievement of higher stabilized efficiencies of a-Si:H solar cells. Beyond the fact that material deposited with H_2 dilution is more stable against light-induced degradation, H_2 dilution allows the deposition of a-Si:H at lower than standard deposition temperatures without deterioration of the material quality. Increased values for the optical gap and thereby enhanced V_{oc} values can thus be obtained.

In the following sections, the effect of H_2 dilution on the film properties is described for the case of our VHF plasma excitation at 70 MHz. We investigated the material properties for various substrate temperatures and H_2 dilution ratios to provide a generalized picture of

a-Si:H deposition using the VHF technique, with special emphasis on the optical absorption and the stability as the key issues for solar cell applications. Finally, we directly compare VHF plasma excitation to standard RF (13.56 MHz) plasma excitation and deposition using a DC plasma. The question as to whether an interdependence between stability and growth rate exists is of special interest in this context.

II.2.2. Hydrogen dilution and influence of the substrate temperature

It has already been mentioned above (section II.1.2.1) that H_2 dilution results in an increase of the optical bandgap of a-Si:H layers for a given substrate temperature during deposition. The optical bandgap E_{04} increases for unalloyed films from ~1.9 eV (standard a-Si:H) to ~1.95 eV when a H_2 dilution ratio of ten is applied to the plasma at standard temperature (Figure 10). The initial motivation to investigate H_2 dilution was therefore to obtain p-i-n solar cells with increased V_{oc} when employing H_2 dilution for the i-layer. We furthermore seeked an answer to the question as to whether the enhanced stability observed for RF deposition [71] could be reproduced also for the VHF deposition technique.

II.2.2.1. Optical properties and hydrogen content

The substrate temperature during deposition influences the optical absorption properties of the resulting a-Si:H material. The optical bandgap of the material decreases with increasing temperature of the substrate during deposition. Figure 18 shows absorption spectra as a function of the photon energy for intrinsic a-Si:H deposited at substrate temperatures between 195°C and 300°C without H_2 dilution. Indicated temperatures are calibrated temperatures as determined by direct measurement on the substrate for conditions corresponding to those during deposition, however without plasma. The absorption spectra are determined from transmission and reflection measurements in the high-energy range and from PDS measurements in the low-energy range. One observes that the absorption curve is shifted in a parallel manner over the whole range of photon energies, except for the defect absorption, when the substrate temperature is increased from 195°C to 300°C. For a given photon energy, the absorption coefficient increases with increasing deposition temperature.

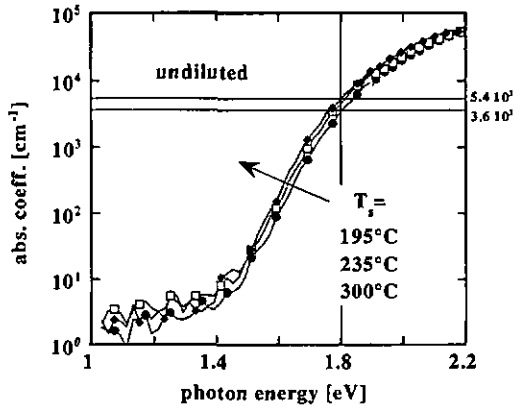

Figure 18: Absorption spectra as measured by transmission/reflection ($h\nu > 1.8$ eV) and PDS ($h\nu < 1.9$ eV) for three substrate temperatures T_s without hydrogen dilution.

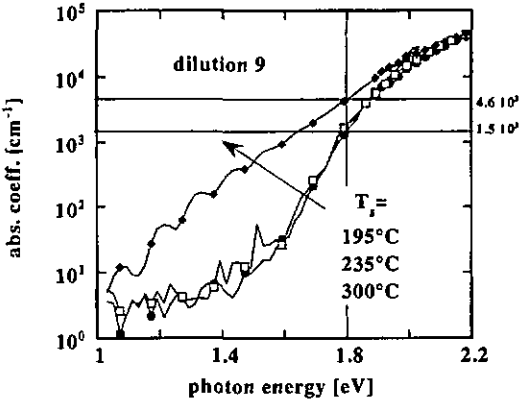

Figure 19: Absorption spectra as measured by transmission/reflection ($h\nu > 1.8$ eV) and PDS ($h\nu < 1.9$ eV) for three substrate temperatures T_s with a hydrogen dilution ratio of nine (right). Note that the sample at T_s = 300°C shows partially microcrystalline absorption.

Hydrogen dilution of the process gas during deposition decreases the optical absorption of the resulting films. Figure 19 shows as an example the absorption spectra of films deposited with a H_2 dilution ratio of 9 for the same substrate temperatures as in Figure 18. Here also, the absorption coefficient increases with increasing substrate temperature. However, for the same substrate temperature, the absorption coefficient is lower for the diluted films than for the films deposited without H_2 dilution. E.g., the absorption coefficient for material deposited at a temperature of 195°C decreases from $3.6 \cdot 10^3$ cm^{-1} without dilution to $1.5 \cdot 10^3$ cm^{-1} at a H_2 dilution ratio of 9 for the photon energy of 1.8 eV. The absorption spectrum in Figure 19 (H_2 dilution ratio of 9) for the film deposited at 300°C indicates that this particular film is microcrystalline. In fact, high substrate temperatures favor microcrystalline growth and reduce the amount of H_2 dilution necessary to obtain microcrystalline films. At standard substrate temperature of 235°C, the onset of microcrystalline growth appears only for H_2 dilution ratios of about 13-15.

Figure 20 shows the optical bandgap E_{04} as a function of the H_2 dilution ratio for a larger set of substrate temperatures. The optical bandgap increases with increasing H_2 dilution ratio and decreases with increasing substrate temperature. The increase in the optical bandgap is an approximately linear function of the H_2 dilution ratio. H_2 dilution reduces the optical bandgap considerably. A H_2 dilution ratio of 9-10 results in about the same increase in the optical bandgap as a reduction of the substrate temperature by 100-150°C.

The optical bandgap of our VHF samples is correlated with the hydrogen content in the

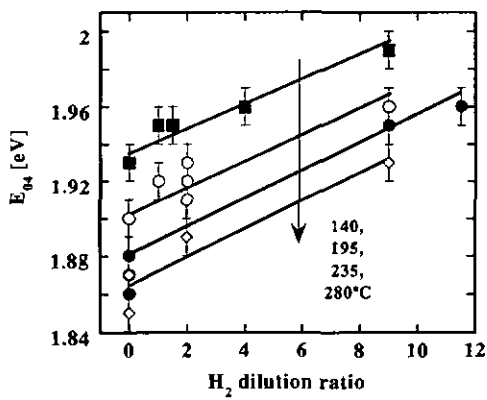

Figure 20: E_{04} values for substrate temperatures between 140°C and 280°C as a function of the hydrogen dilution ratio. Error bars indicate an estimated experimental error of ±0.01 eV.

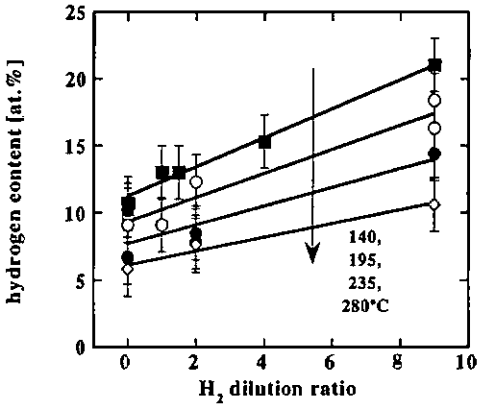

Figure 21: Hydrogen content [at.%] as a function of the H_2 dilution ratio for samples deposited at various substrate temperatures. Error bars indicate an estimated experimental error of ±2 at.%.

amorphous network as determined from the 640 cm^{-1} absorption peak in the infrared spectrum. The hydrogen content increases with increasing H_2 dilution and decreasing substrate temperature (Figure 21). The determination of the H content in the films by evaluation of IR absorption spectra contains some sources of experimental error. The subtraction of the transmission baseline, the fit of the absorption peak with a gaussian distribution, and the determination of the film thickness account for an estimated error on the order of 2 at.% absolute. However, the general tendency is very clear. A high hydrogen content in the film correlates with a high optical gap of the sample. The same tendency had already been observed in the context of a-SiC:H samples (section II.1.2.1 of this work). This correlation is demonstrated in Figure 22.

Taking into account the experimental error for both, optical gap and hydrogen content, a roughly linear relation between optical gap and hydrogen content can be postulated. This linear dependency is valid for all temperatures and H_2 dilution ratios investigated within this work. The fit yields an increase of ~8 meV in the optical gap per at.% hydrogen content in the film.

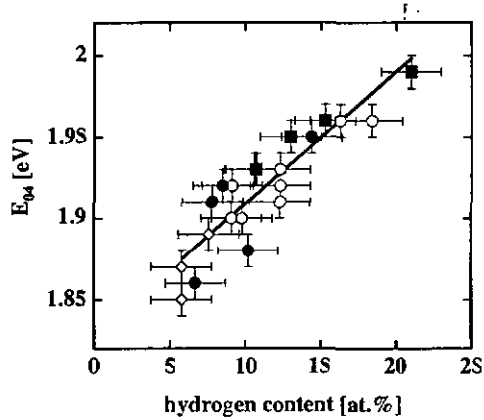

Figure 22: Optical gap E_{04} as a function of the hydrogen content, plotted for the films of Figure 20 and Figure 21. The linear fit for all temperatures and H_2 dilution ratios yields a slope of ~8 meV/at.%.

II.2.2.2. Deposition at low substrate temperatures

Hydrogen dilution plays an important role in the context of a-Si:H deposition at low substrate temperatures. There are different reasons why one would consider to decrease the deposition temperature for a-Si:H below its "standard" value of around 200°C. Firstly, the deposition at lower substrate temperatures yields material with increased optical gap. This can be interesting when one wants to obtain i-layer material for p-i-n solar cells with a high open circuit voltage. In fact, the highest V_{oc} values obtained using H_2 dilution and low substrate temperature for the i-layer deposition (1.04 V) exceed those obtained with a-SiC:H solar cells [74]. Secondly, more and more work is being done in the field of deposition on substrate materials other than glass or stainless steel. Especially polymer substrates are continuously gaining in interest due to their potentially low cost, their lightweight and mechanical properties [75]. However, most polymers do not withstand temperatures of 200°C and therefore necessitate the deposition of a-Si:H at lower substrate temperatures.

When decreasing the substrate temperature below the optimum temperature, the quality of a-Si:H generally strongly decreases. Figure 23 shows the IR absorption spectra in the 2000 cm^{-1} and 2080 cm^{-1} wavenumber region for films deposited at a substrate temperature of 140°C. Clearly, the film deposited without H_2 dilution shows a high microstructure factor of 0.37, i.e. a strong absorption peak at 2080 cm^{-1}, indicating a large void fraction in the material. When adding H_2 to the deposition plasma, films with considerably improved

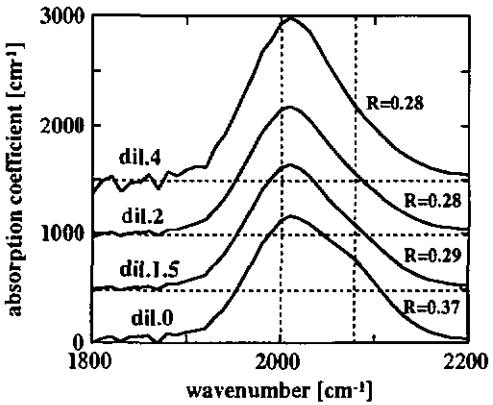

Figure 23: Infrared absorption spectra for a-Si:H layers deposited at 140°C and different H_2 dilution ratios. The spectra are shifted by 500 cm^{-1} with respect to each other. Vertical lines at 2000 cm^{-1} and 2080 cm^{-1} indicate the silicon mono- and polyhydride absorption frequencies. Values of the microstructure factor R are given next to the absorption curves.

microstructure can be obtained, as shown in Figure 23. The 2080 cm^{-1} peak decreases with increasing H_2 dilution. The films deposited with a H_2 dilution ratio of four shows a reasonably low microstructure factor of 0.28, close to what is obtained for "standard" deposition temperature without H_2 dilution.

The fact that H_2 dilution increases the quality of a-Si:H deposited at lower than standard substrate temperatures is also confirmed by the material quality parameter $\mu_0\tau_0$ (section I.3.2.2). Figure 24 shows the $\mu_0\tau_0$ product in the as-deposited state for the sample series deposited at 140°C as a function of the H_2 dilution ratio [76]. $\mu_0\tau_0$ increases with H_2 dilution ratio and clearly correlates with the microstructure factor. At a H_2 dilution ratio of four the gain in $\mu_0\tau_0$ is roughly a factor of four compared to the undiluted film. A $\mu_0\tau_0$ value of $2 \cdot 10^{-7}$ cm^2/V, as obtained by using H_2 dilution four, can be considered to be a value for material of reasonably good quality in the as-deposited state [70].

II.2.2.3. Deposition at enhanced substrate temperature

It has been shown above that the optical gap of an a-Si:H film is directly influenced by the substrate temperature. A higher substrate temperature results in a lower optical gap. This statement has been found to be valid for all H_2 dilution ratios. A smaller optical gap yields

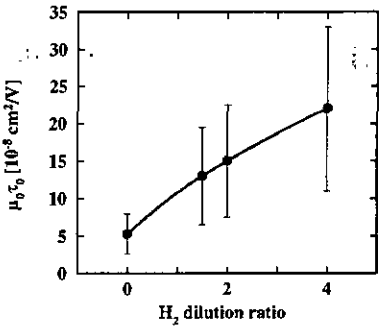

Figure 24: $\mu_0\tau_0$ parameter in the initial state for samples deposited at 140°C and different H_2 dilution ratios. The samples are the same as in Figure 23. The experimental error is assumed to be ±50 %.

enhanced optical absorption which is interesting for solar cell applications. The higher current generation enhances the totally available current density in a solar cell and/or allows for generation of a given current density within a thinner intrinsic layer. Furthermore, the stability of a-Si:H deposited without H_2 dilution increases with increasing deposition temperature as will be shown in section II.2.3.4 below (Figure 32, page 52). Both effects, the enhanced stability of the material together with a higher absorption coefficient and therefore the potential to make thinner cells, bear potential to increase the stabilized efficiency of solar cells. The insertion of intrinsic layers deposited at high temperature in a p-i-n device, however, causes considerable technological problems as will be discussed, together with possible solutions, in section III.4.2.2. Solar cells with intrinsic layers deposited at moderately increased temperature are reported in section III.3.2.

II.2.2.4. Stability

Hydrogen dilution has been shown to increase the stability of RF-deposited intrinsic a-Si:H films [71] and also of solar cells due to enhanced stability of the i-layer against light soaking [77]. The correlation between the stability, i.e. electronic properties of the i-layer material and the performance of a p-i-n solar cell as an entire device has always been a controversial point of discussion. At IMT, the $\mu_0\tau_0$ parameter has been developed as a material parameter which is directly connected to the cell performance in the initial and light-soaked state [14]. This parameter could be shown to be a valuable tool for the evaluation of the material quality. The $\mu_0\tau_0$ parameter combines information on the minority carriers (in an a-Si:H solar cell usually the holes) and the majority carriers (usually the electrons) providing

thereby a quite satisfying image of the electronic transport, both in the layer and the solar cell (see section III.3.1.2). In particular, this assessment is more or less independent of the Fermi level position in contrast to measurements of photo-conductivity and ambipolar diffusion length alone.

Samples of VHF-deposited intrinsic a-Si:H layers, deposited at different temperatures and with various H_2 dilution ratios, have been light-soaked to their stabilized state using pulsed-laser degradation as described in section 1.3.2.2. Measurement of the $\mu_0\tau_0$ parameter in the light-soaked state yielded the results shown in Figure 25 as a function of the H_2 dilution ratio. The $\mu_0\tau_0$ product for the samples deposited without H_2 dilution increases slightly with increasing substrate temperature. We observe a considerable gain of roughly a factor of two for the samples deposited with a H_2 dilution ratio of two compared to the samples deposited without H_2 dilution. The value of $\mu_0\tau_0$ for the samples deposited with dilution two is independent of the substrate temperature in the investigated range between 195°C and 280°C. Increasing the H_2 dilution ratio to a dilution ratio of nine does not increase the stabilized $\mu_0\tau_0$ product further. We conclude therefore, that for VHF-deposition also, H_2 dilution of the SiH_4 plasma results in intrinsic material with enhanced stability against light soaking, i.e. improved electronic transport properties in the light-soaked state. The gain in stability is found already for a relatively small amount of H_2 dilution.

The influence of H_2 dilution of the i-layer on the stability of p-i-n solar cells will be

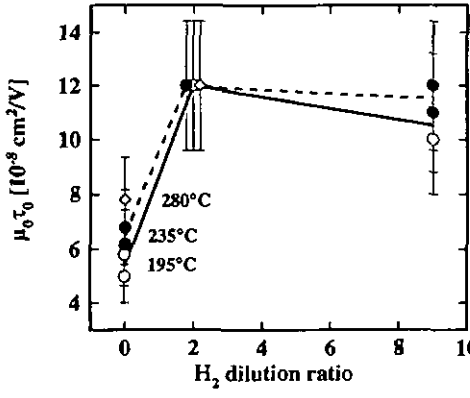

Figure 25: $\mu_0\tau_0$ product as a function of the H_2 dilution ratio in the light-soaked state for samples deposited at different substrate temperatures. Error bars indicate an estimated experimental error of ±20 %.

discussed in more detail in section III.3.1.2 below.

II.2.3. Comparison of VHF, RF and DC plasma excitation

It has first been reported by our group at IMT [78] and later on been confirmed by other groups [79,80] that VHF plasma excitation as used in this work enhances the growth rate of *a-Si:H films without affecting the quality of the material in the as-deposited state. However,* these comparisons extended only over the range from standard 13.56 MHz (RF) plasma excitation to frequencies in the VHF range. The third "conventional" PECVD technology, plasma excitation by a DC source, had so far not been taken into account. Furthermore, the reports were restricted to deposition from undiluted SiH_4 and considered only the material quality in the initial state. In the following we directly compare standard radio frequency (RF, 13.56 MHz) deposition to very high frequency (VHF) deposition at 70 MHz and deposition using a direct current (DC) excitation under similar conditions. Special emphasis is laid on the influence of H_2 dilution, and electronic transport characteristics in the light-soaked state are compared. In the past, all three methods have already demonstrated the potential for producing solar cells with high stabilized efficiency (e.g., [18,81] for RF, [82] for VHF and [83] for DC).

II.2.3.1. Experiments

The intrinsic a-Si:H films reported within this study have been deposited in three different deposition systems. Each of the three systems has been built and optimized for a given excitation frequency. Results reported above for our VHF-deposited films are now compared to data for the two other excitation techniques. DC-deposited films were grown by the author in the i-chamber of a three-chamber PECVD system with load-lock at Princeton University during a one year visit there. A few layers were also deposited using RF excitation in this reactor (referred to as RF(P)). Data on the other intrinsic layers using RF excitation were provided by the group at the Research Center Jülich. Deposition was performed in the i-chamber of a three-chamber system with load-lock in this last case. Table 2 gives an overview of the deposition conditions used for the three plasma excitation techniques.

	Electrode dimensions	Electrode area [cm^2]	El.-substr. distance [cm]	Pressure undiluted films [mbar]	Pressure diluted films [mbar]	Power density [mW/cm^2]
DC	15×15 cm^2	225	1.6	0.67	0.93	22
RF	Ø 13.5 cm	143	1.2	1.33	2.66	30
RF(P)	15×15 cm^2	225	1.6	0.67	-	22
VHF	Ø 13.0 cm	133	1.6	0.35	0.5	30

Table 2: Geometrical dimensions of the electrodes, and deposition conditions.

All temperatures given are true substrate temperatures, as determined by direct measurement on the substrate for conditions corresponding to those during deposition, however without plasma. The plasma excitation power was chosen to be comparable in all three cases. In the DC reactor at Princeton, the plasma burns towards both sides of the powered electrode, due to the triode-configuration of the reactor. The effective electrode surface is therefore twice the value given in Table 2 and the power density of 22 mW/cm^2 is the value of the input power divided by twice the electrode surface. The input power given for RF and VHF deposition was measured by a power meter between the generator and the matching network, and the value for DC deposition is given by current and voltage of the discharge. It has, however, to be taken into account when comparing power densities that in the case of RF and VHF deposition the effective plasma power may be considerably lower than the value read on the power meter. In fact, considerable power losses occur mainly in the matching network. Measurements performed on a deposition system that is quite similar to the one used in the present work for the VHF samples yielded losses close to 50 % at 70 MHz [79]. Such electrical losses depend, however, quite critically on the reactor and deposition conditions and are difficult to quantify.

II.2.3.2. Optical gap and hydrogen content

Influence of the substrate temperature

Optical gap and material properties of the a-Si:H films are strongly influenced by the substrate temperature. We varied the substrate temperature between ~100°C and ~300°C. There is no significant difference for the three excitation techniques. The optical gap of intrinsic a-Si:H films deposited without H_2 dilution decreases with increasing substrate temperature, as has already been reported for VHF above. This decrease approximately is a linear function of the substrate temperature for all three excitation frequencies in the temperature range investigated (Figure 26) with a slope of approximately -55 meV/100 K.

The decrease in the optical gap of the a-Si:H films correlates with a decrease in the H content (c_H) in the films as determined from FTIR spectroscopy (Figure 26). Again, for all three excitation techniques, c_H is an approximately linear function of the substrate temperature in the investigated temperature range (-4.3 at.%/100 K). All excitation frequencies yield comparable values for the optical gap and the hydrogen content. Plotting the optical gap as a function of the hydrogen content (not shown) we obtain dE_{04}/dc_H ~ 6 meV/at.%. For VHF-deposited material and various substrate temperatures and H_2 dilution ratios we had observed a slope dE_{04}/dc_H of approximately 8 meV/at.% (Figure 22); the difference is not very significant considering the scattering of the data.

Influence of hydrogen dilution

We have seen above that all three excitation techniques yield very similar results for samples deposited from 100 % SiH_4. The effect of H_2 dilution, in contrast, depends on the excitation technique (Figure 27). In all three cases, the optical gap E_{04} increases with H_2 dilution. For VHF and RF excitation techniques, this increase is monotonic and almost linear. In the case of RF excitation, a H_2 dilution ratio of 30 results in approximately the same increase in E_{04} as a dilution ratio of ten for VHF (~0.05-0.1 eV). DC deposition exhibits a slightly more complex behavior with H_2 dilution. For low H_2 dilution ratios, the optical gap

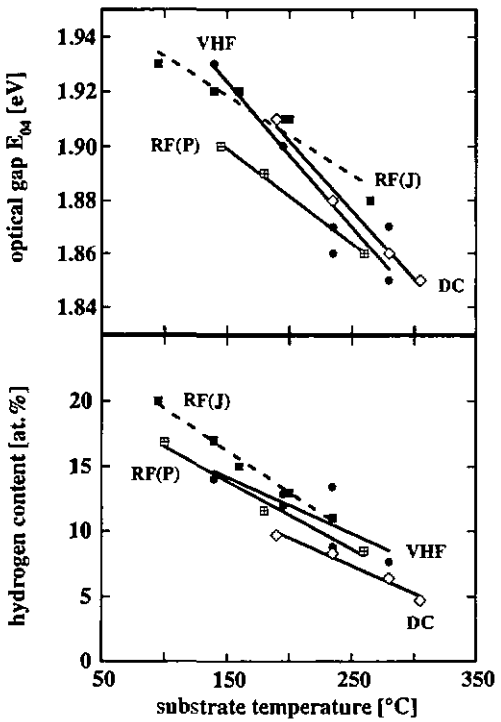

Figure 26: Top: optical gap E_{04} as a function of the deposition temperature for films deposited without H_2 dilution and VHF, RF (Jülich and Princeton) or DC excitation. Bottom: hydrogen content for the same samples. For better legibility we did not plot error bars; the experimental error is estimated to be ±0.01 eV for the optical gap and ±2 at.% for the hydrogen content.

increases moderately and in a similar way as for VHF. Between a dilution ratio of four and six, however, the increase in the optical gap is very steep, followed by an increase to >2.05 eV with further dilution. Sub-bandgap absorption spectra from PDS and UV reflectance measurements [84] indicate that these samples are still purely amorphous and not microcrystalline.

The H content (c_H) of the RF and VHF films increases with increasing H_2 dilution ratio (Figure 27). The increase in c_H is much more pronounced for the VHF samples than for the RF samples, and c_H exceeds here 20 at.% for the highest dilution ratio. On the other hand, we find again for both, RF- and VHF-deposited samples, a correlation between the optical gap and the H content, i.e. a higher optical gap for a higher hydrogen content. H_2 dilution has a relatively small influence on the hydrogen content in the DC-deposited samples for dilution ratios of up to four. For even higher dilution ratios, c_H increases, similar to VHF and RF deposition. Let us note that the determination of the hydrogen content for our DC samples is subject to considerable experimental error. In fact, it turned out that the layer on the crystalline silicon substrate used for IR measurements is, depending on the H_2 dilution ratio, considerably thinner than the layer on the glass substrate. Whereas we do not observe a significant difference in thickness for samples deposited without H_2 dilution, the difference approaches a factor of two for the highest H_2 dilution ratio. Recent experiments with DC plasmas at IMT [85] showed that inhomogeneities on the substrate surface result in inhomogeneities of the plasma, this effect becoming stronger with increasing H_2 dilution ratio. The holder for the crystalline silicon wafer pieces, as used for our DC samples, is made from stainless steel with an opening for the wafer. Even though the plasma could not be observed with the eye at Princeton, it is reasonable to assume a local disturbance of the plasma, explaining the pronounced difference in thickness. The data points in Figure 27 are corrected for this thickness effect. To our knowledge, the only publication on H_2 dilution using DC plasma excitation [86] reports a slight decrease in the H content and a moderately increased optical gap for DC samples deposited with H_2 dilution ratios of up to 10.

Figure 27 (bottom) also shows the microstructure factor for the DC-deposited samples. The microstructure factor exhibits a minimum value around a H_2 dilution ratio of five. This indicates that moderate H_2 dilution improves the material quality in the case of DC excitation whereas too high a dilution results in a high microstructure factor. The exact mechanism behind this behavior is, however, not understood. Let us finally note that the microstructure factor correlates roughly with the discharge voltage at constant plasma power (Figure 34, section II.2.3.4) indicating that a change in the plasma regime might play a role and have consequences on the material quality.

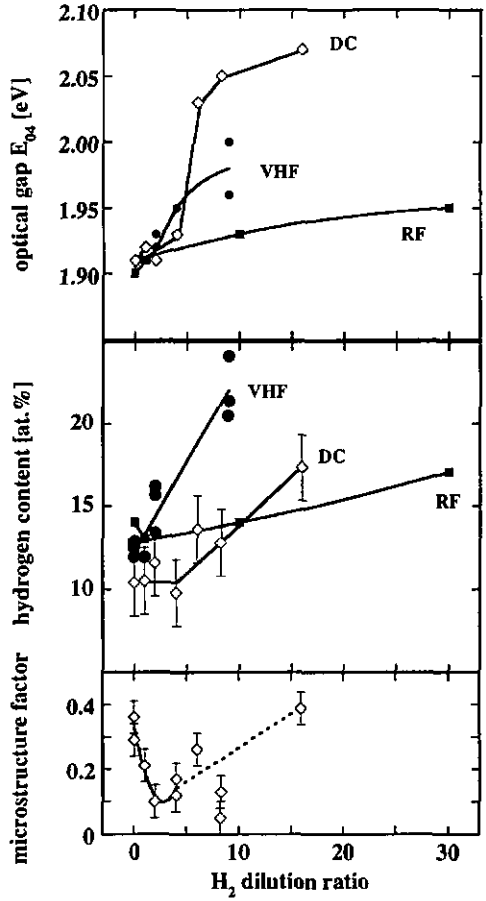

Figure 27: Top: optical gap E_{04} for VHF, RF and DC deposition at a substrate temperature ~200°C as a function of the H_2 dilution ratio of the plasma. All samples in the figure are purely amorphous. Middle: Hydrogen content for VHF, RF and DC-deposited samples as a function of the H_2 dilution ratio. Bottom: Microstructure factor for the DC-deposited samples. For better legibility error bars are plotted only for the hydrogen content and the microstructure factor of the DC films (see text); the experimental error is estimated to be ±0.01 eV for the optical gap and ±2 at.% for the hydrogen content.

II.2.3.3. Growth rate

Figure 28 shows the growth rate of the a-Si:H films as a function of the H_2 dilution ratio (=$[H_2]/[SiH_4]$) for the three excitation techniques and standard substrate temperature of ~200°C. Input power was 30 mW/cm^2 for VHF and RF excitation and 22 mW/cm^2 for DC. We have already mentioned above the difficulty comparing the excitation power for different reactor conditions and excitation frequencies. In our case we have chosen a ~30 % lower input power for DC, thereby taking into account some losses for VHF and RF. If the real losses are higher than 30 %, the growth rate of VHF and RF is underestimated with respect to DC.

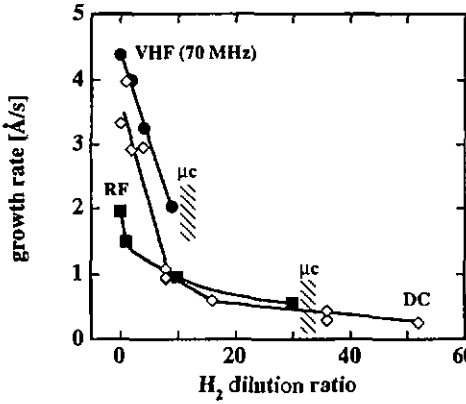

Figure 28: Growth rate for VHF, RF and DC deposition as a function of the H_2 dilution ratio (=$[H_2]/[SiH_4]$). Input power is 30 mW/cm^2 (VHF), 30 mW/cm^2 (RF) and 22 mW/cm^2 (DC). T_s ~200°C.

For films deposited without H_2 dilution, VHF deposition yields the highest growth rate of ~4.5 Å/s, the growth rate obtained with DC excitation is only slightly lower. RF plasma excitation without H_2 dilution yields a growth rate of ~2 Å/s. We observe a quite different behavior for the three techniques when increasing the H_2 dilution ratio. The growth rate for VHF excitation decreases roughly linearly with increasing H_2 dilution ratio. The range of H_2 dilution is very limited for the VHF technique as microcrystalline growth starts (for the prevailing deposition conditions, as used here) already at a dilutioo ratio of ~12. Above a substrate temperature of 200°C, microcrystalline growth sets in at even lower H_2 dilution ratios. The growth rate for RF excitation is much lower and also an almost linear fuoction of H_2 dilution, except for a steep drop by almost a factor of two between pure SiH_4 and dilution

ratio of one. Microcrystalline growth sets in at dilution ratios exceeding 30. For DC excitation, we observe two distinctly different slopes with increasing H_2 dilution. The growth rate drops by a factor of three between H_2 dilution ratios of 0 and 8, almost parallel to VHF deposition. More H_2 in the plasma reduces the growth rate further, but with a smaller slope and similar to RF deposition. We observe the onset of microcrystalline growth at 190°C for H_2 dilution ratios of ~30. It is therefore confirmed, that with H_2 dilution also, VHF plasma excitation yields the overall highest growth rates. DC plasma excitation results in astonishingly high growth rates for moderate H_2 dilution which are, in fact, not much smaller than those obtained for VHF. RF deposition yields, in the range of low dilutions, by far the lowest growth rates; for higher dilution ratios and towards the transition to microcrystalline growth, growth rates are comparable for DC and RF excitation. Microcrystalline growth starts at the lowest H_2 dilution ratios for VHF excitation. DC and RF deposition both require much higher H_2 dilution ratios to yield microcrystals.

For all three plasma excitation frequencies, the substrate temperature has a relatively small influence on the growth rate. The growth rate increases slightly with increasing substrate temperature and at any temperature follows the same dependence on the H_2 dilution ratio as plotted in Figure 28. As an example, we show in Figure 29 the growth rate of the VHF-deposited a-Si:H layers as a function of the substrate temperature for a larger set of samples at slightly higher power density. For all H_2 dilution ratios, the growth rate increases very slightly with increasing substrate temperature.

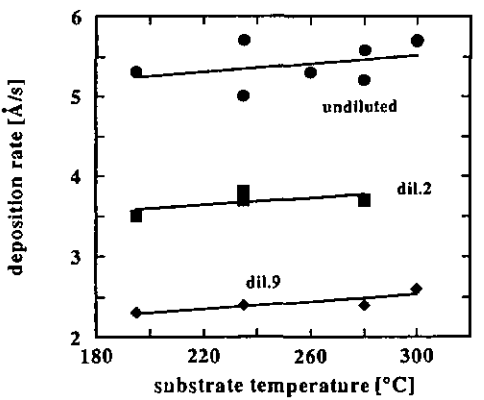

Figure 29: Deposition rates for three H_2 dilution ratios as a function of the substrate temperature. Input power is 45 mW/cm² for all samples.

There is very few data published about deposition rates; our values, however, agree with the general fact that is reported in the literature, that RF deposition without dilution yields deposition rates of the order of 1-2 Å/s [87-90]. Deposition rates for diluted i-layers may reach 2 Å/s [81] for a highly optimized process, in most cases, however, values around [91] or below [92,93] 1 Å/s are reported, depending on the dilution ratio of the i-layer. Microwave glow discharge yields deposition rates of up to 100 Å/s for a-SiGe:H alloys deposited with H_2 dilution [94,95]; however, even at a reduced deposition rate of 10 Å/s, the degradation of solar cells incorporating such high-rate deposited layers is still larger than the degradation of cells containing i-layers deposited by RF at ~1 Å/s [96].

II.2.3.4. Stability

We have seen that VHF deposition yields considerably higher growth rates compared to RF deposition and, depending on the H_2 dilution ratio, also compared to DC plasma excitation. The enhanced growth rate is even more important in the case of H_2 dilution as the growth rates decrease for all three techniques strongly with increasing dilution. No satisfactory answer has been given so far as to if and how this enhanced growth rate affects

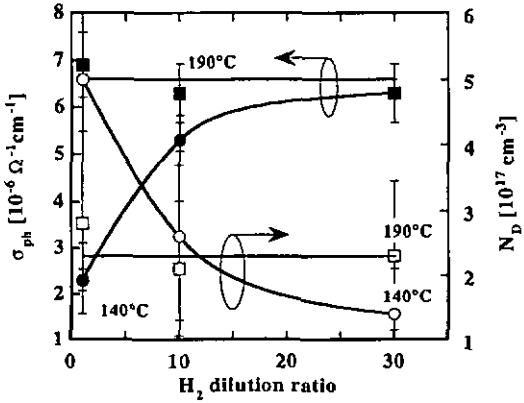

Figure 30: Defect density from CPM measurements and photo-conductivity values in the degraded state for RF-deposited films as a function of the H_2 dilution ratio. Circles: T_s = 140°C, squares: T_s = 190°C, open symbols: defect density (CPM), black symbols: photo-conductivity. Error bars indicate an estimated experimental error of ±50 % for the defect density and ±10 % for the photo-conductivity.

the stability of the VHF-deposited films. The main goal of H_2 dilution is to enhance the stability of the films against light soaking. H_2 dilution improves the stability for VHF-deposited samples, as has been shown above (Figure 25 on page 42). Similar results are reported in the literature, both for RF and DC excitation. Yet, a direct comparison requires identical experimental conditions such as degradation and measurement procedures. In the following we directly compare all three techniques. Both, VHF and DC layers have been deposited especially for this purpose, degradation and measurement of the $\mu_0\tau_0$ product was performed in the same manner. Unfortunately we only have values for the photo-conductivity and the defect density in the degraded state for the RF-deposited samples [18,97].

Figure 25 (page 42) shows the $\mu_0\tau_0$ product in the degraded state as a function of the H_2 dilution ratio. Data are for VHF-deposited samples and deposition temperatures between 195°C and 280°C. The $\mu_0\tau_0$ product for samples deposited without H_2 dilution improves slightly with increasing substrate temperature, and considerably with H_2 dilution. A H_2 dilution ratio of two raises $\mu_0\tau_0$ by a factor of two. A further increase in the H_2 dilution ratio does not raise $\mu_0\tau_0$, whereas the optical gap continues to increase.

In RF-deposited films (Figure 30), higher deposition temperature similarly results in higher photo-conductivity and lower defect density in the degraded state for films deposited without H_2 dilution. H_2 dilution raises σ_{ph} and reduces the defect density for the samples deposited at the lower substrate temperature, both by up to a factor of 2-3. The material quality continuously increases with increasing H_2 dilution, even though most of the

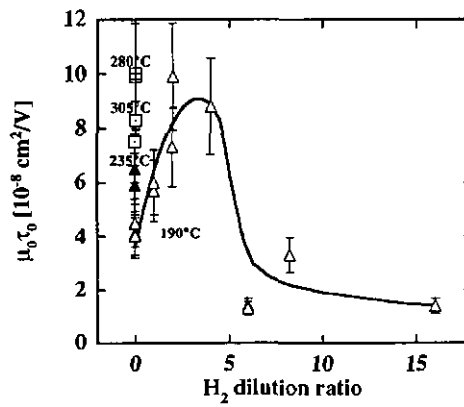

Figure 31: $\mu_0\tau_0$ product in the degraded state for DC-deposited films as a function of the H_2 dilution ratio. T_s ~ 200°C. Error bars indicate an estimated experimental error of ±20 %.

improvement is achieved already for a H_2 dilution ratio of ten. H_2 dilution has a much smaller effect for the higher substrate temperature, if it exists at all. Note that part of the increase in σ_{ph} upon H_2 dilution may be due to a shift of the Fermi level due to oxygen incorporation.

Likewise, the $\mu_0\tau_0$ product in the DC films improves with increasing substrate temperature for undiluted films (Figure 31). H_2 dilution has a beneficial effect at low dilution ratios: the degraded $\mu_0\tau_0$ product is roughly a factor of two higher for samples deposited with a dilution ratio of two to four than for undiluted films, which is comparable to the improvement achieved for VHF-deposited samples (Figure 25). Also, the $\mu_0\tau_0$ product for the best DC-deposited films (~$1.0 \cdot 10^{-7}$ cm^2/V) is comparable to the highest value for VHF-deposited samples (~$1.2 \cdot 10^{-7}$ cm^2/V). For high dilution ratios, in contrast to the observations for VHF and RF deposition, the electronic quality of the films decreases again, even to a value lower than the one for undiluted films.

Deposition at enhanced substrate temperature results in significant improvement of the electronic transport properties in the degraded state (Figure 32). For all three deposition techniques, DC, RF, and VHF, we observe a decrease in the H content in the films with increasing deposition temperature (Figure 26). This observation is in agreement with the results obtained for the hot wire (HW) deposition technique [98,99]. The enhanced stability

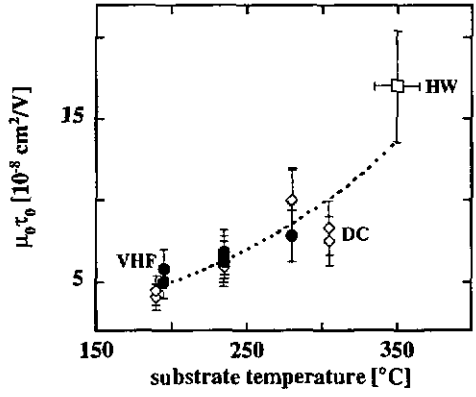

Figure 32: $\mu_0\tau_0$ product in the degraded state for DC- and VHF-deposited films as a function of the deposition temperature. All samples are deposited from undiluted SiH_4 plasma. For comparison we added the best value reported by Ziegler [70] for a HW-deposited sample without H_2 dilution. Error bars indicate an estimated experimental error of ±20 %.

of HW-deposited films also is connected to a low hydrogen content, yet at even lower values of ~2 % [100-104]. These observations raise the question to which extent the enhanced stability of HW-deposited films is produced by the high deposition temperature alone (see Figure 32), and to which extent by the observed structure of hot wire deposited films [105]. This question, even though of fundamental interest, must remain unanswered at this point and may provide an interesting challenge for future work.

Deposition using the hydrogen dilution method also enhances the stability. However, for films deposited with H_2 dilution and using RF or VHF deposition, the enhanced stability correlates with increased H content. DC-deposited samples also exhibit improved stability when deposited with H_2 dilution, but in their case the more stable films contain

	increased T_s - hydrogen content	H_2 dilution - hydrogen content
DC	Reduced	~ Constant
RF	Reduced	Increased
VHF	Reduced	Increased
HW	Reduced [e.g., 98,99]	

Table 3: Overview on the influence of different means to enhance the stability on the hydrogen content in the film for the different deposition techniques. 'Reduced' and 'increased' refers to a-Si:H deposited at standard temperature (~200°C) without H_2 dilution.

approximately as much hydrogen as standard undiluted films. Table 3 illustrates this paradox.

Peculiarity of DC plasma excitation

We have seen that DC excitation exhibits different behavior with respect to hydrogen dilution compared to VHF and RF. We observe an optimum H_2 dilution ratio, above which the transport properties of the material in the light-soaked state decrease. Optimum light-soaked properties are obtained for the H_2 dilution ratio that corresponds to the lowest microstructure factor. The growth rate as a function of the H_2 dilution ratio is not a smooth function as in the case of VHF or RF deposition, we observe two distinctly different slopes, the transition between both regimes lying again close to the point of the most stable films. At the same time the electronic properties of the best DC-deposited films are comparable to those for the best VHF-deposited samples.

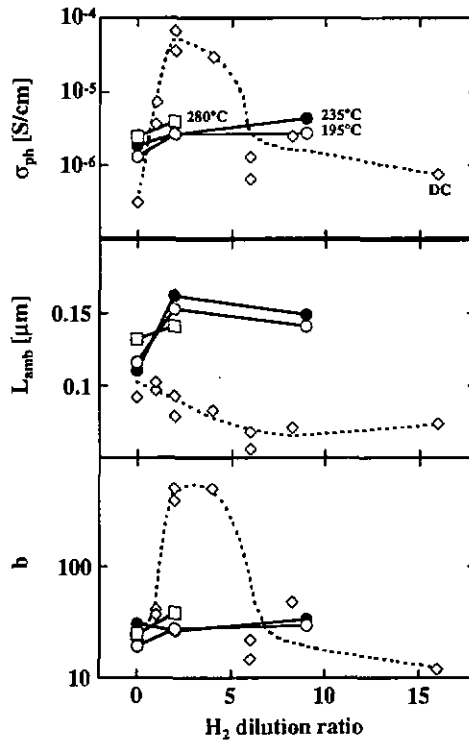

Figure 33: Photo-conductivity, ambipolar diffusion length and b-factor in the light-soaked state as a function of the H_2 dilution ratio. Shown are samples deposited using DC excitation and VHF at different substrate temperatures.

Figure 33 shows photo-conductivity, ambipolar diffusion length and the b-factor (Figure 6) for the series of DC- and VHF-deposited samples in the degraded state. As stated in section I.3.2.2, the b-factor is given by the ratio of the products $\mu_n n/\mu_p p$ for majority and minority carriers. For intrinsic samples in the degraded state, this ratio is usually close to 50, as is the case for the VHF-deposited samples. The best DC-deposited samples, however, made at a dilution ratio of two to four, are characterized by b-values which are roughly an order of magnitude higher than this expected value, indicating that the Fermi level is slightly shifted towards the conduction band edge. The reason herefore is not known; it can, however, be speculated that n-type doping by oxygen might be a possible explanation. Another reason could be a different energetical position of the defects in the band gap. It is noteworthy that HW-deposited samples with high $\mu_0\tau_0$ product in the light-soaked state also exhibit values of

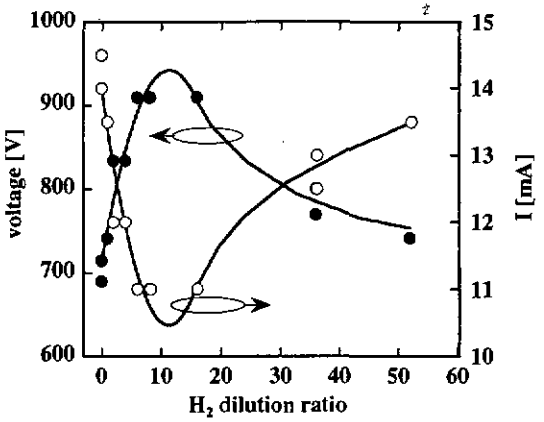

Figure 34: Electrode voltage and discharge current for DC plasma and varying H_2 dilution ratio. The plasma power was held constant at 10 W.

b which are much higher than what is usually observed for "standard" glow-discharge material [106]. Let us state furthermore, that such high values of b once more emphasize the need for a material quality parameter that takes into account both, majority and minority carriers. The photo-conductivity for the DC-deposited samples in Figure 33 made with H_2 dilution ratios of two and four is over-estimated because the Fermi level is obviously shifted as can be seen from the b-factor. At the same time the ambipolar diffusion length is under-estimated, for the same reasons. Measurement of each of both parameters alone would therefore yield a wrong judgement of the material quality.

DC plasma excitation offers the possibility to easily measure voltage and current of the discharge. For the series of samples described in this work, the power was held constant in order to obtain conditions comparable to VHF and RF. Figure 34 shows electrode voltage and discharge current as a function of the H_2 dilution ratio. One observes (Figure 34) that for small dilutions the discharge current decreases strongly with H_2 dilution, similar to the curve observed for the growth rate (Figure 28). In fact it makes sense to assume the growth rate proportional to the (ion) current. For even higher dilution ratios, the current increases again, this time, however, without an increase in growth rate. Thus, we speculate that the current in this case may be mainly carried by species (H) which do not contribute to the film growth. The voltage obviously follows an inverse tendency, corresponding to constant power. This means, in turn, that the most stable films have been deposited under conditions where the discharge voltage was increased compared to the undiluted case. The electrode voltage observed for DC deposition is very high compared to deposition using a high-frequency

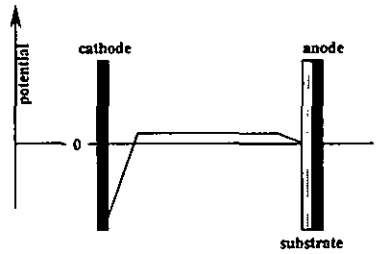

Figure 35: Sketch of the voltage distribution in a DC glow discharge process, according to ref. 107.

deposition technique. In fact, the electrode voltage for DC excitation is, already for undiluted plasma (~700 V), more than an order of magnitude higher than what is observed for VHF deposition at 70 MHz (~50 V) [79]. The voltage distribution in a DC discharge is, however, not uniform. The bulk of the plasma is almost field-free and slightly positive with respect to the anode (which is in our case grounded); a large voltage drop is found next to the cathode (see Figure 35) [107]. Therefore positive ions contributing to the films growth acquire only moderate energies in the small voltage drop in front of the anode.

II.2.4. Discussion and conclusions

H_2 dilution has been shown to enhance the electronic transport properties of a-Si:H in the light-soaked state for all the investigated excitation methods. For the DC deposition technique we observe an optimum H_2 dilution ratio whereas VHF and RF exhibit a pronounced improvement for small H_2 dilutions followed by a rather small additional effect for still higher H_2 dilution ratios. The reduced growth rate when employing H_2 dilution is certainly an important issue in industrial production. For VHF deposition at 70 MHz, we observe the best stabilized electronic properties for a H_2 dilution ratio of two, at a growth rate of ~4 Å/s. DC deposition yields comparable values for the $\mu_0\tau_0$ product in the degraded state for a H_2 dilution ratio of four and a slightly lower growth rate of ~3 Å/s. RF deposition yields considerably lower growth rates (~1 Å/s at a H_2 dilution ratio of ten and ~0.5 Å/s at a dilution of 30). We unfortunately cannot make a statement concerning the quality of the RF-deposited material described above that is based on an objective comparison under identical experimental conditions. There is, however, evidence, such as similar stabilized efficiencies for solar cells [108], indicating that the RF-deposited material described above is of quite similar quality in the degraded state as our VHF-deposited a-Si:H. Hence, as intrinsic a-Si:H material of more or less equal quality can be obtained by all three deposition techniques, the growth rate may become the decisive factor for the choice of excitation frequency. In fact, increasing the growth rate for RF deposition by increasing the deposition power or pressure is

found to be harmful to the stability of the solar cells [23,87,88,109,110]. VHF and DC technology are therefore, in terms of growth rate and material quality, found to be almost equivalent for the deposition of a-Si:H. VHF deposition at 70 MHz yields slightly higher growth rates compared to DC, yet the gain is small, given an additional small uncertainty for the effective plasma power. DC excitation, on the other hand, has the big advantage to allow for much simpler design of the deposition apparatus. Especially the problem to feed power in the high megahertz range into the deposition chamber, including matching network, generator and design of the reactor itself, is not trivial and is avoided when using DC excitation. It is therefore for us not surprising that Solarex, one of the major a-Si:H solar cell manufacturers, uses DC plasma excitation in production.

For application as intrinsic layer in a-Si:H solar cells, other issues besides the electronic transport properties of the material in the degraded state have to be taken into account. All three excitation techniques result in a more or less pronounced increase in the optical gap of a-Si:H deposited with H_2 dilution. This in turn requires thicker i-layers to obtain a given current density, thus affecting the stability of the solar cell. However, this effect is an advantage for the thin a-Si:H top cells in tandem or triple junctions. For these wide-gap cells the necessary thickness adjustment is generally small, resulting in an overall efficiency gain from the enhanced stability coupled with the higher V_{oc} that results from the higher optical gap of the i-layer. Such questions, concerning the design of a-Si:H solar cells for optimum stabilized efficiency are discussed in the following two chapters, chapter III deals with the optimization of single-junction solar cells and chapter IV describes the incorporation of such optimized single-junction cells in tandem structures.

III. Single-junction solar cells

III.1. Introduction

Single-junction solar cells are of interest for several reasons: First, intrinsic material is, after a first assessment of its quality by means of material characterization, best studied when incorporated into a solar cell. Even though quite useful tools for the characterization of intrinsic materials with respect to their performance in a solar cell have been developed [14], the final judgement about a material can only be made once it has been incorporated into a solar cell and a complete evaluation of its performance in the cell, including AM 1.5 degradation, has been executed.

Second, single-junction solar cells can be an interesting approach for industrial solar cell production [111-114] and an attractive alternative to more expensive and complex tandem and triple structures. The manufacturing process is more robust, at the expense of a somewhat lower efficiency. Let us mention in this context only the very critical current matching issue in a tandem or triple cell structure. As will be shown in section IV.2.2, the stabilized efficiency of a tandem cell depends very critically on the current mismatch between top and bottom cell. The situation is certainly even more critical for a triple junction cell. In consequence, e.g. slight thickness inhomogeneities will result in efficiency losses due to location-dependent current mismatching. Single-junction solar cells, in contrast, behave very benignly with respect to the i-layer thickness as will be shown below.

The third interest in studying single-junction cells is the development of component cells for tandem or triple stacked structures. It is technologically more convenient to develop such component cells first in a single-junction structure before incorporating them into tandem cells. Such an approach is used in chapter IV.3 of this work in order to experimentally determine the best suited top cell for a micromorph tandem cell. In a similar way, the component cells of the a-Si:H/a-Si:H stacked cell were first optimized as single-junction cells.

The final goal of any optimization of solar cells is to increase their stabilized efficiency. Different aspects have to be addressed in this context. The cell performance is, under the condition that good doped layers are available, mainly determined by the properties and quality of the intrinsic material. E.g. the voltage of a solar cell is influenced by the optical gap of its i-layer. Yet a large optical gap resulting in high V_{oc} values reduces the current generation in the solar cell. The stability of the i-material against light soaking will determine to what extent the solar cell characteristics degrade upon illumination. A great variety of intrinsic a-Si:H based materials has been investigated within this work, following the demand

for solar cells with specific characteristics. Depending on the application, either a high voltage or rather a high current level may be desirable. The influence of different intrinsic materials on the solar cell characteristics in the initial and light-soaked state is discussed in sections III.2 (a-SiC:H solar cells) and III.3 (a-Si:H solar cells) of this chapter.

Beyond the material quality, other issues influence the solar cell performance before and after light soaking. Among those "design and technological" issues we address in section III.4 in particular interface layers and the problem of i-layer contamination.

III.2. a-SiC:H single-junction solar cells

The basic motivation of carbon alloying for enhancing the optical gap is to collect charge carriers generated by high-energy photons (blue and green) at a higher energy level, i.e. at a higher voltage (see section I.1.1).

Single-junction solar cells incorporating a-SiC:H i-layers have been deposited employing the VHF-deposited intrinsic materials which had been found to be promising in the material study (section II.1.2). As a "starting point" we used the material made from 40 % CH_4. Throughout the study, degradation was systematically investigated, keeping in mind that silicon carbon alloys are even more sensitive to degradation than a-Si:H and that hence cell optimization has to concern above all the degraded state performance.

The first series of solar cells (Table 4) consists of four cells with an i-layer thickness of 200 nm. Cells made from pure silane with a H_2 dilution ratio of ten and without dilution are compared to cells made with 40 % CH_4 and H_2 dilution ratios of ten and zero, respectively. The doped layers are the same for all cells.

type	E_{04} [eV]	initial		280h		relative degr. [%]	
		V_{oc} [V]	FF [%]	V_{oc} [V]	FF [%]	V_{oc}	FF
a-SiC:H undiluted	2.05	0.92	62.7	0.82	31.8	11	49
a-SiC:H (dil.10)	2.03	0.95	56.0	0.87	41.7	8	25
a-Si:H undiluted	1.90	0.82	66.4	0.82	59.0	0	11
a-Si:H (dil.10)	1.95	0.89	62.5	0.88	54.5	1	13

Table 4: V_{oc} and FF values for 200 nm thick p-i-n cells in the initial state and after 280 h light soaking. Listed are cells incorporating a-SiC:H and a-Si:H as the i-layer material, both with and without H_2 dilution.

The light soaking experiments for this series were performed at 50°C employing a sodium lamp with an intensity corresponding to 100 mW/cm². The H_2 diluted a-SiC:H cell has a higher V_{oc} in the initial state than the same cell deposited without H_2 dilution, even though the optical bandgap of the i-layer is sligbtly lower. The reason is the better electronic quality of material deposited with H_2 dilution resulting in less recombination within the i-layer and therefore a higher V_{oc}. The fill factor in the initial state is lower for the H_2 diluted cell, which is also the case for the a-Si:H reference cells. This is believed to be due to oxygen contamination of the i-layer when depositing with H_2 dilution as will be discussed in the context of a-Si:H i-layers in section III.4.3.1. However, FF degradation is remarkably reduced due to the H_2 dilution of the i-layer. Yet, compared to the a-Si:H solar cells, the FF

degradation of the H_2 diluted a-SiC:H solar cell is still twice as high. Both a-SiC:H solar cells show a strong V_{oc} degradation of ~0.1 V. It is interesting to note that the cell deposited from H_2 diluted SiH_4 has a higher V_{oc} value than the cell deposited from undiluted SiH_4 and suffers no degradation of the V_{oc}. This observation will be an important issue in section III.3.1.1 where it will be discussed in more detail.

An i-layer thickness of 200 nm for the a-SiC:H cell is obviously too thick to obtain sufficient stability of the solar cell, even in the case of the i-layer deposited with H_2 dilution. We therefore deposited the same a-SiC:H solar cell containing an i-layer deposited with H_2 dilution but with an i-layer thickness which is reduced to 100 nm (Table 5).

type	E_{04} [eV]	initial		280h		Relative degr. [%]	
		V_{oc} [V]	FF [%]	V_{oc} [V]	FF [%]	V_{oc}	FF
a-SiC:H (dil.10)	2.03	0.95	68.7	0.90	54.1	5	21

Table 5: V_{oc} and FF values for a 100 nm thick a-SiC:H p-i-n solar cells in the initial state and after 280 h light soaking.

Degradation is considerably reduced if the i-layer thickness is reduced to 100 nm. Furthermore, the FF is already in the initial state considerably higher for the thinner solar cell. The explanation is to be sought in the internal electric field. The a-SiC:H i-layer has a relatively high defect density causing enhanced recombination within the i-layer. A thinner i-layer results in a higher built-in electric field in the cell, therefore drift-assisted carrier extraction is enhanced and in consequence the fill factor improved. The same is true after degradation. In addition, the amount of defect generating recombination events (which are the cause for the degradation effect) is reduced in a thinner cell with a higher electric field resulting in less recombination.

As a-SiC:H cells are to be applied as top cells in tandem or triple structures, a realistic thickness will indeed be rather like 100 nm or even less. Furthermore, degradation will be less pronounced as light which is not absorbed in the top cell will not be reflected as in the case for these test cells which were made with a highly reflective ITO/Ag back contact.

However, the stability of the 100 nm thick a-SiC:H solar cell is still not very satisfying. Enhancing the H_2 dilution ratio for the i-layer beyond a ratio of ten can ameliorate the stability of the solar cell (Table 6). The relative degradation of V_{oc} and FF is reduced by 50 % when increasing the H_2 dilution ratio from ten to 30. Yet, we again observe a decrease of the fill factor in the initial state with increasing H_2 dilution ratio, probably due to oxygen contamination. Still, we observe a gain in both, the stabilized V_{oc} and FF, with increasing H_2 dilution ratio.

	V_{oc} [V]			FF [%]		
	initial	degraded	relative	initial	degraded	Relative
dil.10	0.97	0.90	8 %	67	48	40 %
dil.20	0.96	0.91	5 %	65	50	30 %
dil.30	0.97	0.93	4 %	62	51	22 %

Table 6: Initial and degraded values for V_{oc} and FF of solar cells where the i-layer had been deposited employing varying H_2 dilution ratios. i-layer thickness is 100 nm. The cell made at H_2 dilution of ten is equivalent to the cell of Table 5.

In conclusion to the study of a-SiC:H alloys as absorber layer in p-i-n solar cells one can state that H_2 dilution considerably improves the stability of VHF-deposited a-SiC:H solar cells. V_{oc} values in the initial state as high as 0.97 V for a-SiC:H single-junction cells could be achieved. Tandem cells (section IV.1) incorporating a-SiC:H top cells yielded V_{oc} values of 1.82 V (a-SiC:H/a-Si:H tandem cell) and 2.68 V (a-SiC:H/a-Si:H/a-Si:H triple junction cell).

A very important improvement due to this study was the optimization of the a-SiC:H p/i-buffer layer (section III.4.2.1) which led to an actual enhancement of the stabilized efficiency of p/b-i-n solar cells. a-SiC:H alloys are of continuing interest for such p/i-buffer layers and p-layers of p-i-n type solar cells as well as for some specialized applications such as semi-transparent solar cells [54,55] where the stability issue is of secondary importance.

However, already at the time when the above experiments were performed, the interest in a-SiC:H alloys for the application as active layer in a solar cell was globally strongly decreasing due to the unsatisfactorily resolved stability problem. High-voltage a-SiC:H solar cells have been demonstrated [115], however those cells are not applied in today's best stable a-Si:H stacked cell modules [116] because of their insufficient stability. In our case also, the finding of the possibility to achieve the same V_{oc} values as for a-SiC:H solar cells but with far better stability when using a-Si:H deposited at low substrate temperature and with H_2 dilution (section III.3.1) resulted in a shift of the interest towards those low-temperature a-Si:H materials.

III.3. a-Si:H single-junction solar cells

Section II.2 has presented an extended catalogue of intrinsic a-Si:H materials. The present section describes the incorporation of these materials in p-i-n solar cells. The "standard" a-Si:H i-layer material (no H_2 dilution, 235°C) is directly compared to the newly developed materials which are deposited at various substrate temperatures and hydrogen dilution ratios (section III.3.1). For substrate temperatures exceeding the standard temperature, special precautions have to be taken in order to obtain good-quality solar cells. Such cells are described in section III.3.2.

III.3.1. i-layer deposition with H_2 dilution

It has been shown in section II.2 that the H_2 dilution technique leads to intrinsic a-Si:H layers with considerably improved stability against light-induced degradation. We have reported an improvement of the $\mu_0\tau_0$ parameter in the light-soaked state by a factor of two. At the same time, H_2 dilution results in enhanced values for the optical gap of the resulting a-Si:H layers. The following section describes the insertion of these H_2 diluted i-layers in p-i-n solar cells and the effect on the cell characteristics in the initial and light-soaked state.

III.3.1.1. Solar cell results

In order to study the influence of H_2 dilution and deposition temperature of the i-layer on the solar cell performance, we deposited two series of cells. The first series was deposited at standard deposition temperature of 235°C, the second at a substrate temperature of 195°C. The H_2 dilution ratio for the i-layer deposition was varied between zero and nine.

The doped layers were deposited at the same temperature as the i-layer; the other doped layer parameters were held constant. The material properties of these i-layer materials have been described in section II.2.2. The i-layer thickness was chosen to be 450 nm, i.e. much thicker than for stability-optimized solar cells, in order to be as sensitive as possible to variations of the i-layer quality. The cells were systematically degraded for 1000 h at 50°C under white light (spectrum close to AM 1.5, 100 mW/cm^2) and open circuit conditions.

The increase in the optical gap due to H_2 dilution for constant deposition temperature has been reported in section II.2.2.1. This increase has consequences for the solar cell performance, namely V_{oc} and I_{sc} vary with the dilution ratio. In the experiment (Figure 36), this increase in the optical gap results in a strong decrease of the short circuit current density. At the same time the enhanced optical gap of the i-layer results in a pronounced increase in the V_{oc} values for these cells. The fill factor in the initial state is a priori not influenced.

H_2 dilution enhances the stability of the solar cells due to enhanced stability of the i-layer; the consequences of H_2 dilution on the solar cell parameters in the light-soaked state

are as follows. For the 195°C samples, the V_{oc} decreases slightly during degradation (except the sample deposited at a H_2 dilution ratio of nine, where the V_{oc} increases) whereas the V_{oc} values for the 235°C samples even slightly increase with degradation for all H_2 dilution ratios. An increase of the V_{oc} value during degradation is quite surprising. Similar observations have been reported by the group at the Forschungszentrum Jülich [92,117]. The FF after degradation for the cells deposited at a substrate temperature of 195°C increases with H_2 dilution. For the 235°C cells, the degraded fill factor is only slightly improved by H_2 dilution. In both cases, the improvement takes place already for moderate H_2 dilution ratios of two (Figure 36), confirming thereby the observation made by studying the material degradation alone that a H_2 dilution ratio of two is sufficient to obtain a considerable gain in stability.

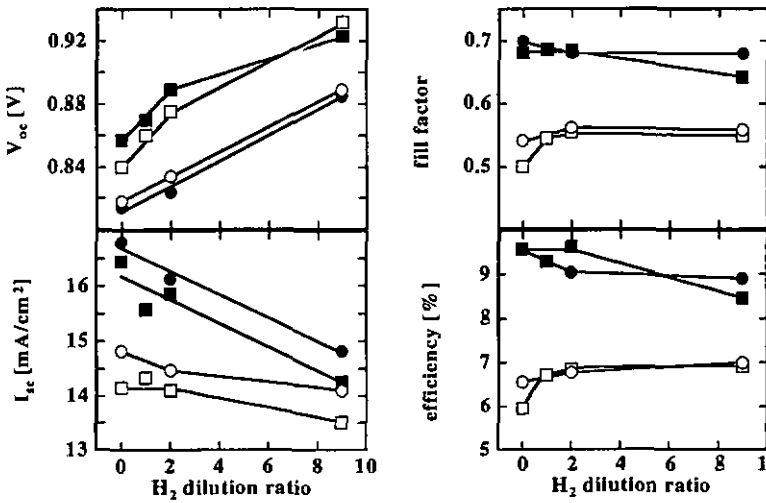

Figure 36: V_{oc}, I_{sc}, FF and efficiency values for p-i-n cells deposited at 235° (■) and 195°C (■) as a function of the H_2 dilution ratio before and after 1000 h degradation. i-layer thickness is 450 nm. Filled symbols indicate the as-deposited, open symbols the light-soaked state.

In the initial state, we observe a drastic decrease of the short circuit current density with H_2 dilution for both temperatures. H_2 dilution, however, reduces this I_{sc} degradation strongly so that, after degradation, the difference between undiluted and strongly H_2 diluted cells is reduced to less than 1 mA/cm^2 (Figure 36). Yet, this phenomenon is influenced to a certain extent by the fact that the i-layer of the solar cells is relatively thick (450 nm). For thinner cells, the enhanced stability of the material would be expected to have more effect on the fill

factor than on the current. In thinner solar cells, the effect of the material quality on the collection efficiency becomes noticeable only at forward voltages when the internal electric field no longer is capable to "mask" to a certain extent the quality of the material. The voltage where a considerable current loss occurs depends on the quality of the material.

The observed gain in V_{oc} and the stabilized fill factor have to compete with the observed loss in current density due to the higher optical gap of the H_2 diluted i-layers. However, the strong V_{oc} increase and the higher FF value after degradation over-compensate this loss in current density. The stabilized efficiency therefore increases with H_2 dilution for both temperatures, the main effect, however, appears at reduced temperature. The increase is pronounced between H_2 dilution ratios zero and two, higher dilution does not improve the stabilized efficiency further. This confirms the observation made in the materials section of this work. Both series have the same efficiency in the degraded state for dilution ratios of two and higher, one cell having a higher current and smaller voltage, the other cell the inverse. This possibility of a choice between current and voltage is particularly interesting in the context of tandem and stacked cells.

III.3.1.2. Correlation between material characteristics and solar cell performance

Our material study (section 0) has shown that H_2 dilution enhances the stability of a-Si:H against light soaking. Above, we have seen that the stabilized efficiency of p-i-n solar cells incorporating such H_2 diluted material is increased. In order to quantify this qualitative observation and in order to establish a larger context, we plot in Figure 37 the efficiency and the fill factor of 450 nm thick p-i-n cells in the initial as well as in the degraded state as a function of the $\mu_0\tau_0$ product of their i-layer material. The intrinsic layers of the solar cells in Figure 37 correspond to those shown in Figure 25, the solar cells to those of Figure 36.

We observe a good linear correlation between the efficiency and $\log(\mu_0\tau_0)$. The correlation is valid for all H_2 dilution ratios and both temperatures which confirms the significance of the $\mu_0\tau_0$ parameter also in the case of H_2 diluted i-layers. However, as the $\mu_0\tau_0$ parameter is a measure for the electronic transport properties of the intrinsic layer, a correlation is expected a priori only between the FF of the solar cell and the $\mu_0\tau_0$ parameter. Especially H_2 dilution has an influence not only on the stability of the i-layer but also on its optical gap, influencing thereby V_{oc} and I_{sc}. In fact, we observe such a linear correlation between the fill factor and $\log(\mu_0\tau_0)$. For the case of our series of H_2 diluted cells we observe an approximately constant product of V_{oc} and I_{sc} of ~13-14 mW/cm^2 in the initial state, which is independent of the H_2 dilution ratio and deposition temperature. In the degraded state this product is also almost a constant with a value of ~12 mW/cm^2. This means that the increase in V_{oc} is compensated by the decrease in I_{sc}, annihilating thereby the effect on the efficiency. Therefore, the correlation for the efficiency is valid only because the influence of the optical

gap on the efficiency can be neglected. Let us note also that the variation of the material quality in the work by Beck et al. was obtained by varying the deposition temperature of the intrinsic layer which has a considerable effect on the optical gap of the material and therefore on voltage and current. Here also, it is rather surprising that the correlation between $\mu_0\tau_0$ and the efficiency is observed in spite of variations in V_{oc} and I_{sc}. Furthermore, because of the important thickness of the intrinsic layers one would have to plot the FF times a factor describing the collection losses at 0 V (e.g. $I_{sc}/I(-3\ V)\cdot FF$) in order to account for recombination losses at I_{sc} conditions. Especially in the light-soaked state the internal electric field at 0 V may not be sufficient to extract all light-generated carriers.

Despite those critical remarks, however, our experiments confirm a correlation between $\mu_0\tau_0$ and the solar cell performance. For the reasons given above, $\mu_0\tau_0$ should not be used to predict a solar cell efficiency, but rather to compare the electronic quality of different materials.

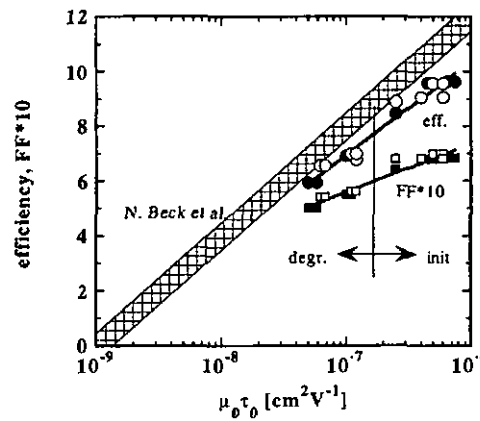

Figure 37: Correlation between the material parameter $\mu_0\tau_0$ and solar cell characteristics. The solar cells contain i-layers with varying H_2 dilution ratio. Plotted are efficiency and FF of the solar cells as a function of the $\mu_0\tau_0$ product of their i-layers in the initial and light-soaked state. i-layer thickness of the solar cells is 450 nm. Open symbols are for i-layers deposited at 235°C, black symbols for those deposited at 195°C. The curve given by Beck et al. [14] for 600 nm thick solar cells is given for comparison.

III.3.2. p-i-n cells at enhanced substrate temperature

Enhanced stability of p-i-n solar cells can be achieved by several means. The incorporation of more stable intrinsic material by means of H_2 dilution has been described in the previous section. Reducing the i-layer thickness also has a beneficial effect on the stability. In order to generate the same current density within a thinner i-layer, one needs a reduced optical gap of the i-layer in order to enhance the absorption. It has been shown in section II.2.2.3 that deposition at enhanced substrate temperature (in the following called high-T_s) results in a-Si:H with reduced optical gap. Furthermore, this material exhibits enhanced stability compared to material deposited at standard temperature (Figure 32, page 52). Such a-Si:H deposited at higher substrate temperature therefore combines two advantageous properties, a high optical absorption and good stability which is of interest for several applications. In single-junction solar cells, such intrinsic material could potentially lead to enhanced stabilized efficiency. When employed in a bottom cell of an a-Si:H/a-Si:H tandem cell, a p-i-n cell deposited at enhanced temperature raises the totally available current and increases thereby the efficiency potential. Finally, a thin and strongly absorbing p-i-n solar cell is an interesting candidate for the top cell in a micromorph tandem (section IV.3).

Solar cells have been made employing i-layers deposited without H_2 dilution. Slight H_2 dilution would be interesting from the stability point of view. However, we restricted our study to i-layers without H_2 dilution. The optical absorption decreases strongly with dilution

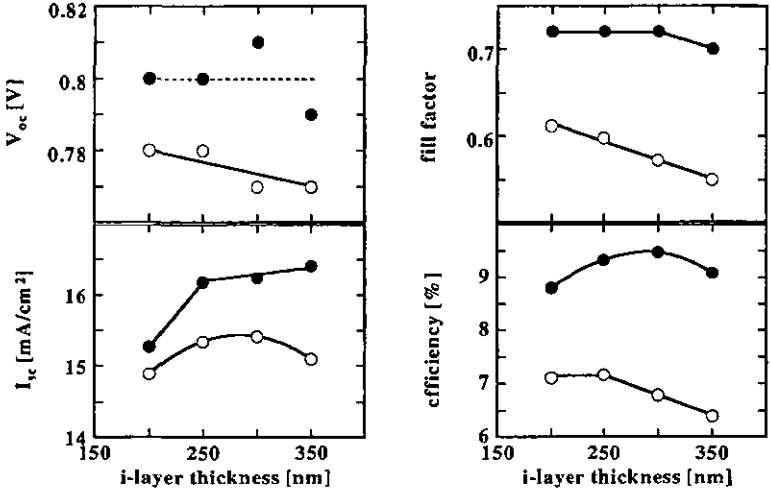

Figure 38: Performance data of optimized high-T_s p/b-i-n solar cells in the initial (●) and degraded (○) state. Substrate temperature for i-layer deposition is 280°C.

(section II.2.2.1) which counteracts the goal of strongly absorbing cells with a high current generation. The doped layers were deposited at the standard substrate temperature (235°C). Before the deposition of the i-layer, the grounded electrode with the substrate was heated up to the deposition temperature of the i-layer. A gas flux of 20 min. prior to the deposition assured a homogeneous temperature over the substrate. After the deposition of the i-layer, the substrate was cooled down before the deposition of the n-layer.

The deposition of the i-layer at higher than standard temperature results in technological problems connected to the fact that the very important p/i-interface is subject to the elevated temperature during the growth of the i-layer [89]. These problems and solutions found here will be discussed below (section III.4.2.2). At this point we present only the results for already optimized solar cells with intrinsic layers deposited at 280°C, i.e. ~50°C higher than the standard temperature at which the doped layers have been deposited (Figure 38). A direct comparison of these high-T_s solar cells to other types of solar cells presented in this work is shown in Figure 51 (page 87).

We obtain reasonably good solar cells, which provide a current density of almost 15.5 mA/cm^2 for an i-layer thickness of 250-300 nm in the degraded state, compared to barely 15 mA/cm^2 for a solar cell with an even thicker i-layer of 450 nm deposited at standard temperature without H_2 dilution (Figure 36). However, thicker i-layers deposited at the elevated temperature lead to a strong current degradation as well as a decrease of the degraded V_{oc} with thickness, which can be attributed to problems connected to the internal electric field.

III.4. Design and technological considerations

The choice of a suitable intrinsic material for a given solar cell application is only part of the way towards the best possible solution for a solar cell. Additional measures with respect to the solar cell design can be taken to enhance the solar cell performance. Namely interface or so-called buffer layers play an important role in this cell optimization process. Such buffer layers have been investigated in this work for two purposes, on the one hand to enhance the V_{oc} and on the other hand as a diffusion barrier in order to prevent boron contamination of the intrinsic layer.

The electric field in the solar cell is an issue which repeatedly had to be addressed, both in the context of interface layers and also of intrinsic layers where contaminations can act as donors and acceptors and thereby reduce the electric field. Part of these technological issues originates from the use of a single-chamber deposition system in this work.

III.4.1. Graded hydrogen dilution - "a-Si:H buffer"

Both, the study of H_2 dilution for the deposition of intrinsic material (section II.2.2) and the incorporation of such material into solar cells (section III.3.1.1), have shown that a moderate H_2 dilution ratio of two is sufficient to obtain the maximum gain in stability. The increase in the optical gap that is connected to H_2 dilution results in undesired current loss in solar cells. However, the V_{oc} of solar cells increases with increasing H_2 dilution ratio. We found that a relatively thin layer with the highest gap (=highest dilution ratio) at the p/i-interface is sufficient to achieve a considerable increase in V_{oc}.

We developed cells where a graded H_2 dilution ratio is employed for the deposition of the i-layer. The first part of the i-layer of about 20 nm close to the p/i-interface was deposited with a H_2 dilution ratio of nine. The bulk of the i-layer was deposited using a dilution ratio of only two. We could thereby combine good i-layer stability (dilution ratio two of the bulk), avoid a too strong increase of the optical gap and still obtain a high V_{oc}. Figure 39 shows the I-V-parameters of such cells in the initial and degraded state as a function of the i-layer thickness. After 1000 h light soaking, all cells show, independent of the cell thickness in the investigated range, a stabilized efficiency of ~7.5 %. The increase in current with increasing i-layer thickness is compensated by a more pronounced fill factor degradation.

The V_{oc} of such cells lies in between the value obtained for solar cells containing i-layers deposited entirely with a dilution ratio of nine (~0.93 V) and cells deposited with dilution two (~0.87V) (see Figure 36). This gain is obtained without increasing the optical gap of the bulk of the i-layer further, i.e. above the value corresponding to a H_2 dilution ratio of two. In fact, the current density of ~15.8 mA/cm^2 in the initial and ~14 mA/cm^2 in the degraded state obtained with a 450 nm thick cell deposited at 195°C with H_2 dilution ratio of two corresponds well to an extrapolation to 450 nm i-layer thickness in Figure 39. A possible drawback of this solar cell deposition technique is the reduced current generation compared to undiluted solar cells deposited at standard temperature. The importance of a high current

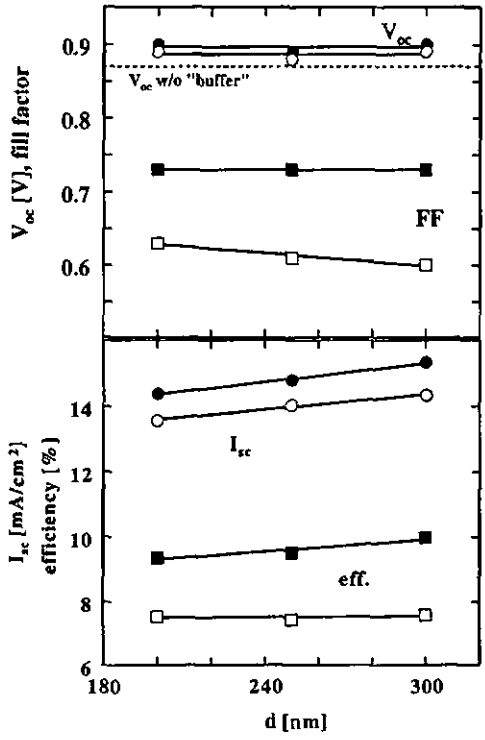

Figure 39: Top: Experimental values of V_{oc} and FF in the initial (black symbols) and degraded (1000 h, open symbols) state for single-junction cells with graded H_2 dilution i-layers as a function of the i-layer thickness. T_S = 195°C. Bottom: I_{sc} and efficiency in the initial and degraded (1000 h) state.

generation versus a high voltage and good stability of the solar cell may, in fact, depend on the specific application. The presented cell deposition technique with a graded H_2 dilution ratio is promising as well for single-junction cells as also for stacked or tandem solar cells. In fact, a stabilized efficiency of 7.5 % is the highest value obtained so far in our laboratory for a single-junction solar cell. Stacked and tandem solar cells employing such cells as top cells will be discussed in chapter IV.

III.4.2. a-SiC:H "buffer" layers

An approach which is quite similar to the one discussed in the previous section can be used to enhance the V_{oc} of a-Si:H solar cells which is relatively low considering the potential according to the optical gap [3]: the insertion of a thin layer of intrinsic material with increased optical gap (usually an a-SiC:H alloy, in the previous section a-Si:H with a widened optical gap) at the p/i-interface has been found to enhance the open circuit voltage of a p-i-n solar cell [45,46,118-120]. A band offset is generated between this so-called buffer layer and the i-layer due to the mismatch of the optical bandgap energies. The offset of the conduction band edge between the buffer layer and the bulk i-layer material results in a barrier for electrons at the conduction band edge. One of the limitations for the V_{oc}, the back-diffusion of electrons to the p-layer, is therefore reduced by the insertion of the buffer layer. The back-diffusion results in enhanced dark current I_0, which directly affects the V_{oc} of the cell [e.g., 3].

III.4.2.1. a-SiC:H buffer layer for V_{oc} enhancement

Silicon-carbon alloys have been discussed in section II.1 of this work. It has been shown that the main problem of these materials is their low stability against light soaking compared to unalloyed a-Si:H. Hydrogen dilution considerably improves the material quality, however, degradation remains one of the main problems for these materials.

When optimizing buffer layers, it is quite difficult to distinguish between degradation due to the buffer layer and degradation due to the bulk of the i-layer. To reduce the influence of i-layer degradation as much as possible we used cells with an i-layer of 100 nm thickness and deposited with a H_2 dilution of nine. The degradation of this i-layer itself is very small and can therefore be considered to be negligible compared to the degradation of the buffer layer. In Figure 40 the triangles indicate V_{oc} and FF values in the initial and degraded state for a p-i-n solar cell containing such a 100 nm thick i-layer. Adding an a-SiC:H buffer layer (60 % CH_4, 40 % SiH_4, H_2 dilution ratio of ten) at the p/i-interface increases the V_{oc} of the solar cell to values close to 1 V, but reduces the fill factor to below 50 %. Furthermore, after degradation the V_{oc} is lower than without buffer layer and the fill factor is reduced to ~25 %.

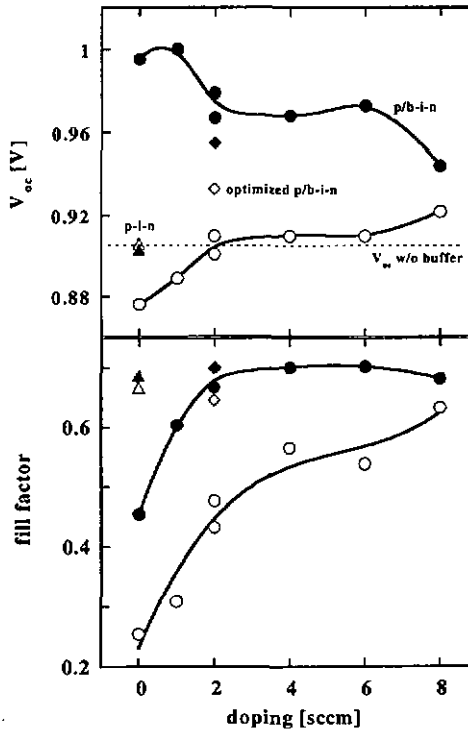

Figure 40: Top: V_{oc} for cells with a buffer layer (60 % CH_4, dilution 10) in the initial (filled) and the degraded (open symbols) state for different doping fluxes (B_2H_6 500 ppm in H_2) for the buffer and comparison to a cell without buffer layer (triangles). i-layer thickness is 100 nm. Diamonds indicate the best cell with an optimized buffer layer (40 % CH_4, dilution 20). Bottom: FF for the same cells before and after degradation.

It has already been proposed by Rech et al. [121] to insert a certain amount of boron into the buffer layer in order to compensate the large density of positively charged defects after degradation and thereby maintain the electric field in the bulk of the i-layer. We therefore prepared a series of solar cells where varying amounts of B_2H_6 were added during deposition of the buffer layer (circles in Figure 40). The undoped part of the i-layer was not modified. Doping of the buffer layer can increase the fill factor in the initial state and reduce its degradation. Similar results have been observed also for solar cells containing an a-SiC:H

intrinsic layer and additionally an a-SiC:H buffer layer [122]. For all cells in the series (Figure 40), however, independent of the doping level, there is no gain in V_{oc} relative to the cell without buffer after degradation, and the fill factor is always lower than for cells without a buffer layer.

In order to increase the stability of the buffer layer itself we further optimized the a-SiC:H material. Less CH_4 in the gas phase and a higher H_2 dilution ratio results in better material quality and enhanced stability (section II.1.2). Employing improved buffer layer material (40% CH_4 in the gas phase, increased H_2 dilution ratio for the buffer layer of 20 and appropriate doping with 100 ppm $B_2H_6 \equiv 2$ sccm B_2H_6/H_2), we obtained the following result: $V_{oc} = 0.95$ V with a fill factor of 70 %, which degrades after 1000 h to 0.93 V and a fill factor of 64.5 % (diamonds in Figure 40). In this case a net gain in V_{oc} of ~30 mV after degradation is achieved by the insertion of the optimized buffer layer, the fill factor in the degraded state is comparable to that of the corresponding solar cell without a buffer layer.

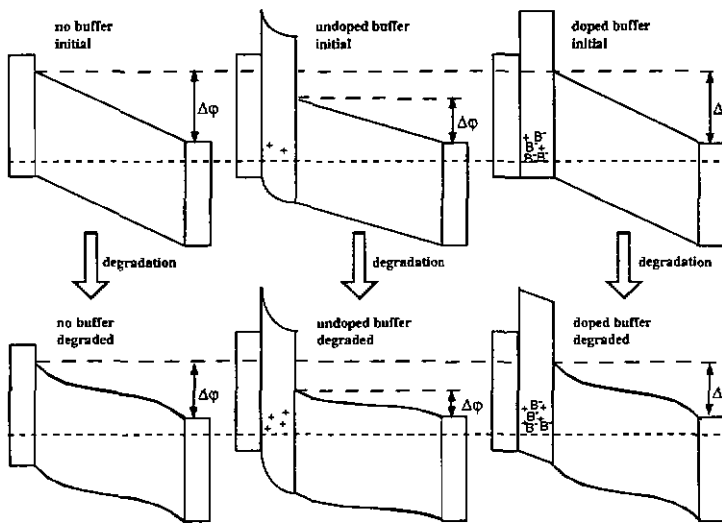

Figure 41: Sketch of the band diagram of solar cells without buffer layer (left), with undoped (middle) and boron-doped buffer (right) in the initial (top) and light-soaked (bottom) state. Δφ indicates the resulting potential difference within the i-layer.

The improvement of FF and V_{oc} due to the boron doping of the buffer layer can be understood in terms of the electric field in the solar cell. Figure 41 shows a sketch of the band

diagrams for solar cells without buffer layer (left), containing an undoped (center) and a boron-doped (right) buffer layer in the initial (top) and light-soaked (bottom) state. Dashed horizontal lines indicate the potential difference (i.e. the electric field) within the i-layer for the different configurations. The electric field in a p-i-n solar cell is given by the gradient of the potential within the i-layer. The field is presumed to be constant if the i-layer material has a low defect density. For more defective intrinsic material, e.g. after degradation, the field is somewhat reduced close to the i/n-interface compared to the p/i-interface [e.g., 6]. a-SiC:H alloys have more defects than unalloyed a-Si:H. Those defects in the p/i buffer layer are positively charged according to the position of the Fermi level in the bandgap. Therefore part of the potential difference drops over the buffer layer which reduces the remaining potential difference across the i-layer (Figure 41, center). A smaller electric field in the i-layer results in a reduced fill factor (Figure 40). The defect density in the a-SiC:H buffer material increases even further during degradation resulting in an even larger potential drop over the buffer layer and a further reduced fill factor. The mechanism of boron doping is to compensate the positively charged dangling bonds in the buffer material with negatively charged boron atoms. The optimum doping density would thereby exactly compensate the defects of the material in the light-soaked state (Figure 41, right), resulting in an (idealized) constant electric field within the i-layer.

The explanation given above is confirmed by spectral response measurements on three different solar cells in the initial and the light-soaked state (Figure 42). In this case, the i-layer is made of a-SiC:H (40 % CH_4, H_2 dilution 10, 100 nm), the buffer layer consists of a-SiC:H made with 60 % CH_4 and and a H_2 dilution of ten. Spectral response measurements can give valuable information on the field distribution in a solar cell (I.4.2). The collection of red light in the solar cell incorporating the undoped buffer layer (Figure 42, center) is reduced already in the initial state (19 % loss at 600 nm compared to 7 % for the cell without buffer layer, Figure 42, top). After degradation, the difference is even more pronounced: 47 % of the carriers generated by light of 600 nm wavelength are lost in the cell incorporating a buffer layer, compared to 27 % for the solar cell without a buffer layer. We assume for this calculation that at a bias voltage of –3 V all light-generated carriers are extracted (i.e., $I(-3\ V)_{init} = I(-3\ V)_{degr.}$). At 0 V bias ($I_{sc}$ conditions), a certain amount of those light-generated carriers recombine within the i-layer due to a reduced internal electric field and do therefore not contribute to the cell current. Slight boron doping of the buffer layer can restore the electric field in the i-layer as is shown in Figure 42, bottom. The current loss at 600 nm is 8 % in the initial state and 28 % in the degraded state for this p/b-i-n solar cell with a slightly boron-doped buffer which is comparable with the values for the cell without buffer layer. *These experimental data confirm our explanation given above and demonstrate the* practicability of boron doping to maintain good cell performance in the initial and degraded state for solar cells incorporating a-SiC:H buffer layers.

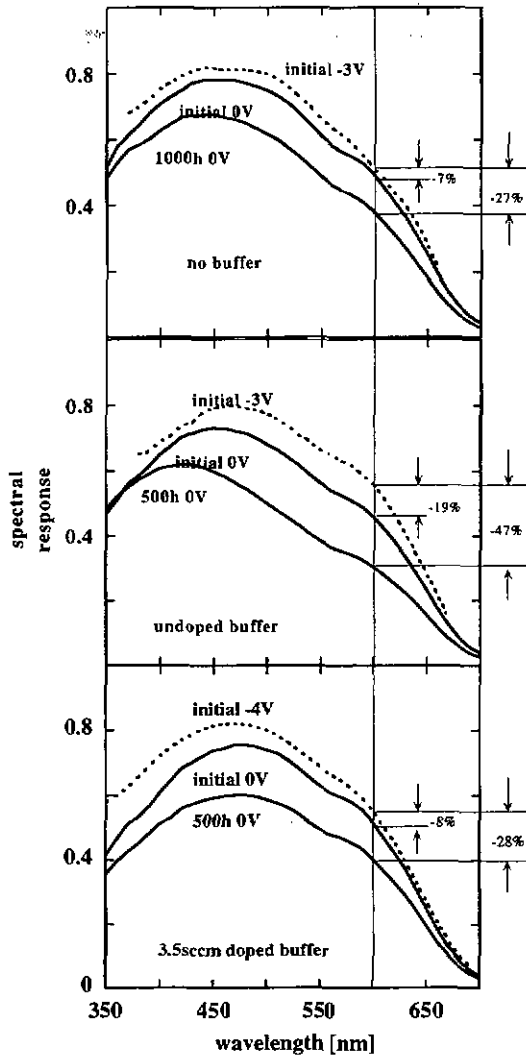

Figure 42: Spectral response data in the initial and degraded state for an a-SiC:H p-i-n solar cell without buffer layer and for solar cells containing an undoped and 3.5 sccm boron-doped buffer layer. The i-layer is the same for all three cells.

Figure 42 also shows a possible drawback of a boron-doped buffer layer. The insertion of the boron doped buffer layer reduces the blue response and therefore the current density of the solar cell slightly. Reasons are a weakening of the electrical field close to the p/i-interface, and possibly also slight boron contamination of the i-layer (see section III.4.3.3). In fact, the buffer layer is part of the active layer of the solar cell. If the amount of boron doping exceeds the necessary quantity, the buffer layer becomes more and more of a "thickened p-layer". In this case, free carriers generated by blue light in the buffer layer may experience a weak electric field together with a high defect density which is even increased by doping states. This results, in turn, in a decreased blue response of a solar cell incorporating such a boron-doped buffer layer.

III.4.2.2. Undoped a-SiC:H buffer layer as diffusion barrier

a-SiC:H buffer layers are also quite efficient diffusion barriers as will be shown in the following. The incorporation of an i-layer that is deposited at higher than standard temperature into a solar cell (section III.3.2) requires special care with respect to the p/i-interface. Figure 43 shows spectral response curves (measured under short circuit conditions, i.e. at 0 V bias) for two solar cells incorporating i-layers that are deposited at substrate

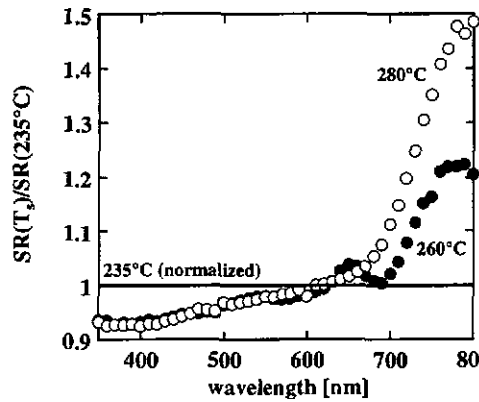

Figure 43: Spectral response curves (measured at 0 V bias in the initial state) for 300 nm thick p-i-n cells with i-layers deposited at 260 and 280°C from undiluted SiH_4 normalized to the SR(0 V) of a cell deposited at 235°C. In order to exclude experimental variation due to the reflectivity of the back contact, all three samples were contacted in the same run with silver contacts.

temperatures of 260°C and 280°C. The curves are normalized with respect to the SR of a "standard" p-i-n cell at 235°C. One clearly observes the desired increase of the SR in the long wavelength region due to the reduced optical bandgap of the i-layer material deposited at high temperature. At 750 nm the spectral response is increased by 35 % for the 280°C cell as compared to the "standard" 235°C cell.

This desired increase in the red spectral response with increasing T_s is, however, combined with a decrease in the blue wavelength spectral response. Figure 43 shows a decrease of the blue SR at 0 V bias for increasing i-layer deposition temperature. At a reverse bias voltage of -3 V, there is, however, no difference for the three temperature values which excludes a reduced transparency of the p-layer as the reason for the reduced blue response. We attribute this effect of a voltage-dependent blue SR to boron contamination of the i-layer due to diffusion of boron out of the p-layer and incorporation into the i-layer when heating it up. The internal electric field in the i-layer is reduced due to slight boron doping of the first part of the i-layer, which reduces the collection of electron-hole pairs generated by blue light close to the p-layer. Heating up of the p-layer in order to deposit the i-layer at higher T_s has also detrimental effects on the other cell characteristics, i.e. V_{oc} and FF.

An appropriate a-SiC:H p/i interface layer can reduce the problem of boron out-diffusion to a large amount. Figure 44 demonstrates the influence of such an optimized p/i interface layer (40 % CH_4, H_2 dilution rate 20) on the spectral response of solar cells with intrinsic

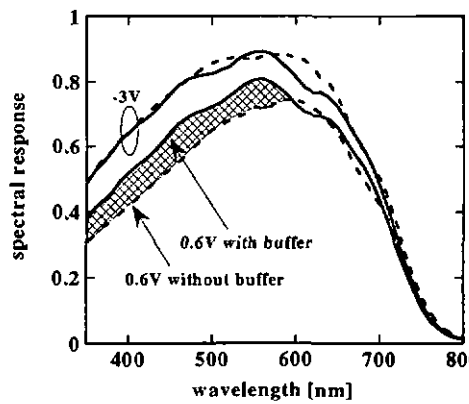

Figure 44: Spectral response curves measured in the initial state at –3 V and 0 V for a-Si:H solar cells with intrinsic layers deposited at 280°C. Dashed lines are for the p-i-n cell, full lines are for the cell with an a-SiC:H interface layer.

layers deposited at 280°C. The cell without interface layer clearly exhibits a large drop in the blue wavelength spectral response between -3 V and +0.6V. This is an indication for a weakened electric field close to the p/i-interface and therefore for boron contamination of the i-layer (Figure 47). The voltage dependence for the blue SR is considerably reduced for the solar cell incorporating the a-SiC:H buffer layer. The interface layer, deposited at the same temperature as the p-layer, acts as a diffusion barrier for boron atoms and prevents thereby the incorporation of boron into the i-layer during i-layer deposition at high temperature. A slight doping of the p/i interface layer due to boron diffusion into the interface layer has a positive effect on the performance of the device (previous section). Performance data and light soaking behavior of such cells made at enhanced substrate temperature are described in section III.3.2. In conclusion, a-SiC:H buffer or interface layers can play a double role in the case of p-i-n solar cells where the i-layer is deposited at enhanced temperature in order to reduce its optical gap. On the one hand, the a-SiC:H material is efficient as diffusion barrier, maintaining thereby a high blue response and a good fill factor. On the other hand, the V_{oc} of the solar cells is recovered to a certain extent due to the "buffer" effect of this interface layer.

III.4.3. Sources of i-layer contamination

The problem of the internal electric field in a p-i-n solar cell has been an important issue in the context of buffer or interface layers. In this case, the problem is mostly localized at the p/i-interface. The importance of drift-assisted collection and hence the electric field in a-Si:H

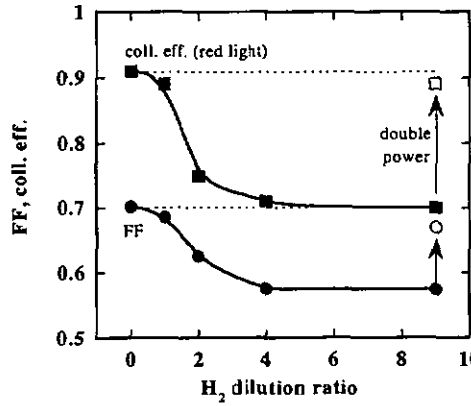

Figure 45: Fill factor (lower curve) and collection efficiency (= SR(0V) / SR(-3V)) @ 650 nm (upper curve) for solar cells with 450 nm thick i-layers made at varying H_2 dilution ratios at T_S = 195°C.

based solar cells has clearly been demonstrated. In this section, we are dealing with disturbances of the electric field that originate from a contamination of the entire i-layer of the solar cell.

The first observation of a possible contamination connected to H_2 dilution of the i-layer of the solar cells was a decrease of the fill factor and of the collection efficiency for red light with increasing H_2 dilution ratio (Figure 45). An increase of the input power during the i-layer deposition could recover the fill factor and collection efficiency at least partially.

Contamination problems can be divided into two groups: The first group is formed by problems connected to the single-chamber system used in this work. Those contaminations originate mainly from cross-contamination by the doping gases. The second group consists of problems that can also appear in multi-chamber systems. In this second group, we have to deal mainly with oxygen originating from different sources. We found both groups of problems to become much more important when depositing i-layers under H_2 dilution as will be developed below.

III.4.3.1. Oxygen

In fact, SIMS measurements [123] performed on our samples deposited with varying amount of H_2 dilution confirm that an increased amount of oxygen is incorporated if H_2 dilution is employed (Figure 46). Oxygen is believed to originate from the chamber walls and from impurities in the feedstock gases [124]. Due to the reduced growth rate when H_2 dilution is employed, the amount of oxygen incorporated into the layer is increased. Figure 46 demonstrates that the amount of oxygen in the layer increases with increasing H_2 dilution ratio (~$8 \cdot 10^{18}$ cm^{-3} for undiluted i-layer, $9 \cdot 10^{18}$ cm^{-3} at a H_2 dilution ratio of two and ~$2 \cdot 10^{19}$ cm^{-3} at dilution nine). Furthermore, oxygen incorporation is decreased when the layer is grown at higher rate (~3 Å/s @ 8 W instead of ~2 Å/s @ 4 W for dilution nine in Figure 46). Oxygen originating from the feedstock gases (mainly hydrogen) is present in the deposition chamber even after the H_2 dilution has been switched off as is shown by the higher oxygen concentration in a-Si:H deposited after a strongly diluted layer.

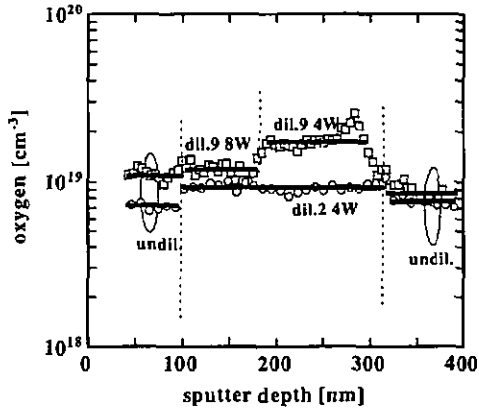

Figure 46: Oxygen concentration in samples deposited by the author, measured at the Forschungszentrum Jülich by SIMS [123]. Shown are depth profiles for two samples consisting of several layers with varying deposition parameters. H_2 dilution ratio and plasma excitation power was varied during deposition. Sample 1: undil. / dil.9 @ 4 W / dil.9 @ 8 W / undil.; sample 2: undil. / dil.2 @ 4 W / undil.

Oxygen is an n-type dopant [125] in a-Si:H. Doping of the intrinsic layer by contaminants leads to a shift of the Fermi level and hence influences the built-in electric field. Figure 47 illustrates in a very schematic way the band profile in a p-i-n solar cell with ideally intrinsic, slightly p-type and slightly n-type absorbing layer. For the intrinsic i-layer, the electric field i.e. the potential gradient within the absorbing layer is constant over the entire depth. The electric field acting on a light-generated free carrier is therefore in this simplified picture not a function of the generation depth. In the case of the p-type i-layer, the potential gradient is reduced close to the p/i-interface and enhanced close to the i/n-interface. Light-generated carriers generated by blue light, which is absorbed within the first part of the i-layer, experience therefore a reduced electric field, which enhances the recombination probability. The collection efficiency for carriers generated close to the i/n-interface is even slightly enhanced in this case. In the case of a n-type absorbing layer, which is the case for an oxygen-contaminated i-layer, the situation is inverted. The electric field is enhanced close to the p/i-interface and reduced close to the i/n-interface enhancing the collection of carriers generated by blue light and reducing the collection of carriers generated by red light [125] (Figure 45).

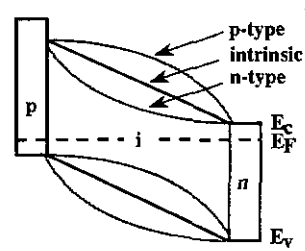

Figure 47: Sketch of the band profile for a p-i-n solar cell with ideally intrinsic, slightly n-type and slightly p-type absorbing layers.

In Figure 46 we have shown that varying H_2 dilution ratios cause varying oxygen incorporation into the i-layer. In Figure 48, we plot V_{oc} and FF* = FF · I_{sc} / I(-3V) for cells containing an i-layer deposited with constant H_2 dilution ratio of nine as a function of the out-

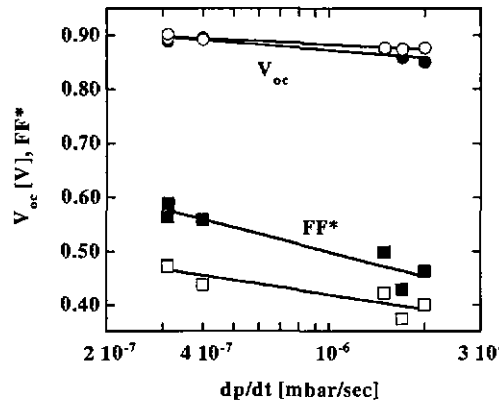

Figure 48: V_{oc} (●) and FF (■) before (black symbols) and after degradation (open symbols) for 450 nm thick cells as a function of the reactor out-gassing rate [mbar/sec]; reactor volume is 16.8 l. Substrate temperature was 195°C, i-layers are deposited with a H_2 dilution ratio of nine.*

gassing rate from the reactor walls. FF* decreases with increasing out-gassing rate due to an increasing amount of oxygen doping, whereas V_{oc} is almost not affected. The major loss in collection efficiency appears for red wavelengths. This confirms that water vapor coming from the walls is another major source of oxygen contamination. It is noteworthy that the relative degradation of the strongly oxygen-contaminated cells (Figure 48) is not stronger than that of the cells with a less contaminated i-layer.

In order to reduce oxygen contamination by out-gassing from the chamber walls, we heated the chamber walls overnight and cooled them down before deposition. Additionally, a gas purifier [124] was employed to withhold oxygen impurities in the feedstock gases. Figure 49 shows the resulting improvement in collection efficiency (= SR(0.6 V) / SR(-3 V)). Curve '1' corresponds to a cell where the i-layer is deposited without gas purifier, curve '2' is that of an identical cell, where a gas purifier has been employed for the i-layer. The i-layer has been deposited with a H_2 dilution ratio of nine. Note that in the case of the strongly

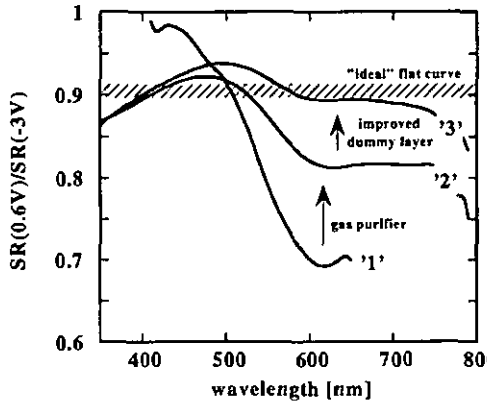

Figure 49: Effect of different types of contamination on the collection efficiency of a 450 nm thick p-i-n solar cell. Substrate temperature was 195°C, the i-layer was deposited with a H_2 dilution ratio of nine. Curve 1: i-layer deposition without special precautions. Curve 2: A gas purifier was used eliminating a large part of the oxygen contamination. Curve 3: The dummy layer after n-deposition was made using a strong H_2 dilution and low chamber pressure (0.2 mbar) thereby reducing the phosphorus contamination. The shaded bar indicates the collection efficiency for an "ideal" flat field distribution.

contaminated solar cell (curve '1') there is no loss in collection for carriers generated by blue light due to the enhanced electrical field close to the p/i-interface (Figure 47). We observe a drop in the blue response between –3 V and 0.6 V only once the strong n-type contamination and hence the field inhomogeneity is reduced below a certain limit.

III.4.3.2. Phosphorus

For curve '2' (Figure 49), the red collection efficiency is better than for curve '1' but not yet sufficiently high; we attribute this remaining imperfection to phosphorus contamination of the i-layer. This is a problem that typically appears in single-chamber reactors only. In the past, we deposited a "dummy layer" after the n-layer of each cell, which covers the electrodes and prevents phosphorus contamination of the next cell. This worked very well for cells deposited from undiluted or only slightly H_2 diluted SiH_4 plasma. When depositing the i-layer from a highly H_2 diluted plasma, we obtained an n-doping effect in the i-layer in spite of the dummy deposition. In fact, the strongly reactive H_2 plasma reaches uncovered parts of the reactor or parts that had been covered only with a thin dummy layer and etches the material containing phosphorus, which afterwards is incorporated into the i-layer. Conclusively, we next made the dummy layer also from a strongly H_2 diluted SiH_4 plasma and at the comparatively low pressure of 0.2 mbar. In this case the plasma is burning also outside the electrodes and covers all parts that can be reached afterwards by the plasma during i-layer deposition. Thereby we obtained a further reduction of collection losses in the red wavelength region as indicated by curve '3' in Figure 49 and a fill factor for the 450 nm thick cell of 70 %.

III.4.3.3. Boron

We have already noted that the collection of blue light is slightly reduced as soon as the strong n-type contamination is taken away. This is due to the equilibration of the electric field, yet possibly also to some extent due to boron contamination, which is then no more compensated by oxygen or phosphorus. Boron contamination also appears mainly in the case of single-chamber reactors. However, also for multi-chamber systems, boron contamination from the substrate holder is sometimes reported. In order to reduce boron contamination in our single-chamber deposition system, the substrate was taken out of the deposition chamber into the "load-lock" after the deposition of the p-layer. A CO_2 plasma at relatively high pressure (1 mbar) and high power efficiently removes boron from the chamber [126] when the i-layer is deposited without or with only small H_2 dilution ratios. However, when strong H_2 dilution is employed for the successive i-layer deposition, we find boron contamination in the i-layer, which is detected by a decreased collection for blue light. Operating the CO_2 plasma at low pressure (0.3 mbar) reduces the problem considerably; the CO_2 plasma then spreads out from between the electrodes and reaches all parts of the reactor.

III.5. V_{oc}-determining factors

Having reported above different means to increase the V_{oc} of a-Si:H based solar cells we compare in the following all factors influencing the V_{oc} directly. First, the V_{oc} is influenced by the optical bandgap of the intrinsic layer. An increase in the optical gap due to carbon alloying resulted for a-SiC:H solar cells in an increase in V_{oc}. The same effect has been obtained for a-Si:H solar cells where the optical gap of the i-layer is increased due to H_2 dilution and deposition of the solar cell at lower than standard temperature. Second, it has been demonstrated that p/i-interface (buffer) layers can increase the V_{oc} even further. In this paragraph we will directly compare V_{oc} values obtained for different types of a-Si:H based solar cells.

Figure 50 shows V_{oc} values in the initial and the light-soaked state obtained for various p-i-n solar cells as a function of the optical bandgap E_{04} of the i-layer. Black symbols indicate values in the as-deposited state, open symbols mark values after light soaking. In the initial state, the V_{oc} is an approximately linear function of the optical bandgap both, in the case of

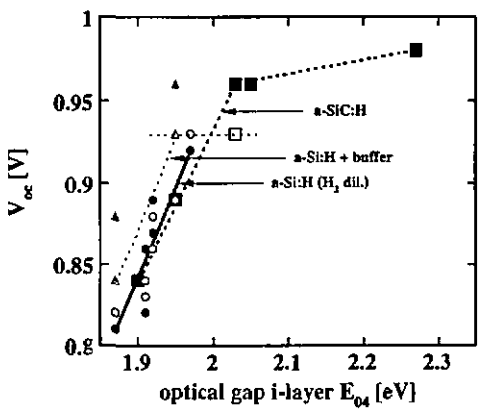

Figure 50: V_{oc} values as a function of the optical gap E_{04} of the i-layer for various p-i-n single-junction cells: a-SiC:H (■), a-Si:H with H_2 dilution (■) and a-Si:H solar cells with a-SiC:H buffer layer (▲). Black symbols indicate the initial state, open symbols for the light-soaked state. i-layer thickness is 100 nm for the a-SiC:H cells and 450 nm for the a-Si:H solar cells. The maximum value in the light-soaked state of 0.93 V is obtained for different types of solar cells with different i-layer materials.

a-Si:H (circles) and a-SiC:H (squares) i-layers as long as the optical gap E_{04} is lower than ~2 eV. For even higher values of the optical bandgap, the increase in V_{oc} is much weaker. The flattening of the curve for values of the bandgap exceeding ~2 eV is believed to be due to the drastic deterioration of the material quality of the a-SiC:H intrinsic layers on the one hand and due to limitations connected to the doped layers on the other hand. A deterioration of the material quality results in enhanced recombination within the i-layer, which is a V_{oc}-limiting factor. The doped layers are the same as those used for standard a-Si:H cells. Mainly the p-layer would need some modification in order to match i-layers with considerably increased optical bandgap [47].

The effect of light soaking on V_{oc} is minor in the case of a-Si:H layers with and without H_2 dilution (Figure 36) whereas a-SiC:H solar cells suffer considerable V_{oc} degradation. In fact, the best stabilized V_{oc} for an a-SiC:H solar cell, only 100 nm thick, is 0.93 V (Table 6, page 62) whereas the same value is obtained for a H_2 diluted a-Si:H solar cell, 450 nm thick, even though the optical gap of its i-layer is smaller than for the a-SiC:H cell. V_{oc} degradation is even more pronounced for a thicker a-SiC:H solar cell. These observations confirm once more that the use of H_2 dilution without carbon alloying is preferable for solar cells, both from the V_{oc} and the stability point of view.

Figure 50 also shows V_{oc} values for solar cells containing an a-SiC:H buffer layer together with an a-Si:H intrinsic layer (triangles). Here also, a stabilized V_{oc} of 0.93 V is obtained, however with a slightly smaller optical bandgap of the i-layer. Together with a "standard" i-layer (no H_2 dilution, 235°C), the a-SiC:H buffer layer results in an initial V_{oc} of ~0.88 V and a stabilized value of ~0.84 V. Direct comparison of the degradation behavior of such a p/b-i-n solar cell with standard i-layer to a cell with a similar initial V_{oc} value (~0.88 V) but deposited using H_2 dilution at low temperature (195°C) results in I-V parameters in the light-soaked state as listed in Table 7.

	V_{oc} [V]	I_{sc} [mA/cm^2]	FF	efficiency [%]
a-SiC:H buffer	0.84	14.6	0.53	6.5
H_2 dilution	0.88	14.1	0.56	6.9

Table 7: Comparison of a p/b-i-n solar cell (235°C, optimized boron doped buffer) and a H_2 diluted p-i-n solar cell (195°C, H_2 dilution ratio of two) in the degraded state. i-layer thickness is 450 nm in both cases.

Both V_{oc} and FF after degradation are higher for the H_2 diluted cell than for the cell containing a buffer layer, resulting in a higher stabilized efficiency. However, the short circuit current density is higher for the solar cell with an undiluted i-layer. We therefore conclude that highest values of the stabilized V_{oc} are obtained using a H_2 diluted i-layer at

reduced deposition temperature. These cells also are characterized by an excellent stability against light soaking (Figure 39). However, due to the increase in the optical gap upon H_2 dilution and deposition at reduced temperature, the current level of such cells is considerably reduced compared to solar cells where the i-layer is deposited at standard temperature and without H_2 dilution. Therefore, if a high current level is desired, an optimized a-SiC:H buffer layer may be an interesting alternative to H_2 diluted solar cells to obtain enhanced V_{oc} values, as will be discussed in section IV.3.

III.6. Conclusions: three deposition techniques "à la carte"

In conclusion, we have, based on the results of chapter II on materials, developed and optimized a variety of single-junction solar cells which differ mainly in their optical gap, i.e. the ability to absorb light. As the optical gap influences the voltage of the solar cell, we have to deal with a tradeoff between current and voltage, where the light soaking behavior adds yet another component. Interface layers have been optimized in order to add an additional degree of freedom to the general correlation between the optical gap, i.e. the current level of a solar cell, and its voltage. Even though not all cells reach the optimum performance from the single-junction cell point of view, each cell deposition technique has its special advantages, depending on the requirements for the solar cell.

Figure 51 shows I-V parameters in the degraded state for thickness series of the three most promising a-Si:H single-junction cell deposition techniques which have been described in this work. Diamonds indicate "standard" p/b-i-n solar cells. The i-layer is made from undiluted SiH_4 plasma at the standard temperature of 235°C. The V_{oc} of these solar cells is enhanced by means of an a-SiC:H buffer layer which is deposited using strong H_2 dilution (ratio 20) and boron doping in order to enhance the stability against light soaking (III.4.2.1). Squares indicate solar cells deposited at the reduced temperature of 195°C and using a graded H_2 dilution ratio for the deposition of the intrinsic layer as described in section III.4.1 of the

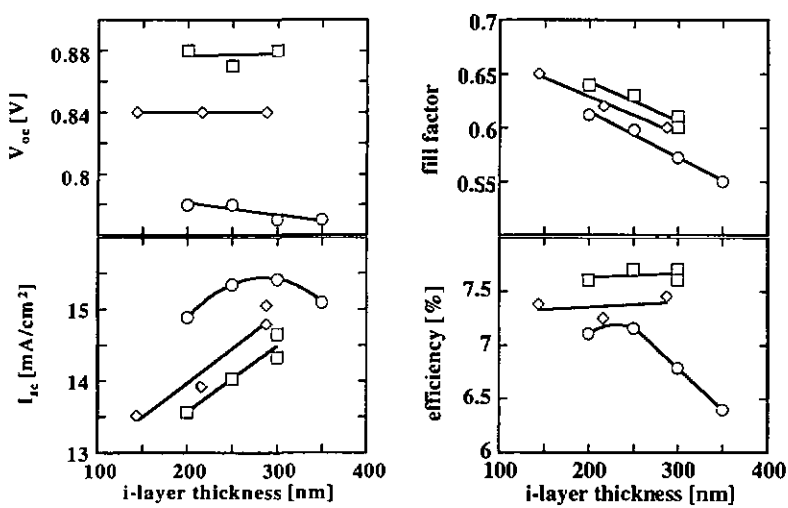

Figure 51: I-V parameters in the light-soaked state as a function of the i-layer thickness for three different cell deposition techniques: "standard" p/b-i-n solar cells (◊), low-temperature cells with H_2 diluted i-layer (□) and high-temperature p/b-i-n cells (○).

present chapter. Solar cells with intrinsic layers deposited at the enhanced substrate temperature of 280°C are indicated by circles. These solar cells contain an a-SiC:H interface layer to enhance the V_{oc} and as barrier against boron out-diffusion (III.3.2).

These three a-Si:H solar cell deposition techniques developed within this work offer a large choice of possible combinations between V_{oc} and I_{sc}. V_{oc} is as high as 0.88 V for the low-temperature cells, ~0.84 V for the standard cells and ~0.78 V for the solar cells with high-T_s i-layers. The short-circuit current density scales inversely with the optical gap of the i-layer. Increasing the temperature for the i-layer deposition to 280°C increases the current by ~0.8 mA/cm^2 compared to the standard cells. However, for i-layer thickness exceeding 300 nm, enhanced current degradation of the high-T_s cells (Figure 38) reduces the gain considerably. Fill factors in the degraded state are comparable for all three types of cells; high-T_s show slightly lower, low-temperature H_2 diluted cells slightly higher values than standard p/b-i-n cells. The highest stabilized efficiency for single-junction cells is obtained for the low-temperature H_2 diluted solar cells. A stabilized efficiency >7.5 % marks a considerable improvement compared to values that have been obtained in our laboratory so far. Such single-junction cells are certainly an interesting approach when not the highest possible power but an economic solution is required. "Standard" p/b-i-n solar cells with the improved buffer layer stabilize at slightly lower efficiencies. High-T_s solar cells are at the present state certainly not interesting as single-junction cells but a possible solution as top cells for micromorph tandem cells as will be shown in the next chapter. A stabilized efficiency of up to 7 % for our high-T_s p/b-i-n cells demonstrates, however, that it is possible to deposit reasonably efficient solar cells with reduced optical gap due to high substrate temperature also by employing the "conventional" p-i-n structure.

The large variety of technological approaches which has been presented in this chapter is the starting point for an optimization of a-Si:H/a-Si:H stacked cells and of the micromorph tandem cell, which is the content of the next chapter.

Finally, let us note that future applications with altered requirements may ask for yet another type of solar cell. Certain promising paths and tools are sketched, detailed optimization has, however, to be performed on the background of the application.

IV. Tandem solar cells

IV.1. Introduction

A tandem or stacked structure is of double interest for a-Si:H based solar cells. It has been mentioned in section 1.1.1 above that a multi-junction solar cell structure with different optical gaps of the component cells bears the potential to considerably increase the efficiency of the solar cell. Due to a splitting of the solar spectrum photo-generated carriers loose less energy due to thermalization to the band edges. Ma et al. [138] predicted in 1993 a maximum efficiency exceeding 30 % for a double stacked (4-terminal) structure with bandgap energies of 2.1/1.15 eV or 2.3/1.4 eV for the top/bottom cell. The second interest for tandem structures of a-Si:H solar cells regards the stability against light soaking. In fact, the increased electric field in a thinner i-layer of a solar cell leads to less recombination events and therefore reduced degradation. At the same time the solar cell can, for the same reason of an enhanced electric field, tolerate a higher defect density in the i-layer and still maintain good current collection. The light absorption is distributed into two solar cells, each of them thinner than

structure	p-i-n	n-i-p	lab.	*efficiency* [%]	comment
a-SiC:H/a-Si:H	x		Fuji	10.8 [50]	initial eff.
a-SiC:H/a-Si:H/a-SiGe:H	x		Solarex	9.15 [127]	active area, >900 cm^2
a-SiC:H/a-SiGe:H/a-SiGe:H		x	Sharp	10.2 [128]	
a-Si:H/a-Si:H	x		Fuji	10.0 [129]	
	x		FZ Jülich	9.2 [130]	
		x	**USSC**	**10.1** [81]	
a-Si:H/a-Si:H/a-SiGe:H		x	Sharp	~9 [52]	
a-Si:H/a-SiGe:H	x		Solarex	9.6 [131]	
	x		Sanyo	10.6 [132]	
		x	**USSC**	**11.2** [81]	
a-Si:H/a-SiGe:H/a-SiGe:H		x	**USSC**	**13.0** [116]	
a-Si:H/μc-Si:H	x		**IMT**	**12.0±0.6** [133]	outdoor measurement, unconfirmed
	x		IMT	10.7 [134]	independently confirmed
		x	IMT	8.4 [135]	
		x	Canon	11.5 [136]	
		x	Kaneka	11.1 [137]	

Table 8: Various a-Si:H tandem cell structures and corresponding solar cell efficiencies.

the single-junction solar cell which would generate a current density corresponding to the sum of both cells. Both cells are connected in series, leading to addition of the voltages at roughly half the current density of a corresponding single-junction cell. The total current potential is determined by the optical gap of the bottom cell i-layer. The enhanced voltage (sum of top and bottom cell voltage) and reduced current produce additional advantages regarding ohmic losses due to series resistance (e.g., front and back contacts). We distinguish, for clarity, between stacked and tandem solar cells below. Stacked solar cells consist of same-bandgap component cells, whereas a tandem cell is a device containing two or more solar cells with pronouncedly different optical bandgap.

Table 8 gives some examples of a-Si:H-based stacked and tandem cell structures. One can see that basically any possible combination of a-SiC:H, a-Si:H, a-SiGe:H and, more recently, μc-Si:H solar cells has been considered. Not all of them, however, have yielded stabilized efficiencies that are competitive to the best values. We marked in bold the highest stabilized efficiencies for the most commonly used tandem or stacked cells. a-Si:H/a-Si:H (same bandgap) stacked cells have yielded stabilized efficiencies of 9-10 % on the laboratory scale. Further efficiency improvement is limited by the absorption of the (unalloyed) a-Si:H, limiting the total current density to ~17-18 mA/cm^2, depending on the deposition temperature and the employed light-trapping "tools". a-SiGe:H alloys enhance the potential for the stabilized efficiency due to a higher current level. Microcrystalline silicon solar cells, as pioneered by our group at IMT, combine enhanced current generation, similar to a-SiGe:H alloys, with absolute stability against light soaking and are therefore a very interesting new candidate for the bottom cell in tandem structures, as will be discussed in section IV.3 below.

In the present work we deal with two of the approaches to enhance the stabilized efficiency, which have been presented above: in section IV.2 below, a-Si:H/a-Si:H stacked cells with high stabilized efficiency are developed. In section IV.3, we discuss the choice of an amorphous top cell deposition technique for incorporation into a-Si:H/μc-Si:H tandem ("micromorph") solar cells and the efficiency potential of such tandem solar cells.

IV.2. a-Si:H/a-Si:H stacked cell

We have described single-junction solar cells with stabilized efficiencies of 7.5 % in section III.6 above. In order to raise the stabilized efficiency beyond this value, the light-induced degradation has to be further reduced. This goal can be achieved with the stacked cell approach. In a stacked cell, the same amount of light is absorbed and converted into current as in a single-junction cell; however, both the i-layers are thinner than the i-layer of the single-junction solar cell, which, in turn, results in reduced degradation. We will show below that careful adjustment of the current matching between both component cells is an important factor in the optimization of stacked solar cells. We first study the influence of current matching on the stacked cell I-V curve by means of a simple semi-empirical model and describe thereafter the technological realization of a VHF-deposited stacked solar cell with a stabilized efficiency of 9 %.

IV.2.1. Semi-empirical modeling of stacked cells

We developed a simple semi-empirical model to calculate tandem or stacked cell I-V curves on the basis of I-V curves of the component cells. The model uses measured I-V curves of solar cells and allows us to study the influence of current mismatch between the component cells on solar cell efficiency. In order to estimate the I-V curve of a stacked cell, we simply add the V(I) curves of both component cells, as is illustrated in Figure 53:

Equation 16

$$V_{tandem}(I) = V_{top}(I) + V_{bottom}(I)$$

This corresponds to the electrical series connection of the two component cells. The solar cell with the smaller current density thereby limits the total current of the stacked cell.

A schematic flow-chart of the model is shown in Figure 52, annex VI.1 lists the MatLab routine. We use as input measured I-V curves for top and bottom cell. The main characteristics of these I-V curves is the FF value, which corresponds to the state of degradation and cell deposition technique chosen for the component cells.

In the next step, the current level of both components is scaled by multiplication of the current values with a constant factor. This allows us to redistribute the totally available current density I_{total} between the two component cells in order to study the influence of current mismatch on the stacked cell performance. The totally available current density I_{total} is determined, besides light-trapping mechanisms, by the optical gap and thickness of the bottom cell. In a stacked cell, this current I_{total} is redistributed into two component cells. Each of the component cells carries at the most $I_{total}/2$, and the tandem cell current is limited by the component cell with the smaller current. Scaling of the current values was done with respect

to the current value at -3 V, which corresponds to the value determined by optical absorption. At a large negative bias voltage all carriers are presumed to be extracted due to field-enhanced collection, also for solar cells in their light-soaked state. By writing the total generated current I_{total} as follows:

Equation 17

$$I_{total} = I_{top}(-3V) + I_{bottom}(-3V)$$

we do the current scaling with respect to optical conditions. We scaled the current levels of the component cells in order to obtain the desired degree of mismatch, keeping the sum of top and bottom cell current ($=I_{total}$) constant. For an a-Si:H/a-Si:H stacked cell we assumed this sum to be 15 mA/cm^2, accounting for a total optical loss of ~1 mA/cm^2 [139] in the inner n/p junction when the total current potential is on the order of 16 mA/cm^2 (Figure 36). In the case of a micromorph bottom cell (section IV.3), this current level is much higher because of

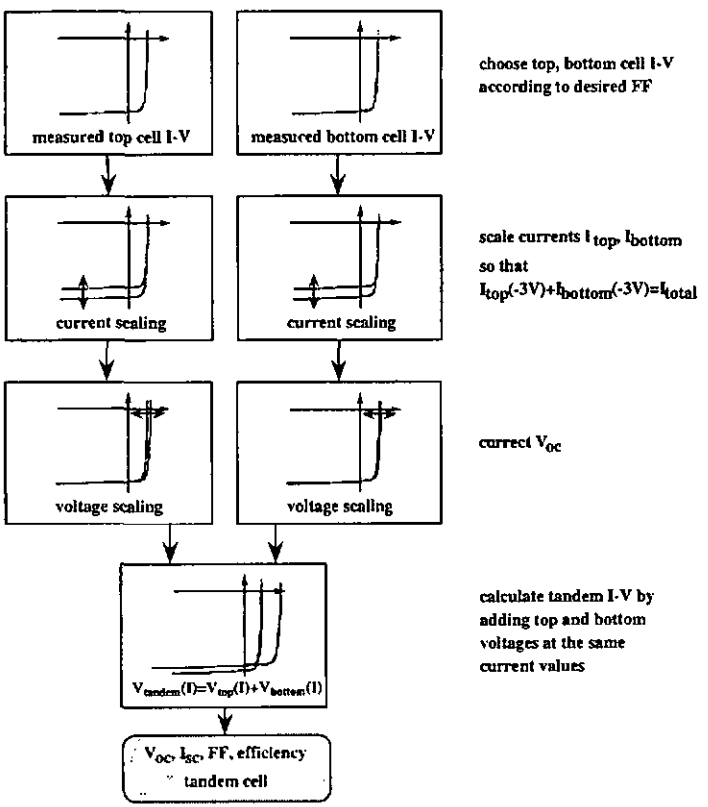

Figure 52: Flow-chart of the tandem cell modeling process.

the small optical gap of VHF-deposited μc-Si:H.

The model contains the possibility to slightly correct V_{oc} values of the component cells. This feature is of some interest only in the context of the modeling of micromorph tandem cells (section IV.3.3) and has not been used for a-Si:H/a-Si:H stacked cells. Scaling is done by simply multiplying voltage values of the measured I-V curve by a (small) constant factor.

Finally, the so-prepared measured I-V curves are simply added according to Equation 16, as is illustrated in Figure 53.

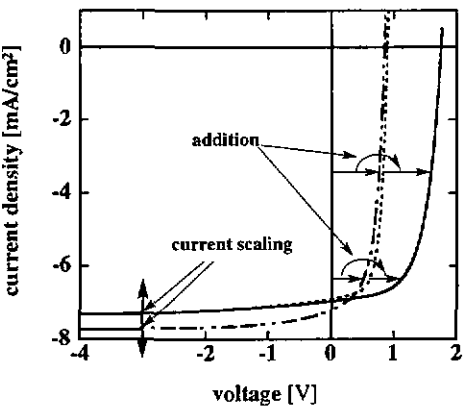

Figure 53: I-V curves of two single-junction solar cells and of the resulting stacked solar cell. The stacked cell I-V curve is obtained by addition of the V(I) curves.

This simple semi-empirical model is believed to describe the actual stacked cell quite well. It contains, however, some inexactitudes. First, the bottom cell in a real tandem cell sees only light filtered by the top cell, i.e. only the red part of the spectrum. By comparing I-V curves measured under white and filtered red light, we found, however, only minor differences. Second, the V_{oc} of a p-i-n solar cell depends on the surface morphology of the p/i-interface. In fact, we have observed that a solar cell deposited on flat TCO exhibits a V_{oc} that is about 40 mV higher than that of the same cell deposited on highly textured Asahi TCO. Therefore, the V_{oc} of the bottom cell may be under-estimated, taking into account a certain smoothing of the surface during deposition of the top cell. Third, the voltage of a solar cell depends logarithmically on the illumination intensity. A solar cell without back reflector (top cell) or a solar cell illuminated by red-filtered light (bottom cell) is therefore expected to provide a slightly lower voltage than the same cell in a single-junction cell structure. Last, the series resistance of a solar cell has less influence when the current density is reduced, as is the

case in a stacked or tandem cell. On the other hand, the inner n/p junction has to be optimized such as to minimize the additional series resistance [139] introduced by this junction. Keeping these minor inexactitudes in mind when interpreting the results, we contend that this model describes quite well the real I-V curve of a stacked cell and allows us to easily model the situation for different degrees of mismatch and degradation as well as for different top and bottom cells.

IV.2.2. Modeling of a-Si:H/a-Si:H stacked cells

Figure 54 (top) shows the dependence of the output power of an a-Si:H/a-Si:H stacked cell (= $V_{oc} \cdot I_{sc} \cdot FF$) on the current mismatch for different pairs of top and bottom cells. It has been shown that it is possible to reduce light-induced degradation by making the stacked cell top-limited [140]. For two cells with the same fill factor, the maximum output power is obtained for matched cell currents, i.e. the same current generation in top and bottom cell. In a realistic stacked cell, however, the bottom cell degrades to a larger extent than the thin and relatively stable top cell (see section IV.2.3). Thus, if we pair a top cell with a high fill factor with a bottom cell showing a lower fill factor, we observe a shift of the point of maximum power towards slighlly top-limited conditions (to the left in Figure 54, top). Reducing the difference in FF of the both cells, the maximum power is again obtained for a smaller mismatch. The model indicates that the optimum mismatch is found somewhere below a difference in current of 1 mA/cm^2, depending on the fill factors of both the top and the bottom cell. For realistic conditions, we expect an optimum mismatch to be around 0.5 mA/cm^2. Figure 54 (bottom) shows the FF values for the same conditions as in Figure 54 (top). The maximum output power is not found for maximum fill factor values which increase for increasing mismatch and are minimum around matched currents. For a high degree of mismatch, one can obtain very high FF values, however the power is low because of a small cell current. Note that Figure 54 shows a very wide range of mismatch. E.g. I_{top}-I_{bottom} = -6 mA/cm^2 means 4.5 mA/cm^2 for the top cell and 10.5 mA/cm^2 for the bottom cell. Figure 54 (bottom) shows furthermore experimentally obtained FF values for a set of ten a-Si:H/a-Si:H stacked cells with varying current mismatch in the initial and degraded state. The current value of the top (bottom) cell is determined from SR measurements. A voltage bias corresponding to the V_{oc} of the bottom (top) cell of the stack and a red (blue) light bias is applied in order to measure the SR of the top (bottom) cells.

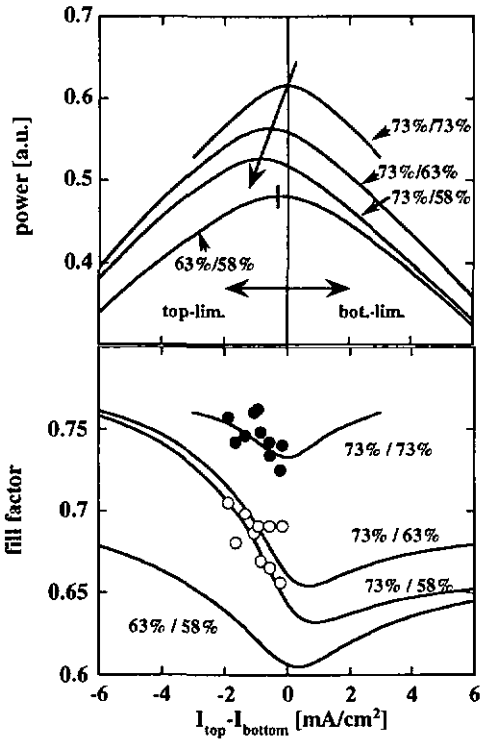

Figure 54: Modeled output power (top) and fill factor (bottom) values for a-Si:H/a-Si:H stacked cells as a function of the "mismatch", i.e. of the difference in current density between top and bottom cell. The sum of top and bottom cell current density ($I_{total} = I_{top} + I_{bottom}$) was held constant at 15 mA/cm^2. Percentage values next to the curves mean fill factors of the top/bottom cell. E.g. 73 % / 58 % means 73 % FF for the top cell and 58 % FF for the bottom cell. The symbols in the fill factor plot indicate experimental fill factor values in the initial (black symbols) and degraded (1000 h, open symbols) state for a set of ten a-Si:H / a-Si:H stacked cells deposited at T_s = 195°C / 235°C for the top / bottom cell.

The experimental data also entered (as points) in Figure 54 confirm the qualitative prediction of the semi-empirical model. Fill factors of bottom and top cell are comparable in the initial state, whereas the FF of the bottom cell in the degraded state is lower than the FF of the top cell because of the large difference in thickness of the two cells. The thickness of the top cell is 50-80 nm, whereas the bottom cell thickness is ~300 nm. Furthermore, the top cell is made of strongly H_2 diluted i-material, whereas the bottom cell contains mainly undiluted material, as will be discussed in more detail in section IV.2.3 below.

Our simple semi-empirical model suggests, in conclusion, that one should maintain slightly top-limited conditions in the degraded state in order to obtain the maximum power output after degradation. The optimum amount of current mismatch depends on the difference between degraded top cell and bottom cell fill factors and has to be optimized in function of the deposition technique used for the top and bottom cell.

IV.2.3. Technological realization

The concept of the graded H_2 dilution ratio in a solar cell has already been presented in section III.4.1. We used this concept in the top cell of our a-Si:H/a-Si:H stacked cell. The first part (~20 nm) of the i-layer is deposited with a H_2 dilution ratio of nine to obtain the maximum possible voltage of 0.88-0.9 V. The bulk of the i-layer is deposited employing a H_2 dilution ratio of two in order to obtain good stability against light soaking and to generate a sufficient amount of current.

An initial efficiency of 10 % requires a current density of 7.7 mA/cm^2 for the stacked cell, assuming a V_{oc} of 1.75 V and a fill factor of 74 %. This means, in turn, a current density of at least 8 mA/cm^2 for the bottom cell in the initial state in order to maintain top-limited conditions after degradation (see above). This current density, however, is not achievable with a diluted i-layer in the bottom cell and at low temperature (195°C). Figure 36 shows that the current density which can be obtained with a thick (450 nm) solar cell is of the order of 16 mA/cm^2 when the i-layer is deposited using a H_2 dilution ratio of two. Taking into account optical losses at the internal junction and a certain amount of current degradation, 8 mA/cm^2 can not be obtained within such a bottom cell. We developed therefore a process using different substrate temperatures for top and bottom cell, providing thereby a higher current density within the bottom cell as is described in the following.

IV.2.3.1. Two-temperature process

It is desirable to deposit the top cell at reduced temperature and with H_2 dilution in order to obtain high V_{oc} and good stability of the top cell. Reduced current generation due to the increased optical gap can here easily be compensated by increasing only slightly the thickness of the top i-layer. As stated above, it is, however, not possible to obtain a

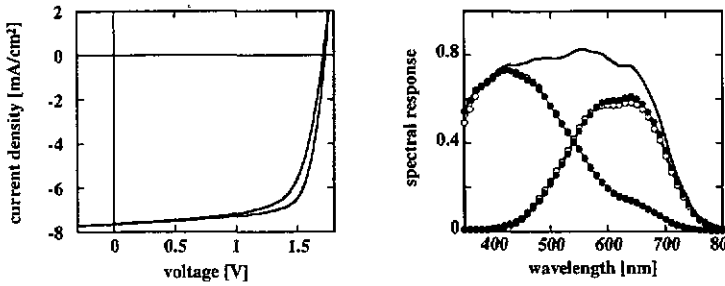

Figure 55: I-V-curve of an a-Si:H/a-Si:H stacked cell as described in section IV.2.3.2 with a stabilized efficiency of 9 % (left). Initial: 1.73 V, 74 % FF, 7.65 mA/cm², 9.8 %. 1000h degraded: 1.71 V, 69 % FF, 7.64 mA/cm², 9.0 % efficiency. Right: spectral response curves for the tandem cell in the initial (black symbols) and light-soaked (open symbols) state. Also shown is the sum of top and bottom cell SR in the initial state.

sufficiently high current density when the bottom cell, also, is deposited at low substrate temperature. We therefore deposited the bottom cell at the standard temperature of 235°C and without H_2 dilution in order to avoid an increase in optical gap. Again, a thin buffer layer of intrinsic material deposited with a H_2 dilution ratio of nine was inserted at the p/i-interface to enhance the V_{oc} of the bottom cell. By employing this technique of depositing top and bottom cells at different temperatures, the bottom cell provides enough current and can still be relatively thin. During the deposition of the bottom cell, the top cell is temporarily heated up to temperatures above its deposition temperature. This results in a reduction of the V_{oc} value of the top cell by ~30 mV. This value is determined by comparing the V_{oc} to values for stacked cells where both cells have been deposited at the lower substrate temperature. Our VHF deposition process, resulting in a high growth rate, provides a clear advantage in this case as the total time during which the top cell is held at high temperature for the deposition of the bottom cell is relatively short. The temperature is raised after p-layer deposition for the bottom cell and decreased immediately after the deposition of the bottom i-layer.

IV.2.3.2. a-Si:H/a-Si:H stacked cell with 9 % stabilized efficiency

Using a technological concept as described above, we deposited such a "two-temperature" p-i-i-n-p-i-i-n stacked cell. The initial efficiency of the solar cell is 9.8 %, after 300 h degradation the efficiency stabilizes at 9 % (8.6±0.6 % according to measurement by the Fraunhofer Institute (FhG-ISE) at Freiburg, Germany) which means a relative degradation of only 8 % (Figure 56). Degradation is partly due to V_{oc}, the fill factor decreases from 74 % to 69 %. The current mismatch between the component cells is 0.56 mA/cm² in the initial

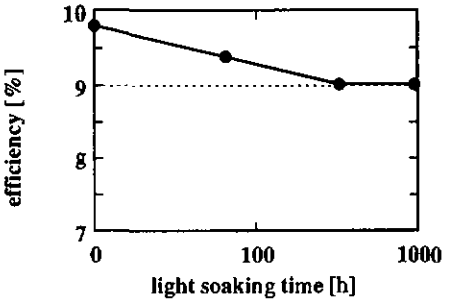

Figure 56: Degradation kinetics of the cell shown in Figure 55. Saturation appears after 300 h light soaking at 50°C under open-circuit conditions.

state. This mismatch is reduced to about 0.3 mA/cm^2 in the degraded state, due to degradation of mainly the bottom cell short-circuit current density. The performance of this solar cell confirms our statement based on semi-empirical modeling that optimized stabilized power of a stacked a-Si:H/a-Si:H solar cell can be achieved when a slight current mismatch between the component cells with different fill factors is maintained after degradation. The solar cell with the higher fill factor in the degraded state (the top cell in our case) should limit the stacked cell current.

IV.2.3.3. Process time

We would like to emphasize at this point the advantage of the VHF technology compared to conventional 13.56 MHz plasma deposition. It has been shown in section II.2.3 that plasma excitation at 70 MHz results in considerably enhanced growth rates compared to standard RF deposition. It has furthermore been shown that the VHF technology is suited to obtain stabilized solar cell efficiencies that are comparable to those obtained by RF deposition under otherwise similar technological conditions [130].

Even though still a number of industries (e.g. NAPS France [141], APS [113], Solems [142]) deposit cells in a single-chamber system, most solar cells are deposited in a multi-chamber reactor. Single-chamber systems can be an economically interesting alternative to expensive multi-chamber systems. Most of the contamination problems discussed in section III.4.3, however, are considerably reduced for multi-chamber systems.

Figure 57 shows a flow chart of our a-Si:H/a-Si:H stacked cell deposition process in a single-chamber reactor. Deposition and process times are indicated in the boxes. Total process time, including 20 min. of substrate pre-heating, is 98 min. Including the cleaning

step ("dummy layer", intrinsic layer deposited on a stainless steel substrate) after the last n-layer to prevent phosphorus contamination of the subsequent solar cell, the whole stacked cell can be made in less than 2 $^1/_2$ hours. For the deposition alone, including the i-layers deposited with H_2 dilution, we need only 22 min. This low value is obtained by employing the VHF deposition process. Thus, the largest part of the entire process time is used here for cleaning steps in between doped and intrinsic layers, which are necessary because of our single-chamber reactor. Schropp et al. [141] report for a stacked cell deposited also in a single-chamber (but at 13.56 MHz) a deposition time of at about 130 min. without any cleaning step in between doped and intrinsic layers and furthermore without H_2 dilution for the i-layers. The H_2 diluted i-layer of the solar cell presented in this work has been deposited at a rate of 4 Å/s, which is at least four times the value obtainable with RF plasma excitation (II.2.3.3).

It would be interesting to compare the above solar cell results to data for DC plasma excitation. This technique has been found (section II.2.3) to yield intrinsic a-Si:H of essentially the same quality in the light-soaked state as our VHF material and furthermore at growth rates which are on the same order as rates obtained for VHF excitation.

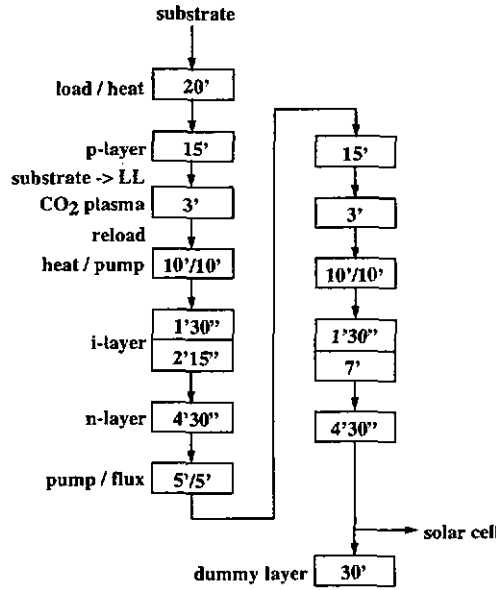

Figure 57: Process sequence for a-Si:H/a-Si:H stacked cell deposition using VHF plasma excitation. i-layer deposition is split off into "buffer" layer and bulk deposition.

IV.2.4. Conclusions

We have shown by means of a simple semi-empirical model that it is very important to carefully balance the current in a tandem or stacked cell in order to obtain optimized performance in the degraded state. The component cell with the higher FF value in the degraded state (i.e. the top cell in an a-Si:H/a-Si:H stacked cell) should slightly limit the current in a stacked or tandem cell.

VHF plasma excitation yields 9 % stabilized efficiency in an a-Si:H/a-Si:H stacked cell which is comparable to conventional RF technology under otherwise similar conditions. The main advantage of the VHF technology is the growth rate, which is at least a factor of four higher compared to RF plasma excitation. The question of the growth rate is even more important for deposition with H_2 dilution, which generally results in a considerable decrease in growth rate. We have demonstrated that an entire stacked solar cell containing i-layers deposited with H_2 dilution can be deposited by VHF-GD in 22 min. (cumulative layer deposition time). This is by far less than what can be obtained by RF plasma excitation.

IV.3. Micromorph tandem cell

IV.3.1. Special challenge for the top cell in a micromorph tandem

The discovery of microcrystalline silicon (μc-Si:H) as suitable absorber material for p-i-n solar cells has led to very interesting new developments in the field of solar cells using the a-Si:H technology. The characteristics of such entirely microcrystalline solar cells are very different from those of "conventional" a-Si:H solar cells: due to the low optical gap of ~1 eV, the current potential is considerably higher. At the same time, however, the voltage of such solar cells is so far comparatively low. So far microcrystalline single-junction solar cells have reached an efficiency of 8.5 % [143]. V_{oc} values as high as 0.53 V and current densities of up to 26 mA/cm^2 have been separately demonstrated in different single-junction cells. A very attractive point about μc-Si:H as new solar cell material is its absolute stability against light-induced Staebler-Wronski type degradation.

The pronounced difference in the optical gap of a-Si:H and of μc-Si:H makes a tandem solar cell containg both materials a very interesting approach. Combining an a-Si:H (top) cell with an μc-Si:H (bottom) cell enhances the efficiency potential compared to a μc-Si:H p-i-n cell alone due to the conversion of high-energy (blue/green) photons at higher energy level, i.e. voltage (section 1.1.1). While the total current potential for an a-Si:H solar cell is on the order of 16 mA/cm^2, μc-Si:H has the potential to provide current densities of up to 26 mA/cm^2. This value might even be exceeded in the future, if light-trapping in the solar cell can be further optimized. This high current density leads, in its turn, to considerable problems for the a-Si:H top cell of an a-Si:H/μc-Si:H tandem ("micromorph") cell. Due to the electrical series connection, such a top cell has to generate a current density which matches the current in the bottom cell, i.e. around 13 mA/cm^2 corresponding to a total cell current of 26 mA/cm^2 in a single-junction cell. This current density has to be generated without a highly reflective back contact, as used in a-Si:H single-junction solar cells to obtain high current density. Considering the difference in voltage between top (V_{oc} up to 900 mV) and bottom cell (so far ~500 mV), the top cell generates roughly two third of the output power. Degradation, on the other hand, is only due to the amorphous top cell. If a current density of 13 mA/cm^2 can, in principle, be obtained in a top cell without back reflector, such a cell has to be comparatively thick, which is undesirable from the point of view of stability.

This particular situation leads to requirements for the amorphous top cell which are very different from those for a-Si:H cells used as single-junction cells or in a-Si:H/a-Si:H or a-Si:H/a-SiGe:H tandem cells. In fact, the thickness of a top cell for a stacked or tandem solar cell is usually less than 100 nm, resulting in excellent stability, as has been shown above. The top cell of a micromorph tandem cell has to provide an extremely high current density and is solely responsible for the entire amount of degradation, rendering the stability issue even

more important. In the following we investigate the different a-Si:H cell deposition techniques developed within this work with respect to their performance in a micromorph tandem cell. We first examine the current potential as a function of the top cell thickness for four different top cell deposition techniques in a micromorph tandem cell. In a second step, we use measured I-V curves for amorphous and microcrystalline solar cells in a semi-empirical model to generate a "map" of the tandem cell efficiency as a function of top cell current and FF in the degraded state. Finally, based on these results, we present directions of further research with respect to their potential to enhance the stabilized efficiency of micromorph tandem cells.

IV.3.2. Choice of a top cell deposition technique

Since the fabrication of the first micromorph tandem cell in 1994 there has always been the question persisting which top cell i-layer material and which i-layer thickness would yield the highest overall stabilized efficiency. In the previous sections, we have studied various VHF deposited a-Si:H materials with respect to increasing stabilized efficiencies for purely amorphous single-junction and stacked cells. Similar to RF-deposited materials, H_2 dilution of the i-layer material has been found to result in enhanced stability against light soaking. However, H_2 dilution generally increases the bandgap of the a-Si:H material, which is particularly unwelcome in the context of micromorph cells with their high current density levels. Cells from standard a-Si:H material, produced without H_2 dilution together with a boron doped a-SiC:H buffer layer, have been shown to yield lower stabilized efficiency than cells produced with H_2 dilution. However, this type of solar cells becomes again interesting in the context of micromorph tandem cells, because of their comparatively high current generation. Finally, solar cells deposited at enhanced substrate temperature have been developed in order to further enhance current generation. We therefore have, at present, a choice of four types of solar cells (section III.6, plus H_2 diluted i-layer @ standard temperature) to select the optimum top cell for a micromorph tandem cell (Table 9). There is

Series	Description	Voltage	Current	Stability
A	"Standard" p/b-i-n @ 235°C	0	0	0
B_LT	H_2 diluted (graded) i-layer @ 195°C	+	--	+
B_ST	H_2 diluted (graded) i-layer @ 235°C	+	-	+
C	High-T_s p/b-i-n @ 280°C	-	+	0/-

Table 9: a-Si:H solar cell deposition techniques which have been optimized and their qualification with respect to application in micromorph tandem cells.

no unique relationship between the tandem cell efficiency and V_{oc}, current density and FF of the top cell. It is therefore not straightforward to predict the influence of various types of top cells on the performance of the micromorph tandem cell in the degraded state. We used a combination of experiment and modeling to clarify the influence of the different parameters on the tandem cell performance and therefore to determine the best suited a-Si:H deposition technique for the top cell of micromorph tandem cells.

IV.3.2.1. Experiment

Top cell deposition technique

As can be seen from Table 9, each of the four cell types has specific advantages and it is a priori not clear which point is the most important for the performance and stability of a micromorph tandem cell. We therefore prepared samples of various thicknesses for each of the four types and light-soaked the cells during 1000 h. In order to simulate the optical conditions for a top cell in a micromorph tandem cell (i.e., no back reflector), a thick (~1.5 µm) µc-Si:H n^+-layer was deposited on top of the n-layer of the a-Si:H single-junction solar cell. Contacts were made from chromium. The thick µc-Si:H n^+-layer together with the weakly reflecting Cr-contacts simulate optical conditions for a top cell in a micromorph tandem structure. Current enhancement in the top cell due to reflection at the back contact is suppressed. Figure 58 (left) illustrates the sample structure. We used glass coated with CVD-deposited ZnO as substrate and front contact, followed by a double µc-Si:H/a-Si:H p-layer. This double p-layer is required to provide a good electrical contact to the ZnO [144]. We used this double p-layer for all four cell series. In order to prevent lateral current collection

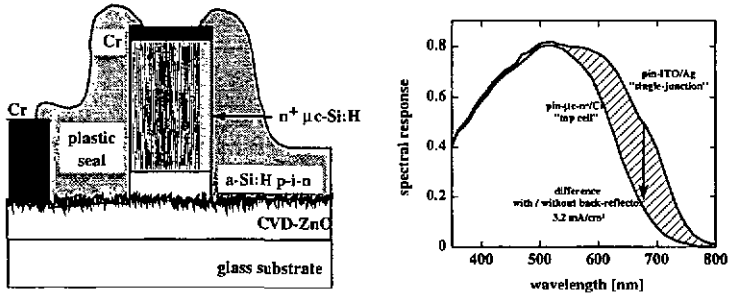

Figure 58: Sketch of the cell configuration for the degradation experiments (left) and comparison of SR curves for cells in this configuration to cells with highly reflective ITO/Ag back contact (right). The thick µc-Si:H n^+-layer together with the Cr contacts results in optical conditions like for a top cell in a micromorph tandem cell.

due to the very thick n^+-layer, we plasma-etched the solar cells around the contact pads. The Cr-contact acted as a mask. The entire substrate with the solar cells was encapsulated with plastic glue in order to seal the cells and prevent chemical reactions during degradation.

Figure 58 (right) compares SR curves for a thin p-i-n cell with ITO/Ag back contact and the same cell with a μc-Si:H n^+/Cr contact. Optical conditions and current generation in the amorphous top cell are therefore in those samples very close to the conditions in a "real" tandem cell.

Current densities I(-3 V) for the four cell series are plotted in Figure 59. V_{oc} and fill factor values of each series in the initial state are indicated next to the curves. The good fill factors of all samples indicate that the additional n^+-layer has no detrimental effect on the solar cell characteristics. Both, V_{oc} and FF, do not depend on the cell thickness in the initial state for neither of the four series, which confirms the quality of the intrinsic layers and the state-of-the-art solar cell technology.

Degradation of thickness series

All four series were degraded simultaneously under V_{oc} conditions. The spectrum was close to AM 1.5, temperature 50°C and light intensity corresponding to 100 mW/cm^2. Fill factor values in the light-soaked state (1000 h) as a function of the i-layer thickness of the

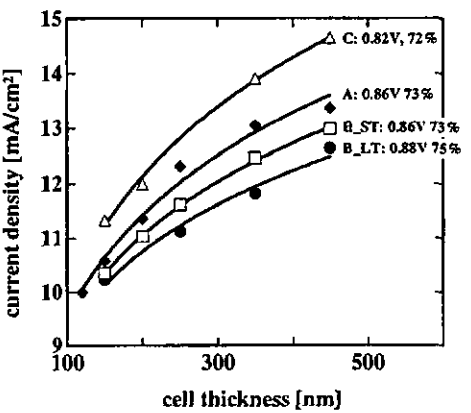

Figure 59: Current densities I(-3 V) as a function of the top cell thickness for the four cell series of Table 9. As-deposited V_{oc} and FF values for the four series are indicated next to the curves and do in the initial state within experimental error not depend on the cell thickness.

solar cells are plotted in Figure 60. The thickness series deposited on CVD-ZnO and containing a thick n^+-layer as sketched in Figure 58 showed enbanced degradation due to technological problems, which have been resolved meanwhile. The values shown in Figure 60 are obtained on solar cells in the "standard" configuration, i.e. deposited on Asahi SnO_2 substrates and contacted with highly reflective ZnO/Ag back contacts. The cell structure is otherwise identical.

Solar cells containing intrinsic layers deposited with H_2 dilution (series B) maintain the highest fill factors after degradation (Figure 60). Fill factors of series A and C are lower than the fill factors of series B. Quite satisfactory results had been obtained for single-junction solar cells with i-layers deposited at enhanced temperature of series C (section III.3.2). The deterioration of the cell performance for i-layer thicknesses exceeding 250 nm (Figure 38) has, however, already indicated that further work on this type of cells is needed in order to reduce damage due to the elevated deposition temperature.

For all four series, the open circuit voltage in the light-soaked state is almost independent of the i-layer thickness. Highest V_{oc} values in the degraded state are obtained for series B_LT (~0.89 V), followed by series B_ST (~0.87 V), series A (~0.84 V) and series C (~0.78 V). For the best cells on ZnO substrate, V_{oc} values are somewhat lower than the best values obtained in single-junction solar cells on Asahi SnO_2. The difference is for all four series on the order of ~20 mV. This can be explained to some extent by the lower generation rate in solar cells without back reflector. The V_{oc} of a solar cell is a logarithmic function of the light

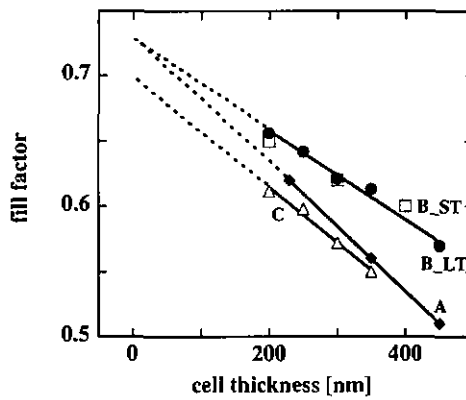

Figure 60: FF values for the four series of Table 9 after 1000 h light-soaking as a function of the thickness of the i-layer. Shown are values obtained for solar cells deposited on Asahi U-type SnO_2 TCO.

intensity. Taking the current density in such a top cell without back reflector as 70 % of the current density in a solar cell with a highly reflective back reflector, one can account for a loss in V_{oc} of [139]

Equation 18

$$\frac{kT}{e}\ln(0.7) \approx -10mV \ .$$

The remaining 10 mV may be attributed to the enhanced surface roughness of the CVD-ZnO which has been used as substrate for the sample series. The morphology of the p/i-interface affects the V_{oc} of p-i-n solar cells by influencing the reverse saturation current I_0 of the diode.

IV.3.3. Modeling of micromorph tandem cells

There is no straightforward relationship between the performance of a single-junction solar cell and a tandem solar cell incorporating this single-junction cell as top cell. This has already been shown for the case of a-Si:H/a-Si:H stacked cells in section IV.2.2. In order to study the influence of top cell parameters on the performance of micromorph tandem cells, we used the same model as for the a-Si:H/a-Si:H stacked cells. A detailed description of the model has been given in section IV.2.1, the only difference is the replacement of the (amorphous) bottom cell I-V curve by the I-V curve of a microcrystalline solar cell. I-V

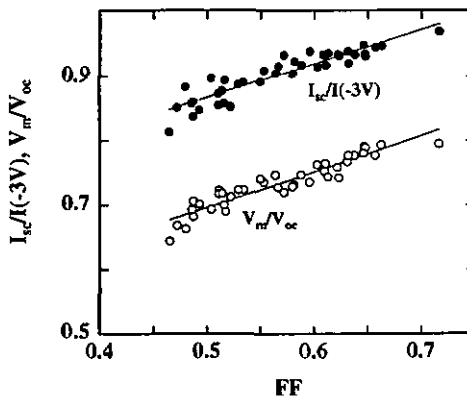

Figure 61: V_m/V_{oc} and $I_{sc}/I(-3V)$ as a function of the fill factor for I-V curves measured on various top cells (i-layer thickness, deposition technique, state of degradation).

curves of amorphous top cells in different states of light-soaking were used as input data for the top cells (I-V curves are shown in annex VI.2). These I-V curves were measured for the solar cells described above (section IV.3.2.1). For the bottom cell, we used the measured I-V curve (see annex VI.2) for a state-of-the-art microcrystalline bottom cell. V_{oc} and FF of this microcrystalline solar cell are 0.53 V and close to 70 %, respectively, which yields, combined with a current density of 23 mA/cm^2 a single-junction efficiency of 8.5 % [143]. On the other hand, a current density as high as 26 mA/cm^2 has been demonstrated in µc-Si:H solar cells. In order to study the potential of micromorph tandem cells, we assumed for modeling a combination of the above mentioned good V_{oc} and FF values (**0.53 V, 70 %**) and a current potential of **26 mA/cm^2**, obtained by scaling the current values of the measured I-V curve.

In a first step, we examined the question whether different types of a-Si:H solar cells, i.e. deposited using different deposition techniques, exhibit pronouncedly different I-V curves and result therefore in different tandem cell efficiencies for the same top cell FF. A priori, one could think of two possibilities: a) any a-Si:H based solar cell is sufficiently characterized by its FF, or b) solar cells can have the same fill factor but still very different I-V curves. One has to take into account that the FF only describes the collection losses

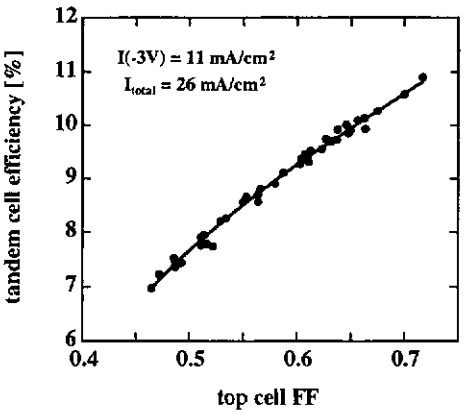

Figure 62: Modeled tandem cell efficiencies for various top cells. The top cell I-V curves are measured curves for solar cells of different deposition techniques and various states of degradation. V_{oc} values have been scaled to 0.85 V, current is 11 mA/cm^2 for the top cells and (26-11) mA/cm^2 for the bottom cell. The microcrystalline bottom cell is as described in the text (V_{oc} = 0.53 V, FF = 70 %).

between I_{sc} and the maximum power point. Theoretically, one could, e.g., shape an I-V curve with a low FF but high current collection between –3 V and 0 V (I_{sc}). In reality, however, such behavior is not commonly observed.

In order to provide an answer to the question whether all I-V curves are "geometrically identical" and are sufficiently described by their fill factor, we picked a large number of experimental I-V curves which had been measured on solar cells of all four deposition techniques. The set contains I-V curves for various i-layer thicknesses and different states of degradation. Figure 61 shows $I_{sc}/I(-3\ V)$ and V_m/V_{oc} as a function of the fill factor. Both geometrical factors of the I-V curve correlate with the FF. In other words, two I-V curves measured on solar cells of different deposition techniques, i-layer thickness or state of degradation, but showing the same FF, are geometrically identical. This statement is valid for a-Si:H based p-i-n cells investigated in this work.

In a second step, we modeled micromorph tandem cell I-V curves for the top cell I-V curves of Figure 61. V_{oc} values were normalized prior to modeling to 0.85 V by scaling the voltage values of the I-V curves; current values were adjusted so that $I(-3\ V) = 11\ mA/cm^2$. Figure 62 shows the resulting modeled tandem cell efficiency. Clearly, the tandem cell efficiency also only depends on the top cell FF, but not on the deposition technique, thickness or state of degradation of the top cell if identical V_{oc} and current values are taken (Figure 62). This confirms that I-V curves with the same FF value but measured on a-Si:H cells of different deposition technique are of very similar shape. It seems indeed reasonable to assume that current collection as a function of the applied voltage is a smooth function, depending mainly on the defect density in the intrinsic layer.

In consequence, the efficiency of a micromorph tandem cell is – for a given bottom cell – determined by voltage, current and FF of the top cell. Maximum tandem cell performance is, however, not obtained for the top cell with the maximum product of voltage, current and FF. As the top cell voltage is the parameter that varies the least, we based our model on a grid of FF and current density values for the top cell, but kept V_{oc} constant at 0.85 V. We took a measured I-V curve out of Figure 62 for each FF value. The tandem cell efficiency was then modeled as a function of the top cell current density by scaling the chosen I-V curve to yield the desired current value and subsequent computation of the tandem cell I-V curve. The same procedure was performed with the next experimental I-V curve, corresponding to another fill factor value. Thereby a grid of data points $\eta_{tandem}(FF_{top},I_{top})$ was obtained. All I-V curves used in the model are obtained by measurements on solar cells, the resulting "efficiency-map" represents, however, an extrapolation beyond presently experimentally available solar cells. E.g. current densities as high as 16 mA/cm^2 without highly reflective back contact (see Figure 58) have not been achieved in a-Si:H solar cells.

The resulting plot contains values that are valid for all types of top cells, i.e. all deposition techniques, provided this type of solar cell can provide the corresponding pair of current and FF. Efficiency values obtained are, however, calculated for a top cell V_{oc} of 0.85 V and have to be corrected for top cells with different V_{oc}. In a first-order approximation we set the correction as follows:

Equation 19

$$\eta_{corrected} = \eta_{modeled} \frac{V_{oc}^{top} + V_{oc}^{bottom}}{850mV + V_{oc}^{bottom}}$$

This approximation is valid as long as the real V_{oc} of the top cell is not too far from the value of 0.85 V, which has been used for modeling. The correction of the tandem cell efficiency due to a variation in top cell V_{oc} is, according to Equation 19, smaller than ±4 % relative as long as ΔV_{oc}^{top} (with respect to 0.85 V) is smaller than ±50 mV.

Limitations and minor inexactitudes of the model bave already been stated in section IV.2.1 above. The fact that we deal with a relatively new type of tandem solar cells and that furthermore relatively few experimental data are available adds some incertainty in the case of micromorph tandem cells. The purpose of our modeling is, however, to estimate the efficiency potential of such solar cells and evaluate directions of further research rather than to very precisely predict efficiencies.

IV.3.4. Results and discussion

IV.3.4.1. Present state

Tandem cell V_{oc} and I_{sc}

Figure 63 shows as a result of the above described modeling "maps" of micromorph tandem cell efficiency, I_{sc} and fill factor as a function of the top cell fill factor and saturated current density I_{top}(-3 V). The sum of top and bottom cell current densities available in the tandem cell was assumed to be 26 mA/cm^2 (= I_{total}). The open circuit voltage of the tandem cell corresponds to the sum of top and bottom cell V_{oc}, i.e. (0.85+0.53) V = 1.38 V. One would expect a somewhat lower V_{oc} in a tandem cell than what corresponds to the sum of both component cells, as has been discussed above. However, a small variation on the order of 10 mV does not have a substantial influence on the results and is therefore neglected in our model. Tbe short circuit current density of the micromorph tandem cell follows the increase in the top cell current (Figure 63, middle). A maximum is attained, and for even higher top cell currents the tandem cell current decreases again. The tandem cell current is first limited by the top cell (up to ~13 mA/cm^2), followed by limitation by the bottom cell as the sum of both component cell currents is limited to 26 mA/cm^2.

Tandem cell fill factor

The modeled overall fill factor of the tandem cell (Figure 63) is always higher than the fill factor of the corresponding single-junction top cell. This is can be explained by a "tandem effect" on the fill factor. Due to the electrical series connection, the component cell with the lower current level limits the current of the tandem cell. There are three possibilities for a

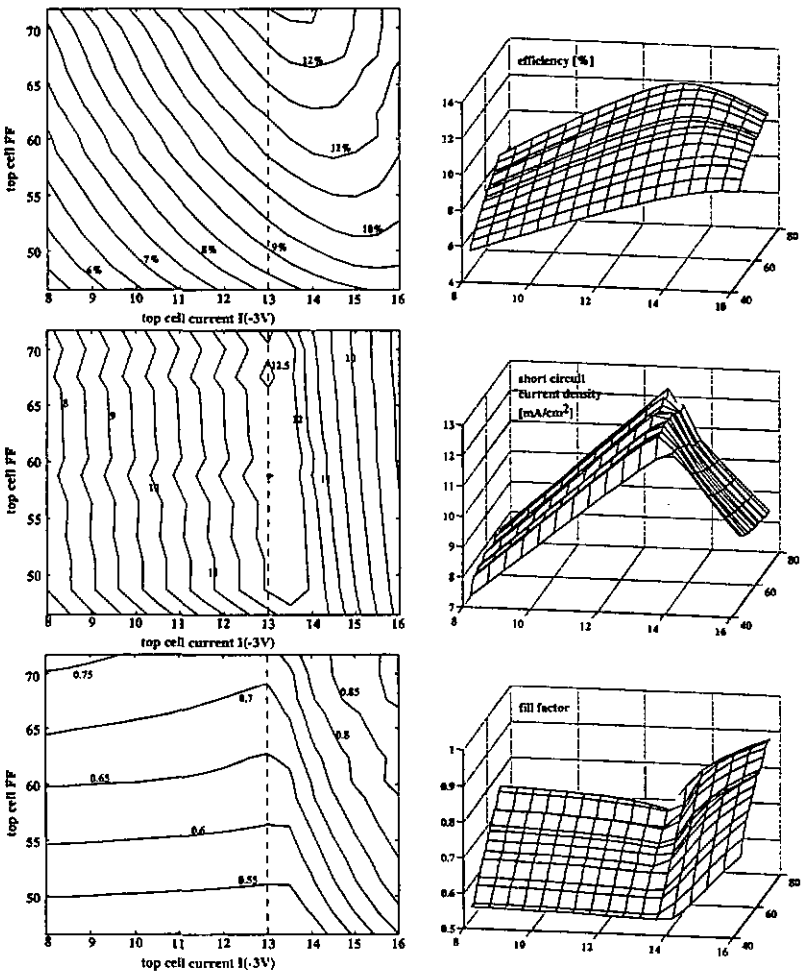

Figure 63: Modeled efficiency, FF and short circuit current density for micromorph tandem cells as a function of the FF and current level I(-3 V) of the amorphous top cell. Total current density (sum of top and bottom cell currents) is 26 mA/cm². V_{oc} of the top cell is 0.85 V, the bottom cell characteristics are as described in the text.

two-stacked solar cell: either top or bottom cell limit the current or both cells provide the same current density and the cell curents are matched. In the present case of a micromorph tandem cell, the top cell needs to be quite thick in order to generate a sufficiently high current density. The fill factor of an amorphous top cell after degradation, however, strongly decreases with increasing i-layer thickness (Figure 60). Therefore, the top cell fill factor will, after degradation, always be lower than the fill factor of the microcrystalline bottom cell, which is close to 70 % for the I-V curve underlying our model. If the currents are approximately matched after degradation (Figure 64, center), the tandem cell fill factor corresponds to a value in between those of top and bottom cell, where the weight of the top cell FF is stronger due to the higher V_{oc} of the top cell.

Even higher tandem cell FF values can be obtained if a strong current mismatch between the component cells is prevailing. High tandem cell fill factors are obtained when the top cell strongly limits the current. In this case, the tandem cell I-V curve is basically given by the top cell I-V curve, shifted to the right by the value of V_{oc} of the bottom cell (Figure 64, left), resulting in considerable FF improvement compared to the top cell. Increasing the top cell current, the bottom cell limits the tandem cell current and the fill factor increases again (Figure 64, right).

We have seen that quite high FF values can be obtained in the light-soaked state due to the "tandem effect" on the I-V curve. However, in order to optimize the electrical output power of the tandem cell, maximizing the fill factor is not a sufficient criterion. E.g., in Figure 64, the output power (surface of the shaded rectangle) is lowest for the case of strong bottom limitation (right), for which case we observe, however, the highest fill factor. In the present realistic example the top limited and equilibrated case have quite similar output power. This is due to the fact that the fill factor is quite low (51 %) for a top cell reaching current equilibration whereas the fill factor of a top cell which strongly limits the current is relatively high (66 %). If current equilibration could be achieved within a top cell with a higher fill factor, output power would be maximum close to current matching, yet the fill

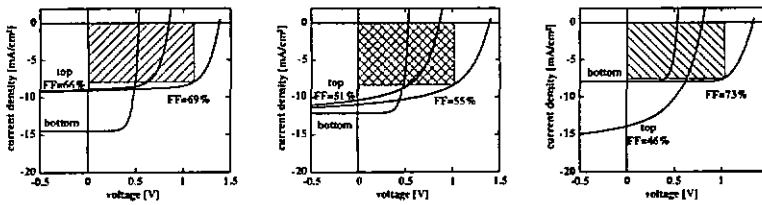

Figure 64: Component cell I-V curves and resulting tandem cell output for the case of extreme top limitation, a situation close to current matching and extreme bottom limitation (from left to right). Bottom cell fill factor is 70 % in all cases.

factor would still remain lower than in both cases with strong current mismatch.

Tandem cell efficiency and experimental values

For any current density of the top cell, the tandem cell efficiency increases with increasing top cell fill factor as can be easily understood (Figure 63). For a given top cell fill factor, the tandem cell efficiency first increases with increasing top cell current, reaches a maximum and decreases again for even higher current generation in the top cell. The decrease for high top cell currents is again caused by the decrease of the tandem cell current due to limitation by the bottom cell. It is, however, interesting to note that maximum tandem cell efficiency is obtained for top cell currents that are higher than those yielding maximum tandem cell current. In fact, a slight limitation of the current by the bottom cell yields an improved overall fill factor, as can be seen in Figure 63, bottom.

Data points and lines on the efficiency map (Figure 65) indicate experimentally obtained trajectories FF(I), i.e. current – fill factor pairs for amorphous top cells in the light-soaked state. Values for the current density correspond to those obtained for cells on CVD-ZnO and with a thick n^+-layer which avoids current enhancement due to reflection at the back contact

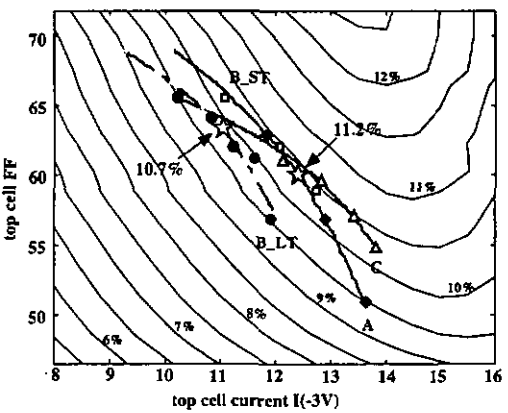

Figure 65: Modeled efficiency for micromorph tandem cells as shown in Figure 63. Trajectories in the efficiency-map correspond to experimentally obtained values for four different types of top cells, series B_LT (low-temperature H_2 diluted ●), B_ST (standard temperature H_2 diluted □), A ("standard" p/b-i-n ♦) and C (high-T_s Δ) of Table 9. Stars indicate the approximate location of experimentally obtained micromorph tandem cells.

(Figure 59). Fill factors have been measured on single-junction cells of varying i-layer thickness, deposited on Asahi U-type TCO, in the light-soaked state. Each of those trajectories corresponds to one of four types of top cells (see Table 9, page 102). The general behavior is the same for all deposition techniques: increasing top cell thickness results in enhanced current density but also lower FF values after degradation. Starting at thin top cell i-layers (high degraded fill factor, low current), the trajectories first lead "uphill": the top cell current increases and at the same time the degraded fill factor decreases. In the tandem cell, however, the gain due to the current increase is more important than the reduction of the top cell fill factor, leading to a net increase in tandem cell efficiency. At a certain point, the trajectories turn parallel to the "iso-efficiency" curves, i.e. the tandem cell efficiency remains constant. Current increase and FF decrease with increasing thickness compensate each other. Even thicker i-layers in the top cell lead again "downhill": the tandem cell efficiency decreases as the top cell fill factor decreases and the cell currents move towards equilibration.

One has to keep in mind that the efficiency map is calculated for a top cell V_{oc} of 0.85 V when comparing efficiencies for the trajectories of different deposition techniques in Figure 65. According to Equation 19, tandem cell efficiencies can be corrected for top cell V_{oc} as indicated in Table 10.

series	V_{oc} [V]	efficiency correction
B_LT	0.89	+ 2.9 % rel.
B_ST	0.87	+ 1.4 % rel.
A	0.84	- 0.7 % rel.
C	0.78	- 5.1 % rel.

Table 10: Correction of modeled tandem cell efficiencies for top cell $V_{oc} \neq 0.85$ V.

The maximum of ~10 % efficiency for series B_LT corresponds therefore to a corrected value of ~10.3 %, corrected maxima for series A and B_ST are 10.4 % and 10.6 %, respectively, and the corrected value for the maximum of series C (10.5 %) is ~10 %. Those values are quite close to experimentally achieved tandem cell efficiencies in the light-soaked state with such amorphous top cells. The value of 10.4 % with low-temperature H_2 diluted top cells is close to an experimentally obtained value of 10.7 % for a micromorph tandem cell in the light-soaked state, as measured by an independent laboratory. 11.2 % stabilized efficiency has been measured on a tandem cell with an amorphous top cell of type "A" [134]. The approximate location of these two data points is marked with stars in Figure 65.

None of the four deposition techniques clearly results in considerably higher efficiency values in a tandem cell than the others. Cells deposited with H_2 dilution at standard temperature (series B_ST) have, however, the highest efficiency potential of ~10.6 %

(corrected for V_{oc}). Top cells deposited at enhanced temperature are interesting due to their considerably higher current level. Lower FF values and low V_{oc} values compared to the other cells, however, overcompensate the gain in current so far.

The main conclusion from Figure 65 is the observation that currently available amorphous top cells are not suited to yield micromorph tandem cells with efficiencies exceeding ~11 %. Values as high as 12.5-13 % are theoretically possible. For such tandem cells, the current generation in the amorphous top cell would have to be of the order of 13-14 mA/cm^2, while at the same time a fill factor of the top cell in the light-soaked state of around 70 % is needed. Both conditions can be fulfilled separately. High stabilized fill factors are achievable for thin solar cells with H_2 diluted i-layer. On the other hand, current densities exceeding 13 mA/cm^2 are achievable for solar cells containing i-layers deposited without H_2 dilution and/or at enhanced substrate temperature (Figure 59, series A and C). However, when the i-layer thickness is chosen to yield a current density of 13 mA/cm^2, fill factor values in the light-soaked state are on the order of 55 %.

Finally, let us point out that a major restriction for the tandem cell efficiency is the series connection and the resulting current matching issue. Ma et al. [138] achieve by using a 4-terminal a-Si:H/poly-Si structure an efficiency of 21 % (a-Si:H top cell undegraded). Using our experimental data for top and bottom cell we can estimate an efficiency for a 4-terminal device using our cell data as top: 10.5 mA/cm^2·0.69·0.9 V = 6.52 mW/cm^2 and bottom: (26-10.5) mA/cm^2·0.7·0.53 V = 5.75 mW/cm^2, which adds to an efficiency of 12.3 %. Taking a total current density of 40 mA/cm^2 as in ref. 138 (300 µm poly-Si), our bottom cell would yield (40-10.5) mA/cm^2·0.7·0.53 V = 10.94 mW/cm^2, i.e. 17.5 % in the tandem. The remaining difference to 21 % is explained by the higher bottom cell V_{oc} and FF (0.58 V, 79 %) in ref. 138.

Goals for a-Si:H top cells

Different means are imaginable in order to increase the stabilized efficiency of micromorph tandem cells beyond a value of ~11 %. If research on a-Si:H could provide intrinsic material of good quality but with considerably reduced optical gap, the amorphous top cell could provide a high current density within a relatively thin i-layer and therefore a good fill factor in the light-soaked state (horizontal move to the right in Figure 65). This requires that this hypothetical material would have to be grown under conditions which are suited for solar cell production, i.e. especially moderate substrate temperatures. The high-T_s intrinsic material investigated here (section II.2.2.3) points into the right direction, however technological problems connected with the cell fabrication restrict the utility of this material for micromorph tandem cells so far. Intrinsic material with strongly reduced light-induced degradation also could contribute to higher stabilized tandem cell efficiencies resulting from

higher stabilized FF values. Such material would result in higher stabilized FF values. If this can be obtained without loss in optical absorption, one would vertically move upwards in Figure 65, which means an increase in stabilized tandem cell efficiency. Unfortunately, the considerable gain in stabilized $\mu_0\tau_0$ product by employing the H_2 dilution technique (section 0) has to be paid for with reduced optical absorption. Thereby the beneficial effect is annihilated, as shows the comparison between the trajectories for series A and B_ST in Figure 65.

A possible approach to increase the current generation within a given i-layer thickness while using existing a-Si:H materials consists of inserting a selectively reflecting ZnO interface layer in between top and bottom cell [145]. Assuming that the enhanced illumination of the top cell results in negligible additional degradation, this measure would result in a horizontal move of the experimental trajectories to the right in Figure 65 and therefore enhanced stabilized efficiency. It has to be taken into account, however, that the bottom cell current decreases by at least the same amount as the top cell current increases, and additional optical losses may occur. This approach has been studied theoretically in ref. 139.

Based on the results presented above, we will discuss below directions of further research with respect to their potential to enhance the stabilized efficiency of micromorph tandem cells.

IV.3.4.2. Future developments

Enhanced total current density

Thin-film silicon solar cells are reported to have a current potential approaching 30 mA/cm^2 [146]. An increase in the totally available current density due to optimization of light-trapping or by enhancing the absorption seems indeed within possibilities for micromorph solar cells. We therefore investigated the efficiency potential of micromorph tandem cells with such enhanced total current density. Figure 66 illustrates the modeled tandem cell efficiency map as a function of top cell fill factor and current density for a total current density of 30 mA/cm^2. The only difference compared to Figure 63 is the total current density raised by 4 mA/cm^2. The maximum tandem cell efficiency is clearly increased to over 14 %. This modeled efficiency, however, would only be obtained for a top cell providing >15 mA/cm^2 with a fill factor of around 70 %, which is definitely not achievable today. Efficiencies along the experimental top cell trajectories are slightly enhanced compared to the situation for a total current density of 26 mA/cm^2; the gain is on the order of 0.5 % absolute. This is because of improved tandem cell fill factors due to a higher degree of current mismatch for experimentally available top cells.

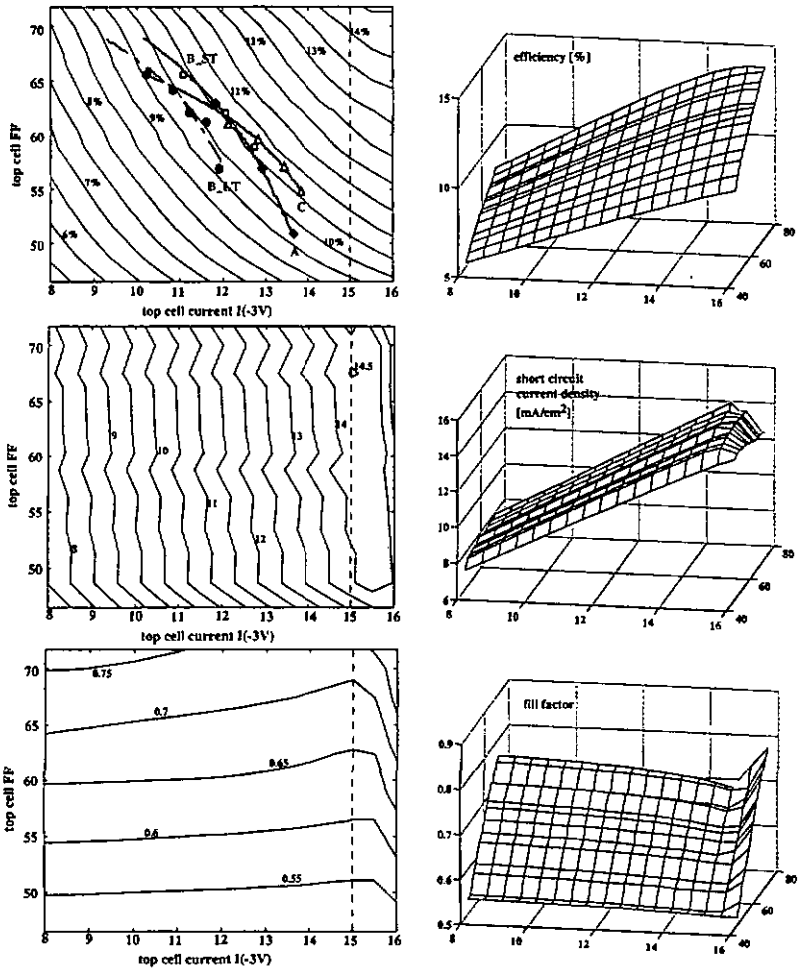

Figure 66: Modeled efficiency, FF and short circuit current density for micromorph tandem cells as a function of the FF and current level I(-3 V) of the amorphous top cell. Total current density (sum of top and bottom cell currents) is 30 mA/cm². V_{oc} of the top cell is 0.85 V, the bottom cell characteristics are as described in the text. Trajectories in the efficiency-map correspond to experimentally obtained values for four different top cell deposition techniques, series B_LT (low-temperature H_2 diluted ●), B_ST (standard temperature H_2 diluted □), A ("standard" p/b-i-n ♦) and C (high-T_s Δ) of Table 9.

An increase in the totally available current density therefore does not considerably improve the stabilized efficiency of micromorph tandem cells as long as the problem of the current generation / stability of the top cell is not resolved satisfactorily.

a-Si:H/μc-Si:H/μc-Si:H triple cells

We have seen above that the basic problem of the micromorph tandem cell is the generation of a high current density within an amorphous top cell without back reflector. This cell furthermore needs a high stabilized fill factor. As such an ideal top cell is not available with current a-Si:H technology, it is worthwile to study the triple cell approach, i.e. the distribution of the total current density into three component cells. An a-Si:H solar cell as the middle cell can directly be ruled out; already a total current density of 24 mA/cm^2 would require at least 16 mA/cm^2 in the both amorphous cells (meaning 8 mA/cm^2 to flow through both cells). It has been shown in section IV.2.3 that such a value is available with a-Si:H as the absorbing layer only when a highly reflective back contact is applied. a-SiGe:H alloys could principally provide enough current in a middle cell. This solution requires, however, the availability of amorphous silicon germanium alloy technology, which is somehow incoherent with the use of μc-Si:H as low-gap material.

The approach to use a microcrystalline solar cell also as a middle cell in a triple stacked cell has first been proposed by Fischer et al. [145], and implemented by Yamamoto et al. [137], leading to a stabilized efficiency of 11.5 %. We used our semi-empirical model to investigate the efficiency potential of such a triple stacked cell. The middle and bottom cell were represented for modeling by a μc-Si:H solar cell with doubled V_{oc}, the current was taken as $(I_{total}-I_{top})/2$. This approach presumes that both, middle and bottom cell, have similar V_{oc} and FF values. Figure 67 shows the modeled efficiency map, together with tandem cell fill factor and I_{sc} for this case of a "micro^{2}morph" (a-Si:H/μc-Si:H/μc-Si:H) triple cell and a total current density of 26 mA/cm^2. In this case we observe the maximum in the efficiency for top cell current densities of around 9 mA/cm^2. The theoretically achievable maximum efficiency is on the order of 11.5-12 %. This is slightly lower than what is theoretically conceivable for a double-stacked tandem cell with 26 mA/cm^2 total current density (~12.5 %, Figure 63).

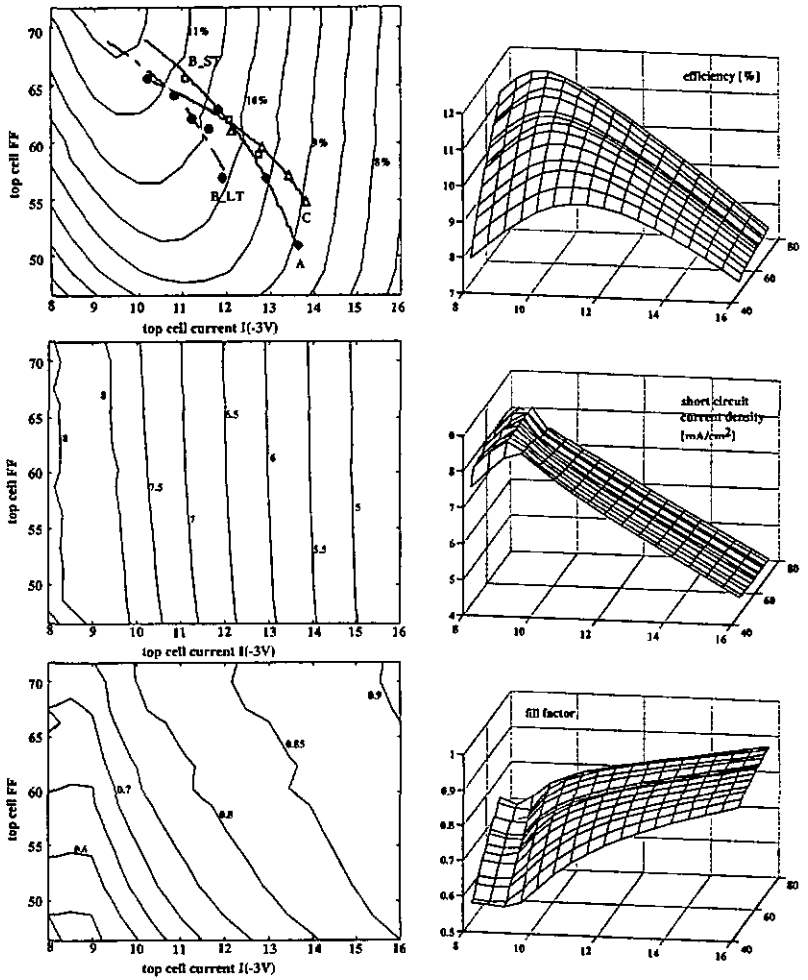

Figure 67: Modeled efficiency, FF and short circuit current density for micramorph triple (a-Si:H/μc-Si:H/μc-Si:H) cells as a function of the FF and current level I(-3 V) of the amorphous top cell. Total current density (sum of top, middle and bottom cell currents) is 26 mA/cm². V_{oc} of the top cell is 0.85 V, the middle and bottom cell characteristics are identical and as described in the text. Trajectories in the efficiency-map correspond to experimentally obtained values for four different top cell deposition techniques B_LT (low-temperature H_2 diluted ●), B_ST (standard temperature H_2 diluted □), A ("standard" p/b-i-n ♦) and C (high-T_s Δ) of Table 9.

In contrast to the theoretical maximum for the double stacked cell, the maximum efficiency for the triple stacked cell is obtained for current and fill factor values of the top cell which are within the experimentally attainable range. In fact, the experimental FF(I) trajectories of the top cells are, for all four deposition techniques, directed towards this efficiency maximum (Figure 67). In other words, reducing the thickness of the amorphous top cell, one moves on the FF(I) trajectory towards the maximum of tandem cell efficiency. An amorphous top cell providing a current density of 9 mA/cm^2 can, in fact, be very thin and therefore highly stable. Furthermore, in this case the enhanced optical gap of i-layer material deposited with H_2 dilution is no longer a limit for this deposition technique. Therefore one can take full advantage of the enhanced stability and at the same time high and stable V_{oc} values of low-temperature H_2 diluted cells (series B_LT). The i-layer thickness for such a top cell would have to be on the order of only 100 nm in order to generate a sufficient amount of current.

Using this triple stacked cell approach, the balance of energy generation is shifted in

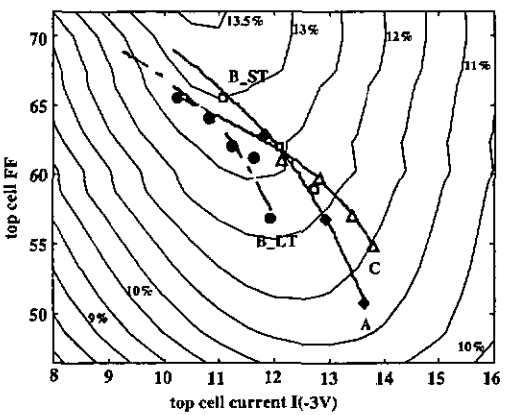

Figure 68: Modeled efficiency, FF and short circuit current density for micromorph triple (a-Si:H/μc-Si:H/μc-Si:H) cells as a function of the FF and current level I(-3 V) of the amorphous top cell. Total current density (sum of top, middle and bottom cell currents) is 30 mA/cm^2. V_{oc} of the top cell is 0.85 V, the middle and bottom cell characteristics are identical and as described in the text. Trajectories in the efficiency-map correspond to experimentally obtained values for four different types of top cells B_LT (low-temperature H_2 diluted ●), B_ST (standard temperature H_2 diluted □), A ("standard" p/b-i-n ♦) and C (high-T, Δ) of Table 9.

favor of the microcrystalline part. In a conventional double stacked cell roughly 2/3 of the energy are generated in the top and 1/3 in the bottom cell. Assuming V_{oc} values of 0.9 V for the top and 0.53 V for both, middle and bottom cell of a triple stack, 46 % (0.9/(0.9+2·0.53)) of the energy is generated in the top cell and 54 % (2·0.53/(0.9+2·0.53)) in middle and bottom cell together. This means, in its turn, that the V_{oc} of the microcrystalline component cells becomes a very decisive parameter for optimizing the efficiency of such triple stacked cells.

A further advantage of the triple stacked cell is the reduced series resistance problem. The generated power is shifted towards higher voltages and smaller currents; the current density is reduced by a factor of $^2/_3$, according to the distribution of the total current density in three instead of two component cells.

The disadvantage of this triple cell approach consists in a more complicated cell structure. Two more doped layers are needed, which increases the process time slightly. Let us emphasize, however, that the total microcrystalline i-layer thickness remains the same - for a given total cell current density - as for a micromorph tandem cell. The total i-layer thickness is only separated into two component cells.

A first such a-Si:H/μc-Si:H/μc-Si:H "micro^{2}morph" triple cell deposited at IMT exhibits the following characteristics: V_{oc} = 1.75 V, FF = 70 %, I_{sc} = 5.13mA/cm^2. The efficiency is limited by the unsatisfying current matching: even though the sum of all three component currents exceeds 22 mA/cm^2, the bottom cell strongly limits the current.

Modeling the "micro^{2}morph" triple cell for a total current potential of 30 mA/cm^2 (Figure 68) one obtains maximum efficiencies as high as 13.5 %. Stabilized efficiency exceeding 13 % is within possibilities for amorphous top cells as available today. The following Table 11 summarizes the different approaches for micromorph tandem and triple cells together with their efficiency potential according to our semi-empirical model.

	efficiency potential	max. efficiency with today's top cells
tandem 26 mA/cm^2	12.5 %	10.5-11 %
tandem 30 mA/cm^2	14.5 %	10.5-11 %
triple 26 mA/cm^2	11.5 %	~11.5 %
triple 30 mA/cm^2	13.5 %	13-13.5 %

Table 11: Efficiency potential and efficiency achievable with today's top cells according to our semi-empirical modeling for micromorph tandem and triple cells with varying total total current potential.

Other directions of future research

The direction of basic material research has, in consequence to the observations made above for the micromorph tandem cell, to be directed towards the development of intrinsic a-Si:H with improved stability, similar to what is obtained for the H_2 dilution technique, yet without the increase in the optical gap. Figure 69 illustrates the influence of H_2 dilution and substrate temperature on the quality of the material in the light-soaked state. The layout of the plot, with the stabilized $\mu_0\tau_0$ product on the abszissa and the absorption coefficient on the ordinate, is similar to the efficiency map in Figure 63, where the tandem cell efficiency is plotted as a function of fill factor and current density in the top cell.

Any method to increase the current generation in the amorphous top cell bears potential to increase the stabilized efficiency of a micromorph tandem cell. Such methods include the insertion of a ZnO selectively reflecting interface layer between the top and bottom cell. It has been theoretically [147] and experimentally [148] shown that such an intermediate reflector layer can increase the current generation within a given top cell thickness by roughly 2 mA/cm^2. Assuming a negligible influence of this selective mirror on the degraded fill factor of the top cell, this would result in a horizontal shift to the right by 1 mA/cm^2 of the experimental FF(I) trajectories in Figure 63.

Ameliorated light-trapping mechanisms also can contribute to enhanced current generation in the amorphous top cell. The texture and transparency of the front TCO is of

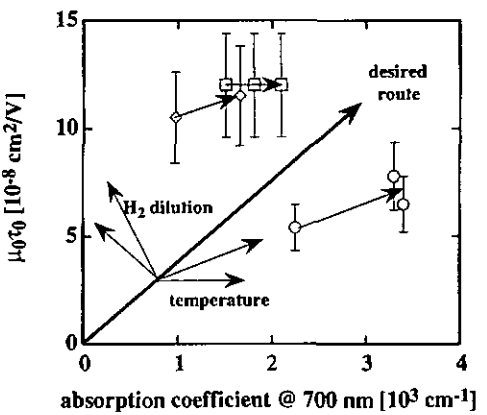

Figure 69: Illustration of the relationship between stabilized $\mu_0\tau_0$ and the absorption coefficient @ 700 nm for intrinsic films deposited at various substrate temperatures and H_2 dilution ratios.

crucial importance. Our CVD-deposited ZnO already results in current densities that are higher than those obtained for an identical solar cell deposited on Asahi U-type SnO_2. Further improvement by fine-tuning the texture of the TCO surface should result in additional improvement. Furthermore, antireflective coating on top of the front glass has the potential to slightly enhance the current density within the solar cell by reducing reflection losses at the air-glass interface.

Deposition of the entire solar cell stack in the "inverted" structure, i.e. deposition sequence n-i-p on top of a non-transparent substrate also bears potential for a further efficiency improvement, for several reasons. First, solar cells in the n-i-p deposition sequence generally have higher V_{oc} values than cells deposited under comparable conditions in the p-i-n structure. The n-i-p structure has the further advantage that the p-i-interface is not directly affected by the substrate temperature during i-layer deposition. Technological problems with solar cells where the i-layer is deposited at enhanced temperature in order to reduce its optical gap might therefore be reduced [149]. Such inverted solar cells have not been developed in the framework of this work, they might, however, be an interesting starting point for further optimization of micromorph tandem cells.

IV.3.4.3. Experimental results for micromorph tandem cells

Table 12 contains experimental values for micromorph tandem cells in the light-soaked state. Efficiency values correlate quite well with values obtained by semi-empirical modeling, as described above. V_{oc} is higher for the LT H_2 diluted top cell, the current density, in contrast, is higher for the standard top cell with undiluted i-layer. The efficiency values of 10.7 % and 11.2 %, respectively, are not too far from the values obtained in Figure 63. The higher efficiency for the tandem cell containing a "standard" top cell is caused by the higher short circuit current density.

type top cell	V_{oc} [V]	I_{sc} [mA/cm^2]	FF [%]	efficiency [%]
LT H_2 diluted	1.34	11.9	67	10.7
standard	1.28	13	67	11.2

Table 12: Experimental performance data for micromorph tandem cells with different top cells in the light-soaked state.

IV.3.5. Conclusions

Confirming the data obtained for the optical gap of intrinsic layers and currents in single-junction solar cells, we observe pronouncedly different current potential for different top cell deposition techniques. Amorphous top cells deposited at enhanced substrate temperature result in 6-8 % higher current density in a top cell compared to standard undiluted cells; low

temperature cells deposited with H_2 dilution result in a current loss of 5-9 % compared to standard cells. The loss increases in both cases with increasing i-layer thickness. Therefore, the difference in current level in the amorphous top cell can be as pronounced as 17 %, comparing high-T_s solar cells to LT H_2 diluted cells for thick i-layers.

Our simple semi-empirical model allows us to estimate the efficiency potential for different types of micromorph tandem cells. Assuming a total current potential of 26 mA/cm^2 we observe as upper limit for the tandem cell efficiency in the light-soaked state a value of 12-13 %. However, this potential can not be fully used with currently available amorphous top cells. The required high current density exceeding 13 mA/cm^2 and at the same time a stabilized FF close to 70 % can not be obtained in today's amorphous top cells.

The general goal of future work on amorphous top cells therefore has to be the enbancement of the current generation in the top cell and / or enhanced stability of the amorphous top cell. Interesting approaches in this context comprise enhanced light-trapping or ZnO intermediate reflector layers. An antireflective coating would enhance the current density in both, the top and bottom cell. Deposition of the top i-layer at enhanced temperature has been shown to yield considerably enbanced current values, however the corresponding cell technology still needs further improvement. Development of solar cells in the inverted n-i-p structure might be a promising way to overcome technological problems.

Taking into account the technological problems connected to generating a high current density in the amorphous top cell and maintaining at the same time good stability, the "micro^{2}morph" triple cell is a noteworthy alternative. In this case, the amorphous top cell again can be thin and therefore relatively stable. Furthermore the H_2 dilution technique can be employed, leading to enhanced stability and higher V_{oc} values for the top cell.

Stabilized efficiencies of 10.7 % and 11.2 % have been demonstrated in micromorph two-stacked tandem cells and employing amorphous top cells which have been optimized in the context of this work.

V. General conclusions

The goal of the present work was the enhancement of the stabilized efficiency of a-Si:H based thin film solar cells. This goal has been addressed using two main approaches. On the one hand, the deposition of intrinsic a-Si:H has been optimized with respect to stability against light soaking. On the other hand, questions concerning the solar cell design, such as optimization of the i-layer thickness, optical gap of the i-layer, interface layers etc., have been addressed.

- ***Optimization of intrinsic a-Si:H deposition***

H_2 dilution of the process gas improves the stability of the resulting a-Si:H material against light-induced degradation. The $\mu_0\tau_0$ product in the light-soaked state is enhanced by a factor of two compared to standard material deposited without H_2 dilution. The optical bandgap increases and the hydrogen content of the material decreases as the H_2 dilution ratio is increased.

A comparison of VHF, RF and DC plasma excitation shows the properties of material deposited without H_2 dilution at standard temperature of ~200°C to be almost equal for all three deposition techniques. A variation of the deposition temperature has the same effect in all three cases: increasing the temperature results in a decrease in the hydrogen content and the optical bandgap of the a-Si:H films. Material deposited at higher than standard substrate temperature exhibits improved stability against light soaking compared to material deposited at standard temperature.

The increased growth rate observed for the VHF technique, compared to conventional RF deposition, has always been one of the principal motivations for its investigation in the context of a-Si:H deposition. The direct comparison of VHF, RF and DC excitation shows that material of almost identical quality can be deposited with all three techniques. Therefore, the growth rate becomes the most important criterion for the choice of a plasma excitation frequency. The growth rate of a-Si:H films deposited with H_2 dilution is 4-8 times higher for VHF than for conventional RF excitation, whereas DC deposition yields growth rates close to those of the VHF technique. It is therefore certainly not astonishing that the interest in the VHF technique for a-Si:H deposition is booming lately, leading to an increasing number of publications where the VHF technique is employed [e.g., 150-158].

- ***Single-junction solar cells***

The use of intrinsic layers deposited using the H_2 dilution technique results in enhanced stability against light soaking. Good correlation between the $\mu_0\tau_0$ product of the intrinsic material and the efficiency of single-junction solar cells is observed. A stabilized efficiency

of 7.5 % for a single-junction cell has been demonstrated. The intrinsic layer of this solar cell is deposited, using VHF excitation, at a growth rate of 4 Å/s with H_2 dilution.

Various contamination sources affect the performance of solar cells when the i-layer is deposited with H_2 dilution. The main contaminants are oxygen, boron and phosphorus. We have studied the influence of these contaminants on the solar cell performance and described technological means to suppress contamination below a critical level.

Besides solar cells deposited with H_2 dilution, we have developed other types of single-junction solar cells for use in tandem and stacked structures. As a result we have a choice of various cell deposition techniques with specific properties.

We could show that the considerably higher growth rates obtained due to the VHF excitation technique do not affect the stability of the solar cells. Stabilized efficiencies that are comparable to values obtained by the conventional RF technique have been demonstrated, confirming a true advantage of the VHF plasma excitation technique.

- ***Stacked solar cells***

We have obtained a stabilized efficiency of 9.0 % for an a-Si:H/a-Si:H stacked cell, as confirmed by an independent laboratory. The cumulative layer deposition time, including i-layers deposited with H_2 dilution, is reduced to 22 min. due to the VHF deposition at high rate. The growth rate for the H_2 diluted i-layer is 4 Å/s.

It has been shown experimentally and by modeling that the exact balance of current matching is a very important parameter for the optimization of the stabilized efficiency. Slightly top-limited conditions result in optimized stacked cell performance after light soaking.

- ***Micromorph tandem cells***

Different types of a-Si:H top cells in micromorph tandem cells have been investigated with respect to their potential to enhance the stabilized efficiency of micromorph tandem cells. Different approaches, including i-layers deposited with H_2 dilution and buffer layers have been studied experimentally and by means of a semi-empirical model.

10.7 % (confirmed by an independent laboratory) and 11.2 % (measured at IMT) stabilized efficiency of micromorph tandem cells have been obtained using amorphous top cells as developed and optimized here.

The efficiency potential for micromorph tandem cells in the degraded state is, based on our semi-empirical model, estimated to be 12-13 %. This value, however, can not be achieved with today's amorphous top cells but requires a-Si:H top cells with considerably higher current generation and better stability than those available today. Future research on a-Si:H materials has to be directed into this direction.

We propose the alternative concept of a "micro^{2}morph" triple cell. Such solar cells have potential for stabilized efficiencies close to 12 %. In contrast to the micromorph tandem cell, the triple cell requires a-Si:H top cells that are available with today's technology.

- *Synthesis*

The following Figure 70 illustrates the solar cell optimization process as described in this work. A combination of intrinsic material optimization and measures that can be subsumed under "cell design" result in a considerable increase in the stabilized solar cell efficiency. Employing H_2 diluted i-layer material with enhanced stability in a 450 nm thick p-i-n cell leads to a stabilized efficiency of ~7.5 %. A comparable cell in the conventional p/b-i-n structure degrades to ~6.5 % after 1000 h. Further enhancement of the stabilized efficiency is possible when an a-Si:H/a-Si:H stacked structure is employed. A stabilized efficiency of 9 % has been obtained in this case. Considerable additional improvement is possible when the same-bandgap stacked structure is replaced by a tandem structure with two pronouncedly different optical bandgaps in the two component cells: micromorph tandem cells have led to stabilized efficiencies well above 10 %.

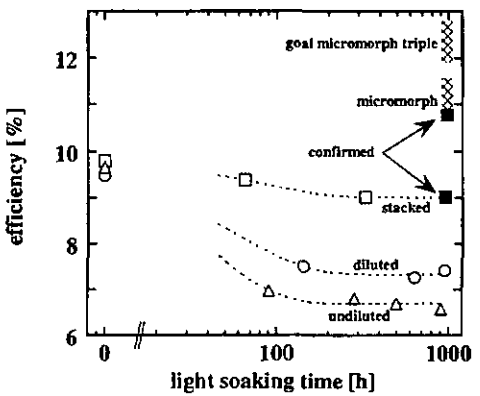

Figure 70: Comparison of the light soaking behavior of an undiluted versus a H_2 diluted single-junction cell and an optimized a-Si:H/a-Si:H stacked cell. Stabilized micromorph tandem efficiencies and the goal range for micromorph triple cells are added.

- *Outlook*

We have found that the efficiency of micromorph tandem cells is largely limited by the amorphous top cell. The search for a-Si:H material with enhanced stability against light-

soaking remains of crucial importance. H_2 dilution has been shown to yield such material with improved stability, however at the expense of reduced light absorption. The challenge for any material study is the combination of enhanced stability and low optical gap of the material.

Finally, given the promising state of research in the laboratory, we believe that now the scale-up to large-area deposition should be undertaken in order to demonstrate the feasability of industrial production.

VI. Annex

VI.1. MatLab program calculating I-V curve of a stacked cell

```
                                        % calculates I-V curve of a tandem cell
clear;
load IVbot;          bottom=IVbot;      % I-V bottom cell
load IVtop;          top=IVtop;         % I-V top cell

ftop = 16;                              % current top cell @ -3V
fbottom = 26 - ftop;                    % current bottom cell @ -3V
utop = 0.9942;                          % correction top cell Voc

ibottom = -fbottom:0.02:0.5;            % ibottom = -fbottom to 0.5 step 0.02
itop = -ftop:0.02:0.5;                  % itop = -ftop to 0.5 step 0.02

bottom(:,2)=bottom(:,2)/bottom(1,2)*fbottom*(-1); % scaling the current values bottom cell
top(:,2)=top(:,2)/top(1,2)*ftop*(-1);   % scaling the current values top cell
top(:,1)=top(:,1)*utop;                 % scaling the voltage top cell

pbottom=bottom(:,1) .* bottom(:,2);
ptop=top(:,1) .* top(:,2);

if ftop <= fbottom                      % current tandem cell = smaller of
        itandem = top(1,2):0.02:0.5;    % the component currents
else
        itandem = bottom(1,2):0.02:0.5;
end;

utandem = spline(top(:,2),top(:,1),itandem)+spline(bottom(:,2),bottom(:,1),itandem);
                        % spline for i(u), top and bottom, add u values for same current
ptandem = utandem .* itandem;

ptandemmax = min(ptandem);
voc = interp1(itandem,utandem,0);
isc = interp1(utandem,itandem,0);
fftandem = ptandemmax/(voc*isc);
```

VI.2. I-V curves for modeling of micromorph tandem cells

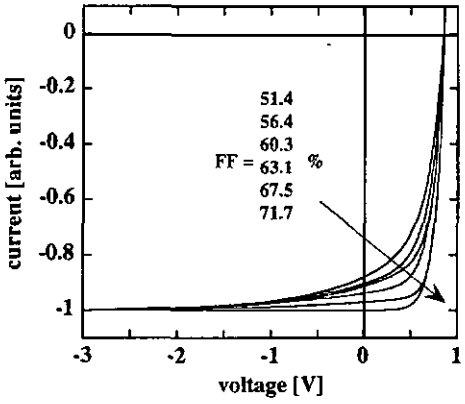

Figure 71: Measured I-V curves of amorphous p-i-n solar cells that have been used for modeling of micromorph tandem cell performance. FF values are given in the figure, voltage and current values have been normalized.

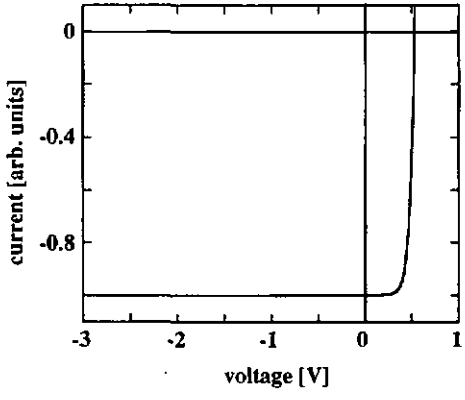

Figure 72: Measured I-V curves of amorphous p-i-n solar cells that have been used for modeling of micromorph tandem cell performance. V_{oc} = 0.53 V, FF = 70 %, the current values have been normalized.

VI.3. Constants, symbols and abbreviations

VI.3.1. Constants

e	Elementary charge, $1.602 \cdot 10^{-19}$ C.
h	Planck's constant,
k_B	Boltzmann's constant,

VI.3.2. Symbols

c_H	Hydrogen content.
D	Carrier diffusion constant.
d	Thickness.
E	Energy.
E_{03}	Optical bandgap, $\alpha(E_{03}) = 10^3$ cm^{-1}.
E_{04}	Optical bandgap, $\alpha(E_{04}) = 10^4$ cm^{-1}.
E_{act}	Dark-conductivity thermal activation energy.
E_F	Fermi energy.
E_g	Optical bandgap.
E_{Tauc}	Optical bandgap energy after Tauc; intersection of the $(\alpha E)^{1/2}(E)$ curve with abscissa.
E_U	Urbach energy = slope of the valence band tail.
F	Electric field.
G	Generation rate.
i	Current density.
I	Current.
I_0	Reverse saturation current.
I_{bottom}	Bottom cell current density.
I_{light}	Light intensity.
I_m	Current at maximum power point.
I_{sc}	Short circuit current density.
I_{top}	Top cell current density.
I_{total}	Sum of top and bottom cell current density.
L_{diff}	Carrier diffusion length.
L_{drift}	Carrier drift length.
n	Density of free electrons.
p	Density of free holes.
R	Microstructure factor.
R	Optical reflection.
S	Capture cross section.
T	Optical transmission.
T	Temperature.
T_s	Substrate temperature.
V	Voltage.
V_{bi}	Built-in voltage.
V_m	Voltage at maximum power point.
V_{oc}	Open circuit voltage.
α	Optical absorption coefficient.
η	Solar cell efficiency.

κ	Factor relating i-layer thickness and drift length.
λ	Wavelength.
μ	Carrier mobility.
$\mu_0\tau_0$	Mobility lifetime product.
μ_n	Effective electron mobility.
μ_p	Effective hole mobility.
ν	Light frequency.
σ_d	Dark-conductivity.
σ_{ph}	Photo-conductivity.
τ	Carrier liftetime.
τ_n	Electron liftetime.
τ_p	Hole liftetime.
ω	Frequency of IR light.

VI.3.3. Abbreviations

AM 1.5	"Air mass 1.5"; energy distribution of the sunlight after 1.5 passes through the earth's atmosphere, corresponding to an angle of incidence of ~60°.
a-Si:H	Amorphous hydrogenated silicon.
a-SiC:H	Amorphous hydrogenated silicon carbon.
a-SiGe:H	Amorphous hydrogenated silicon germanium.
B_2H_6	Diborane.
C_2H_4	Ethylene.
C_2H_6	Acetylene.
CH_4	Methane.
CO_2	Carbon dioxide.
CPM	Constant photocurrent method.
c-Si	Crystalline silicon.
CVD	Chemical vapor deposition.
DC	Direct current.
FF	Fill factor.
FTIR	Fourier transform infrared (spectroscopy).
GD	Glow discharge.
H_2	Hydrogen.
HW	Hot wire.
IL	Interface layer.
IR	Infrared.
ITO	Indium tin oxide, material used as transparent conductive oxide.
KOH	Kalium hydroxide.
PDS	Photothermal deflection spectroscopy.
PECVD	Plasma enhanced chemical vapor deposition.
PH_3	Phosphine.
PV	Photovoltaic.
RF	Radio frequency (here: 13.56 MHz).
sccm	Standard cubic centimeter (1 cm^3 gas at atmospheric pressure).
SiH_4	Silane.
SIMS	Secondary ion mass spectroscopy.
SnO_2	Tin oxide; material used as transparent conductive oxide.
SR	Spectral response.
TCO	Transparent conductive oxide.

VHF	Very high frequency (~40-130 MHz, here usually 70 MHz).
XPS	X-ray photoelectron spectroscopy.
ZnO	Zinc oxide, material used as transparent conductive oxide.
μc-Si:H	Microcrystalline hydrogenated silicon.

VI.4. Further publications

R. Platz and G. Dodel:
"Frequenzverschiebung von Ferninfrarot (FIR) strahlung im Megahertzbereich zur Anwendung bei der Heterodyninterferometrie und der Laserlichtstreuung mit Heterodynnachweis"
Spring meeting of the German Physical Society, March 9-11, 1993, Greifswald (D).

R. Platz, R. Brüggemann and G.H. Bauer:
"More insights from simulation for the interpretation of the constant photocurrent method"
Journal of Non-Crystalline Solids 164-166 (1993) 355.

R. Platz, D. Fischer and A. Shah:
"VHF-deposited a-SiC:H alloys for high-bandgap solar cells: combining high Voc and reasonable stability"
in: Amorphous Silicon Technology – 1995, ed. by M. Hack, E.A. Schiff, A. Madan, M. Powell, A. Matsuda (Materials Research Society Proceedings 377, Pittsburgh, PA 1995) p.645.

R. Platz, D. Fischer, C. Hof, S. Dubail, J. Meier, U. Kroll and A. Shah:
"H2-dilution vs. buffer layers for increased Voc"
in: Amorphous Silicon Technology – 1996, ed. by M. Hack, E.A. Schiff, S. Wagner, R. Schropp, A. Matsuda (Materials Research Society Proceedings 420, Pittsburgh, PA 1996) p.51.

R. Platz, D. Fischer, S. Dubail and A. Shah:
"a-Si:H/a-Si:H stacked cell with 9% stabilised efficiency deposited in a single-chamber reactor at high rate due to VHF-GD"
Proceedings 14th European Solar Energy Conference (1997) 636.

R. Platz, D. Fischer, S. Dubail and A. Shah:
"a-Si:H/a-Si:H stacked cell from VHF-deposition in a single-chamber reactor with 9% stabilized efficiency"
Solar Energy Materials and Solar Cells 46 (1997) 157.

R. Platz, J. Meier, D. Fischer, S. Dubail and A. Shah:
"The problem of the top cell for the micromorph tandem"
in: Amorphous and Microcrystalline Silicon Technology – 1997, ed. by S. Wagner, M. Hack, E.A. Schiff, R. Schropp, I. Shimizu (Materials Research Society Proceedings 467, Pittsburgh, PA 1997) p.699.

R. Platz, D. Fischer, M.-A. Zufferey, J.A. Anna Selvan, A. Haller and A. Shah:
"Hybrid collectors using thin-film technology"
Proceedings 26th IEEE Photovoltaic Specialists Conference (1997) 1293.

R. Platz, N. Pellaton Vaucher, D. Fischer, J. Meier and A. Shah:
"Improved Micromorph tandem cell performance through enhanced top cell currents"
Proceedings 26th IEEE Photovoltaic Specialists Conference (1997) 691.

R. Platz, C. Hof, B. Rech, S. Wieder, A. Payne, S. Wagner, D. Fischer, A. Shah:
"Comparison of VHF, RF and DC plasma excitation for a-Si:H deposition with hydrogen dilution"
in: Amorphous and Microcrystalline Silicon Technology – 1998, ed. by H. Branz, M. Hack, R. Schropp, I. Shimizu, S. Wagner (Materials Research Society Proceedings 507, Pittsburgh, PA 1998), in print.

R. Platz, C. Hof, D. Fischer, J. Meier and A. Shah:
"High-Ts amorphous top cells for increased top cell currents in micromorph tandem cells"
Solar Energy Materials and Solar Cells 53 (1998) 1.

R. Platz, S. Wagner, C. Hof, S. Wieder, B. Rech:
"On the choice of excitation frequency for plasma-enhanced CVD of amorphous and microcrystalline silicon"
40th Electronic Materials Conference, June 24-26, 1998, Charlottesville, VA.

R. Platz, S. Wagner, C. Hof, A. Shah, S. Wieder, B. Rech:
"Influence of excitation frequency, temperature and hydrogen dilution on the stability of PECVD-deposited a-Si:H"
Journal of Applied Physics 84 (1998) 3949.

R. Platz and S. Wagner:
"Intrinsic microcrystalline silicon by plasma-enhanced chemical vapor deposition from chlorine-containing source gas"
Journal of Vacuum Science and Technology A 16 (1998) 3218.

R. Platz and S. Wagner:
"Intrinsic microcrystalline silicon by plasma-enhanced chemical vapor deposition from dichlorosilane"
Applied Physics Letters 73 (1998) 1236.

A. Allmendinger, R. Platz and G. Dodel:
"Megahertz far-infrared frequency shifting via multiple diffraction by a rotating grating"
Review of Scientific Instruments 64 (7) (1993) 1705.

A. Shah, R. Platz and H. Keppner:
"Thin-film silicon solar cells: a review and selected trends"
Solar Energy Materials and Solar Cells 38 (1995) 501.

J. Meier, S. Dubail, D. Fischer, J.A. Anna Selvan, N. Pellaton Vaucher, R. Platz, C. Hof, R. Flückiger, U. Kroll, N. Wyrsch, P. Torres, H. Keppner, A. Shah, K.-D. Ufert:
"The 'micromorph' solar cells: a new way to high efficiency thin film silicon solar cells"
Proceedings 13th European Solar Energy Conference (1995) 1445.

A. Shah, J. Hubin, R. Platz, M. Goerlitzer and N. Wyrsch:
"The quasineutrality condition in amorphous semiconductors: reformulation of the 'lifetime/relaxation' criterion"
Journal of Non-Crystalline Solids 198-200 (1996) 548.

D. Fischer, S. Dubail, J.A. Anna Selvan, N. Pellaton Vaucher, R. Platz, C. Hof, U. Kroll, J. Meier, P. Torres, H. Keppner, N. Wyrsch, M. Goetz, A. Shah, K.-D. Ufert:
"The 'micromorph' solar cell: extending a-Si:H technology towards thin film crystalline silicon"
Proceedings 25th IEEE Photovoltaic Specialists Conference (1996) 1053.

H. Keppner, U. Kroll, P. Torres, J. Meier, R. Platz, D. Fischer, N. Beck, S. Dubail, J.A. Anna Selvan, N. Pellaton Vaucher, M. Goerlitzer, Y. Ziegler, R. Tscharner, C. Hof, M. Goetz, P. Pernet, N. Wyrsch, J. Vuille, J. Cuperus, A. Shah, J. Pohl:
"The 'micromorph' cell: a new way to high-efficiency low-temperature crystalline silicon thin-film cell manufacturing?"
AIP Conference Proceedings 394 (1996) 271.

J. Meier, P. Torres, R. Platz, S. Dubail, U. Kroll, J.A. Anna Selvan, N. Pellaton Vaucher, C. Hof, D. Fischer, H. Keppner, A. Shah:
"Intrinsic microcrystalline silicon material (μc-Si:H) for thin-film solar cells"
Technical Digest of the 10th "Sunshine" Workshop on Thin Film Solar Cells (1996) 9.

J. Meier, P. Torres, R. Platz, S. Dubail, U. Kroll, J.A. Anna Selvan, N. Pellaton Vaucher, C. Hof, D. Fischer, H. Keppner, A. Shah, K.-D. Ufert, P. Giannoulès, J. Köhler:
"On the way towards high efficiency thin film silicon solar cells by the 'micromorph' concept"
in: Amorphous Silicon Technology – 1996, ed. by M. Hack, E.A. Schiff, S. Wagner, R. Schropp, A. Matsuda (Materials Research Society Proceedings 420, Pittsburgh, PA 1996) p.3.

H. Keppner, P. Torres, J. Meier, R. Platz, D. Fischer, U. Kroll, N. Beck, S. Dubail, J.A. Anna Selvan, N. Pellaton Vaucher, M. Goerlitzer, Y. Ziegler, R. Tscharner, C. Hof, M. Goetz, P. Pernet, N. Wyrsch, J. Vuille, J. Cuperus, A. Shah, J. Pohl:
"The 'micromorph' cell: a new way to high-efficiency low-temperature crystalline silicon thin-film cell manufacturing?"
in: Advances in Microcrystalline and Nanocrystalline Semiconductors - 1996, ed. by R.W. Collins, P.M. Fauchet, I. Shimizu, J.-C. Vial, T. Shimada, A.P. Alivisatos (Materials Research Society Proceedings 452, Pittsburgh, PA 1996) p.865.

J. Meier, P. Torres, R. Platz, S. Dubail, U. Kroll, J.A. Anna Selvan, N. Pellaton Vaucher, C. Hof, D. Fischer, H. Keppner, A. Shah, K.-D. Ufert:
"Towards high-efficiency thin-film silicon solar cells with the 'micromorph' concept"
Solar Energy Materials and Solar Cells 49 (1997) 35.

D. Fischer, H. Keppner, U. Kroll, P. Torres, J. Meier, R. Platz, S. Dubail, J.A. Anna Selvan, N. Pellaton Vaucher, Y. Ziegler, R. Tscharner, C. Hof, N. Beck, M. Götz, P. Pernet, M. Goerlitzer, N. Wyrsch, J. Vuille, J. Cuperus, A. Shah:
"Recent progress of the 'micromorph' tandem solar cells"
Proceedings 14th European Solar Energy Conference (1997) 2347.

C. Hof, Y. Ziegler, R. Platz, N. Wyrsch, A. Shah:
"Stability of a-Si:H prepared by hot-wire and glow discharge using H2 dilution evaluated by pulsed laser degradation"
Journal of Non-Crystalline Solids 227-230 (1998) 287.

J. Meier, S. Dubail, J. Cuperus, U. Kroll, R. Platz, P. Torres, J.A. Anna Selvan, P. Pernet, N. Beck, N. Pellaton Vaucher, C. Hof, D. Fischer, H. Keppner, A. Shah:
"Recent progress in micromorph solar cells"
Journal of Non-Crystalline Solids 227-230 (1998) 1250.

H. Keppner, D. Fischer, J. Meier, U. Kroll, N. Beck, Y. Ziegler, C. Hof, R. Platz, A. Shah:
"Low bandgap amorphous silicon top cells for micromorph tandems: results from hot-wire and VHF-plasma CVD"
Technical Digest of the 11th "Sunshine" Workshop on Thin Film Solar Cells (1998) 35.

J. Merten, J.M. Asensi, C. Voz, A. Shah, R. Platz and J. Andreu:
"Improved equivalent circuit and analytical model for amorphous silicon solar cells and modules"
IEEE Transactions on Electron Devices 45 (1998) 423.

F. Wang, B.J. Hinds, D. Wolfe and G. Lucovsky, R. Platz and S. Wagner:
"A study of silicon suboxide thin films by photoluminescence"
in: Amorphous and Microcrystalline Silicon Technology - 1998, ed. by H. Branz, M. Hack, R. Schropp, I. Shimizu, S. Wagner (Materials Research Society Proceedings 507, Pittsburgh, PA 1998), in print.

N. Pellaton Vaucher, J.-L. Nagel, R. Platz, D. Fischer, A. Shah:
"Light management in tandem cells by an intermediate reflector layer"
Proc. 2nd World Conference on Photovoltaic Energy Conversion (Vienna 1998), in print.

VII. References

1 BP Statistical Review of World Energy 1997, June 1997.
2 T. Jackson, Energy Policy 20 (1992) 861.
3 A.V. Shah, R. Platz, H. Keppner, Solar Energy Materials and Solar Cells 38 (1995) 501.
4 D.E. Carlson, C.R. Wronski, Appl. Phys. Lett. 28 (1976) 671.
5 D.L. Staebler, C.R. Wronski, Appl. Phys. Lett. 31 (1977) 292.
6 D. Fischer, PhD thesis, Université de Neuchâtel 1994.
7 A. Payne, PhD thesis, Princeton University 1998.
8 Y. Hishikawa, N. Nakamura, S. Tsuda, S. Nakano, Y. Kishi, Y. Kuwano, Jpn. J. Appl. Phys. 30 (1991) 1008.
9 R. Swanepoel, J. Sci. Instr. 16 (1983) 1214.
10 J. Tauc, R. Grigorovici, A. Vancu, Physica Status Solidi 15 (1966) 627.
11 C.R. Wronski, B. Abeles, G.D. Cody, Solar Cells 2 (1980) 245.
12 M. Vanecek, J. Kocka, J. Stuchlik, A. Triska, Solid State Communications 39 (1981) 1199.
13 E. Sauvain, PhD thesis, Université de Neuchâtel 1992.
14 N. Beck, N. Wyrsch, C. Hof and A. Shah, J. Appl. Phys. 79 (1996) 9361.
15 C. Hof, N. Beck, N. Wyrsch, D. Fischer, A. Shah, Proc. 13th European PVSEC (1995) 1634.
16 C. Hof, private communication.
17 C. Hof, Y. Ziegler, R. Platz, N. Wyrsch and A. Shah, J. Non-Cryst. Solids 227-230 (1998) 287.
18 B. Rech, S. Wieder, F. Siebke, C. Beneking, H. Wagner, MRS Symp. Proc. 420 (1996) 33.
19 M.H. Brodsky, M. Cardona, J.J. Cuomo, Phys. Rev. B 16 (1977) 3556.
20 N. Maley, I. Szafranek, MRS Symp. Proc. 192 (1990) 663.
21 E. Lotter, G.H. Bauer, MRS Symp. Proc. 258 (1992) 517.
22 K. Eberhardt, E. Lotter, M. Heintze, H.-D. Mohring, G.H. Bauer, MRS Symp. Proc. 258 (1992) 673.
23 S. Guha, J. Yang, S.J. Jones, Y. Chen, D.L. Williamson, Appl. Phys. Lett. 61 (1992) 1444.
24 W.E. Spear, P.G. LeComber, Solid State Commun. 17 (1975) 1193.
25 D.A. Anderson, W.E. Spear, Phil. Mag. B 35 (1977) 1.
26 W. Paul, D.K. Paul, B. von Roedern, J. Blake, S. Oguz, Phys. Rev. Lett. 46 (1981) 1016.
27 A. Morimoto, T. Miura, M. Kumeda, T. Shimizu, Jpn. J. Appl. Phys. 20 (1981) L833.
28 A. Matsuda, T. Yamaoka, S. Wolff, M. Koyama, Y. Imanishi, H. Kataoka, H. Matsuura, K. Tanaka, J. Appl. Phys. 60 (1986) 4025.
29 S.H. Baker, W.E. Spear, R.A.G. Gibson, Phil. Mag. B 62 (1990) 213.
30 D.W. Williamson, A.H. Mahan, B.P. Nelson, R.S. Crandall, Appl. Phys. Lett. 55 (1989) 783.
31 H. Sakai, T. Yoshida, S. Fujikake, Y. Ichikawa, MRS Symp. Proc. 149 (1989) 477.
32 W.A. Nevin, H. Yamagishi, K. Asaoka, Y. Tawada, Proc. 22nd IEEE PVSC (1991) 1347.
33 H.-D. Mohring, C.-D. Abel, R. Brüggemann, G.H. Bauer, J. Non-Cryst. Solids 137&138 (1991) 847.
34 F. Alvarez, M. Sebastiani, F. Pozzili, P. Fiorini, F. Evangelisti, J. Appl. Phys. 71 (1992) 267.
35 Y.-M. Li, B.F. Fieselmann, A. Catalano, in: Amorphous and crystalline silicon carbide IV, pp.229-238, Springer Proceedings in Physics 71, ed. by C.Y. Yang, M.M. Rahmann and G.L. Harris, Springer-Verlag Berlin Heidelberg 1992.
36 F. Demichelis, G. Crovini, C.F. Pirri, E. Tresso, R. Galloni, R. Rizzoli, C. Summonte, F. Zignani, P. Rava, A. Madan, Phil Mag. B 69 (1994) 377.
37 I. Solomon, L.R. Tessler, MRS Symp. Proc. 336 (1994) 505.
38 R.O. Dusane, S.V. Rajarshi, D.J. Goyal, V.G. Bhide, T. Nagrajan, J. Appl. Phys. 76 (1994) 242.
39 V. Chu, J.P. Conde, P. Brogueira, P. Micaelo, J.P. Jarego, M.F. da Silva, J.C. Soares, MRS Symp. Proc. 377 (1995) 565.

40 J.I. Pankove, U.S. Patent No. 4,109,271 (1978).
41 Y. Tawada, M. Kondo, H. Okamoto, Y. Hamakawa, Proc. 15th IEEE PVSC (1981) 245.
42 Y. Tawada, H. Okamoto, Y. Hamakawa, Appl. Phys. Lett. 39 (1981) 237.
43 Y. Tawada, K. Tsuge, M. Kondo, H. Okamoto, Y. Hamakawa, J. Appl. Phys. 53 (1982) 5273.
44 A. Catalano, R.V. D'Aiello, J. Dresner, B. Faughnan, A. Firester, J. Kane, H. Schade, Z.E. Smith, G. Swartz, A. Triano, Proc. 16th IEEE PVSC (1982) 1421.
45 A. Catalano, U.S. Patent No. 4,782,376.
46 A. Catalano, R.R. Arya, C. Fortmann, J. Morris, J. Newton, J.G. O'Dowd, Proc. 19th IEEE PVSC (1987) 1506.
47 Y.-M. Li, MRS Symp. Proc. 297 (1993) 803.
48 C.M. Fortmann, S. Lange, M. Farley, J.G. O'Dowd, Proc. 19th IEEE PVSC (1987) 296.
49 R.E. Hollingsworth, P.K. Bhat, A. Madan, Proc. 19th IEEE PVSC (1987) 684.
50 T. Yoshida, S. Fujikake, H. Shimabukuro, Y. Ichikawa, H. Sakai, Proc. 20th IEEE PVSC (1988) 335.
51 K. Nomoto, Y. Takeda, S. Moriuchi, H. Sannomiya, T. Okuno, A. Yokota, M. Kaneiwa, M. Itoh, Y. Yamamoto, Y. Nakata, T. Inogucchi, Proc. PVSEC-4 (1989) 85.
52 S. Moriuchi, Y. Inoue, H. Sannomiya, A. Yokota, M. Itoh, Y. Nakata, H. Itoh, Proc. 21st IEEE PVSC (1990) 1449.
53 F. Demichelis, G. Crovini, C.F. Pirri, E. Tresso, G. Amato, U. Coscia, G. Ambrosone, P. Rava, Thin Solid Films 241 (1994) 274.
54 J.N. Bullock, C. Bechinger, Y. Xu, D.K. Benson, H.M. Branz, MRS Symp. Proc. 420 (1996) 183.
55 W. Gao, S.-H. Lee, Y. Xu, D.K. Benson, H.M. Branz, S. Morrison, MRS Symp. Proc. 507 (1998) 345.
56 Y. Tawada, in: Amorphous Semiconductor Technologies & Devices, Vol. 6, pp.148-160, OHMSA, Ltd. and North-Holland Publishing Co., 1983.
57 M. Ohsawa, A. Asano, T. Yoshida, T. Hama, M. Nagano, Y. Ichikawa, H. Sakai, Techn. Dig. PVSEC-5 (1990) 989.
58 W. Beyer, R. Hager, H. Schmidbauer, G. Winterling, Appl. Phys. Lett. 54 (1989) 1666.
59 H. Rübel, J. Fölsch, H. Schade, Proc. 23rd IEEE PVSC (1993) 1016.
60 E. Schaller, Université de Fribourg, private communication.
61 R. Zedlitz, E. Lotter, M. Heintze, J. Non-Cryst. Solids 164-166 (1993) 1031.
62 M.P. Schmidt, J. Bullot, M. Gauthier, P. Cordier, I. Solomon, H. Tran-Quoc, Phil. Mag. B 51 (1985) 51.
63 R. Vincenzoni, G. Masini, G. Leo, G. Guattari, F. Galluzi, MRS Symp. Proc. 297 (1993) 687.
64 J. Robertson, Phil. Mag. B 62 (1992) 615.
65 X. Xu and S. Wagner, in: Amorphous and microcrystalline semiconductor devices, vol. II, pp.89-128, ed. by J. Kanicki, Artech House, Boston, London, 1992.
66 H. Wieder, M. Cardona, C.R. Guarnieri, Phys. Stat. Sol. (B) 92 (1979) 99.
67 R.R. Koropecki, F. Alvarez, R. Arce, J. Appl. Phys. 69 (1991) 7805.
68 A.H. Mahan, R. Raboisson, D.L. Williamson, R. Tsu, Solar Cells 21 (1987) 117.
69 G. Crovini, F. Demichelis, C.F. Pirri, E. Tresso, J. Meier, S. Dubail, A. Shah, MRS Symp. Proc. 336 (1994) 481.
70 Y. Ziegler, PhD thesis, Université de Neuchâtel 1997.
71 S. Guha, K.L. Narasimhan, S.M. Pietruszko, J. Appl. Phys. 52 (1981) 859.
72 X. Xu, J. Yang, S. Guha, J. Non-Cryst. Solids 198-200 (1996) 60.
73 L. Yang, L.-F. Chen, MRS Symp. Proc. 336 (1994) 669.
74 X. Deng, K.L. Narasimhan, J. Evans, M. Izu, R.S. Ovshinsky, Proc. 1st WCPEC (1994) 678.
75 K. Tabuchi, F. Fujikake, H. Sato, S. Saito, A. Takano, T. Wada, T. Yoshida, Y. Ichikawa, H. Sakai, F. Natsume, Proc. 26th IEEE PVSC (1997) 611.
76 $\mu_0\tau_0$ measurements performed by C. Hof.
77 J. Yang, X. Xu, S. Guha, MRS Symp. Proc. 336 (1994) 687.

78 H. Curtins, N. Wyrsch, M. Favre, A.V. Shah, Plasma Chemistry and Plasma Processing 7 (1987) 267.
79 A. Howling, J.L. Dorier, C. Hollenstein, U. Kroll, F. Finger, J. Vac. Sci. Technol. A 10 (1992) 1080.
80 M. Heintze, R. Zedlitz, G.H. Bauer, J. Phys. D: Appl. Phys. 26 (1993) 1781.
81 S. Guha, Proc. 25th IEEE PVSC (1996) 1017.
82 R. Platz, D. Fischer, S. Dubail and A. Shah, Solar Energy Materials and Solar Cells 46 (1997) 157.
83 L. Yang, M. Bennett, L. Chen, K. Jansen, J. Kessler, Y. Li, J. Newtown, K. Rajan, F. Willing, R. Arya, D. Carlson, MRS Symp. Proc. 420 (1996) 839.
84 T.I. Kamins, Polycrystalline silicon for integrated circuit applications, Kluwer Academic Publishers 1988, p.68.
85 Y. Ziegler, private communication.
86 M. Bennett, K. Rajan, K. Kritikson, Proc. 23rd IEEE PVSC (1993) 845.
87 P. Lechner, H. Rübel, N. Kniffler, Proc. 10th EC-PVSEC (1991) 354.
88 H. Schade, P. Lechner, H. Rübel, Proc. 12th EC-PVSEC (1994) 89.
89 M. Nishikuni, T. Takahama, S. Okamoto, K. Ninomiya, H. Nishiwaki, S. Tsuda, A. Takeoka, M. Ohnishi, S. Nakano, Y. Kuwano, Progr. in Photovoltaics 2 (1994) 211.
90 J. Dutta, Z.Y. Wu, T. Emeraud, E. Turlot, E. Comil, J.P.M. Schmitt, A. Ricaud, Proc. 11th EC-PVSEC (1992) 545.
91 J. Bezemer, W.G.J.H.M. van Sark, M.B. von der Linden, W.F. van der Weg, P.M. Meijer, J.D.P. Passchier, W.J. Goedheer, Proc. 12th EC-PVSEC (1994) 327.
92 S. Wieder, B. Rech, C. Beneking, F. Siebke, W. Reetz, H. Wagner, Proc. 13th EC-PVSEC (1995) 234.
93 E. Maruyama, Y. Hishikawa, M. Tanaka, S. Kiyama, S. Tsuda, MRS Symp. Proc. 420 (1996) 329.
94 S. Guha, X. Xu, J. Yang, A. Banerjee, Appl. Phys. Lett. 66 (1995) 595.
95 K. Saito, M. Sano, K. Ogawa, I. Kajita, J. Non-Cryst. Solids 164-166 (1993) 689.
96 S. Sugiyama, X. Xu, J. Yang, S. Guha, MRS Symp. Proc. 420 (1996) 197.
97 S. Wieder, diploma thesis, RWTH Aachen 1996.
98 H. Matsumura, J. Appl. Phys. 65 (1989) 4396.
99 A.H. Mahan, J. Carapella, B.P. Nelson, R.S. Crandall, I. Balber, J. Appl. Phys. 69 (1991) 6728.
100 M. Vanecek, A.H. Mahan, B.P. Nelson, R.S. Crandall, Proc. 11th European PVSEC (1993) 96.
101 D. Kwon, J.D. Cohen, B.P. Nelson, E. Iwaniczko, MRS Symp. Proc. 377 (1995) 301.
102 R. Zedlitz, F. Kessler, M. Heintze, J. Non-Cryst. Solids 164-166 (1993) 83.
103 P. Papapdopulos, A. Scholz, S. Bauer, B. Schröder, H. Oechsner, J. Non-Cryst. Solids 164-166 (1993) 87.
104 M. Vanecek, A.H. Mahan, B.P. Nelson, R.S. Crandall, Proc. 12th European PVSEC (1994) 354.
105 J.T. Stephen, D. Han, A.H. Mahan, Y. Wu, MRS Symp. Proc. 420 (1996) 485.
106 Y. Ziegler, private communication.
107 B. Chapman: Glow discharge processes, sputtering and plasma etching, John Wiley & Sons Inc. 1980.
108 R. Platz, D. Fischer, S. Dubail, A. Shah, Proc. 14th EC-PVSEC (1997) 636.
109 X. Xu, J. Yang, S. Guha, MRS Symp. Proc. 297 (1993) 649.
110 R.E.I. Schropp, A. Sluiter, M.B. von der Linden, J.D. Ouwens, J. Non-Cryst. Solids 164-166 (1993) 709.
111 J. Bauer, H. Calwer, P. Marklstorfer, P. Milla, F.W. Schulze, K.-D. Ufert, J. Non-Cryst. Solids 164-166 (1993) 685.
112 R.L. Jacobson, F.R. Jeffrey, R.K. Westerberg, R.C. Williams, Proc. 19th IEEE PVSC (1987) 588.
113 J. Macneil, A.E. Delahoy, F. Kampas, E. Eser, A. Varvar and F. Ellis Jr., Proc. 21st IEEE PVSC (1990) 1501.

114 J. Xi, T. Liu, V. Iufelice, M. Nugent, K. Si, J. de Cueto, M. Ghosh, F. Kampas, Proc. 23rd IEEE PVSC (1993) 821.
115 Y.-M. Li, F. Jackson, R.R. Arya, Proc. 23rd IEEE PVSC (1993) 850.
116 J. Yang, A. Banerjee, T. Glatfelter, S. Sugiyama, S. Guha, Proc. 26th IEEE PVSC (1997) 563.
117 B. Rech, C. Beneking, U. Zastrow, H. Wagner, Proc. 12th EC PVSEC (1994) 1245.
118 K.S. Lim, M. Konagai, K. Takahashi, J. Appl. Phys. 56 (1984) 538.
119 W.Y. Kim, H. Tasaki, M. Konagai, K. Takahashi, J. Appl. Phys. 61 (1987) 3071.
120 H. Sakai, T. Yoshida, S. Fujikake, T. Hama, Y. Ichikawa, J. Appl. Phys. 67 (1990) 3494.
121 B. Rech, C. Beneking, H. Wagner, Proc. 1st WCPEC (1994) 472.
122 R. Platz, D. Fischer, A. Shah, MRS Symp. Proc. 377 (1995) 645.
123 SIMS measurements performed at the Forschungszentrum Jülich by A. Mück.
124 U. Kroll, J. Meier, H. Keppner and A. Shah, S.D. Littlewood and I.E. Kelly, P. Giannoulès, J. Vac. Sci. Technol. A 13(6) (1995) 2742.
125 M. Isomura, T. Kinoshita, Y. Hishikawa and S. Tsuda, Appl. Phys. Lett. 65 (18) (1994) 2329.
126 M. Kubon, N. Schultz, M. Kolter, C. Beneking, H. Wagner, Proc. 12th EC-PVSEC (1994) 1268.
127 J. Morris, R.R. Arya, C. Poplawski, A. Catalano, R. Podlesny, J.L. Newton, A. Wilczynski, T. Lommarson, Proc. 21st IEEE PVSC (1990) 1445.
128 K. Nomoto, H. Saitoh, A. Chida, H. Sannomiya, M. Itoh, Y. Yamamoto, Techn. Dig. PVSEC-7 (1993) 275.
129 Y. Ichikawa, S. Fujikake, T. Yoshida, T. Hama and H. Sakai, Proc. 21st IEEE PVSC (1990) 1475.
130 B. Rech, C. Beneking, S. Wieder, T. Eickhoff and H. Wagner, Proc. 13th EC-PVSEC (1995) 613.
131 Y.-M. Li, L. Yang, M.S. Bennett, L. Chen, F. Jackson, K. Rajan and R.R. Arya, MRS Symp. Proc. 336 (1994) 723.
132 Y. Hishikawa, K. Ninomiya, E. Maruyama, S. Kuroda, A. Terakawa, K. Sayama, H. Tarui, M. Sasaki, S. Tsuda and S. Nakano, Solar Energy Materials and Solar Cells 41/42 (1996) 441.
133 J. Meier, S. Dubail, J. Cuperus, U. Kroll, R. Platz, P. Torres, J.A. Anna Selvan, P. Pernet, N. Beck, N. Pellaton Vaucher, C. Hof, D. Fischer, H. Keppner and A. Shah, J. Non-Cryst. Solids 227-230 (1998) 1250.
134 J. Meier, S. Dubail, R. Platz, P. Torres, U. Kroll, J.A.A. Selvan, N. Pellaton Vaucher, C. Hof, D. Fischer, H. Keppner, R. Flückiger, A. Shah, V. Shklover, K.-D. Ufert, Solar Energy Materials and Solar Cells 49 (1997) 35.
135 M. Götz, PhD thesis, Ecole Polytechnique Fédérale de Lausanne 1997.
136 K. Saito, M. Sano, K. Matuda, T. Kondo, T. Nishimoto, K. Ogawa, I. Kajita, Proc. 2nd WCPEC (1998) 351.
137 K. Yamamoto, T. Suzuki, M. Yoshimi, A. Nakajima, Proc. 14th EC-PVSEC (1997) 1018.
138 W. Ma, T. Horiuchi, C.C. Lim, K. Goda, H. Okamoto, Y. Hamakawa, Proc. 23rd IEEE PVSC (1993) 833.
139 N. Pellaton Vaucher, PhD thesis, Université de Neuchâtel, 1998.
140 X. Xu, J.C. Yang, S. Guha, Proc. 23rd IEEE PVSC (1993) 971.
141 R.E.I. Schropp, M.B. von der Linden, J. Wallinga, D. Knoesen, J. Hyvärinen, J. Skarp, T. Suntola, J.A. Willemen, M. Zeman, J.W. Metselaar, W. Loyer, D. Guillardeau, E. Fabre, Proc. 1st WCPEC (1994) 626.
142 U. Eicker, Proc. 10th EC-PVSEC (1991) 358.
143 J. Meier, H. Keppner, S. Dubail, Y. Ziegler, L. Feitknecht, P. Torres, C. Hof, U. Kroll, D. Fischer, J. Cuperus, J.A. Anna Selvan, A. Shah, Proc. 2nd WCPEC (1998) 375.
144 E. Böhmer, F. Siebke, B. Rech, C. Beneking, H. Wagner, MRS Symp. Proc. 426 (1996) 519.
145 D. Fischer, S. Dubail, J.A. Anna Selvan, N. Pellaton Vaucher, R. Platz, C. Hof, U. Kroll, J. Meier, P. Torres, H. Keppner, N. Wyrsch, M. Götz, A. Shah, K.-D. Ufert, Proc. 25th IEEE PVSC (1996) 1053.

146 K. Yamamoto, T. Suzuki, M. Yoshimi, A. Nakajima, Proc. 25th IEEE PVSC (1996) 661.
147 N. Pellaton Vaucher, J.-L. Nagel, R. Platz, D. Fischer, A. Shah, Proc. 2nd WCPEC (1998) 728.
148 R. Platz, N. Pellaton Vaucher, D. Fischer, J. Meier, A. Shah, Proc. 26th IEEE PVSC (1997) 691.
149 T. Takahama, S. Okamoto, K. Ninomiya, M. Nishikuni, N. Nakamura, S. Tsuda, M. Ohnishi, S. Nakano, Y. Kishi, Y. Kuwano, Techn. Dig. PVSEC-5 (1990) 375.
150 J. Yang, S. Sugiyama, S. Guha, MRS Symp. Proc. 507 (1998) 157.
151 X. Deng, S.J. Jones, T. Liu, M. Izu, S.R. Ovshinsky, Proc. 26th IEEE PVSC (1997) 591.
152 S.J. Jones, X. Deng, T. Liu, M. Izu, MRS Symp. Proc. 507 (1998) 113.
153 W.G.J.H.M. van Sark, J. Bezemer, E.M.B. Heller, M. Kars and W.F. van der Weg, MRS Symp. Proc. 377 (1995) 3.
154 W.G.J.H.M. van Sark, J. Bezemer, R. van der Heiden, W.F. van der Weg, MRS Symp. Proc. 420 (1996) 21.
155 H. Meiling, J. Bezemer, R.E.I. Schropp, W.F. van der Weg, MRS Symp. Proc. 467 (1997) 459.
156 M. Heintze, MRS Symp. Proc. 467 (1997) 471.
157 T. Takagi, Y. Nakagawa, Y. Watabe, K. Takechi, S. Nishida, MRS Symp. Proc. 467 (1997) 483.
158 J. Hautala, Z. Saleh, J.F.M. Westendorp, H. Meiling, S. Sherman, S. Wagner, MRS Symp. Proc. 420 (1996) 83.

Acknowledgements

I thank Prof. A. Shah for the possibility to work in his group and for his never-ending effort to maintain the excellent working conditions at IMT. My colleagues from IMT helped with advice, croissants and a nice atmosphere in the laboratory. Special thanks to Sébastien Dubail for a most efficient and enjoyable collaboration using the same deposition system, as well as to Dr. Diego Fischer for his estimated advice and time. The chapter on a-Si:H material would have been incomplete without the precious help of Christian Hof who performed the degradation experiments and transport measurements.

I thank Prof. J. Faist, Dr. H. Schade and Prof. S. Wagner for kindly taking over the reading of the thesis and many useful comments.

I am very much obliged to Prof. S. Wagner for accepting me in his group at Princeton University where I spent a most exciting and enriching year.

Dr. Bernd Rech, Stephan Wieder and many others from the Forschungszentrum Jülich have always been open for discussions and exchange across European borders.

Without the financial support of the "Arthur und Aenne Feindt Stiftung" as well as the "Fondation Charles-Edouard Guillaume" my stay at Princeton University would not have been possible.